“The Northern Chile forearc constrained by 15 years of permanent seismic monitoring”

Christian Sippl (sippl@ig.cas.cz)
Bernd Schurr (schurr@gfz-potsdam.de)
Jannes Münchmeyer (munchmej@univ-grenoble-alpes.fr)
Sergio Barrientos (sbarrien@dgf.uchile.cl)
Onno Oncken (oncken@gfz-potsdam.de)

This manuscript is a postprint, the original publication is in the *Journal of South American Earth Sciences*, and is available under the following DOI: https://doi.org/10.1016/j.jsames.2023.104326.

The Northern Chile forearc constrained by 15 years of permanent seismic monitoring

Christian Sippl[1,*], Bernd Schurr[2], Jannes Münchmeyer[2,4], Sergio Barrientos[3], Onno Oncken[2]

Abstract

In this review article, we compile seismological observations from the different constituent parts of the Northern Chile forearc: the downgoing Nazca Plate, the plate interface, the upper South American Plate as well as the mantle wedge beneath it. As Northern Chile has been monitored by a network of permanent seismic stations since late 2006, there is a wealth of observations that enables us to characterize the structure as well as ongoing processes in the forearc throughout the last 15 years. We put an emphasis on the analysis of seismicity, for which we have extended a massive earthquake catalog that now contains >180,000 events for the years 2007-2021. Moreover, we draw on published results for earthquake mechanisms, source properties, seismic velocity structure, statistical seismology and others, and discuss them in context of results from neighboring disciplines. We thus attempt to provide a comprehensive overview on the seismological knowledge about the structure and ongoing processes in the Northern Chile forearc, a breviary of which is found in the following:

The Northern Chile megathrust hosted two major earthquake sequences during the analyzed time period. The 2007 M_w 7.8 Tocopilla earthquake broke the deep part of the megathrust just north of Mejillones Peninsula, whereas the 2014 M_w 8.1 Iquique earthquake ruptured the central segment in the north of the study region. The latter event has a highly interesting preparatory phase, including a significant foreshock sequence as well as aseismic slip transients. Besides these large events, background seismicity elsewhere on the megathrust may be helpful for characterizing the earthquake potential and locking state in the remaining seismic gap.

The downgoing Nazca Plate in Northern Chile exhibits very high seismicity rates, with the vast majority of earthquakes occurring at depths of ∼80-140 km with downdip extensive mechanisms. While seismic tomography shows no sudden changes in slab geometry along strike, seismicity describes peculiar offsets that may be linked to subducted features on the oceanic plate. Upper plate seismicity likewise shows strong variations along strike, with the north and south of the study area showing only weak activity, whereas the central segment shows pervasive microseismicity throughout the upper plate, all the way to the plate interface. These earthquakes have thrust and strike-slip mechanisms with P-axes striking roughly N-S, indicating margin-parallel compression that may be connected to the concavity of the margin.

Keywords: Northern Chile, Subduction zone, Seismicity, Forearc, Fluid processes

1. Introduction

The subduction plate margin in Northern Chile is one of the most seismically active regions on this planet. The activity encompasses all its structural parts: within the last 20 years, the Northern Chile megathrust ruptured with an M8.1 and two M>7.5 events, the subducted Nazca Plate hosted one M>7.5 and about 20 M>6 earthquakes and the upper South American Plate still featured two events of M>6. Due to its status as a prominent seismic gap that had not ruptured since 1877 (see Figure 1), the region has been permanently monitored with seismic stations since late 2006. With 15 years of uninterrupted station coverage, Northern Chile is one of the better-monitored subduction zone segments globally. The M8.1 Iquique earthquake in 2014 (Schurr et al., 2014; Ruiz et al., 2014; Hayes et al., 2014) partially closed the seismic gap, but great earthquakes are still expected to the south and north of it (Lay and Nishenko, 2022), so that ongoing observation of the region is essential. The present article is an attempt to summarize the seismological state-of-knowledge on the Northern Chile forearc between Arica at the Peruvian border (∼18.3°S) and the Mejillones Peninsula in the south (∼23.5°S; see Figure 1). We will present an overview of observations that was gained from past and ongoing seismological experiments, while also introducing and analyzing an extended and comprehensive microseismicity catalog that covers the years 2007 to 2021 (>180,000 events), and thus allows us to investigate long-term trends. After introducing the regional tectonic setting (Section 2) and describing the seismicity catalog (Section 3), we compile observations and conceptual models for the different constituent parts of the Northern Chile forearc: the plate interface (Section 4), the downgoing plate (Section 5), the mantle wedge (Section 6) and the upper plate (Section 7). In each of these sections, we will draw on seismological evidence for the observation summary and include results from neighboring disciplines such as geodesy or geology for the discussion of ongoing processes. Lastly, we will provide an outlook onto potential interactions between the different parts of the forearc (Section 8).

2. Tectonic Setting

Regional plate kinematics in Northern Chile are prescribed by the slightly oblique ENE-directed convergence between the downgoing oceanic Nazca Plate and the South American Plate with a relative velocity of about 6.7 cm/yr (Angermann et al., 1999; Norabuena et al., 1998; Jarrin et al., 2022). The Nazca Plate

*corresponding author: sippl@ig.cas.cz
[1]Institute of Geophysics, Czech Academy of Sciences, Prague, Czech Republic
[2]Helmholtz Centre Potsdam - German Research Centre for Geosciences (GFZ), Potsdam, Germany
[3]National Seismological Center, Faculty of Physical and Mathematical Sciences, University of Chile, Santiago, Chile
[4]now at: Centre National de la Recherche Scientifique, ISTerre, Université Grenoble Alpes, Grenoble, France

is 46-52 Ma old where it impinges on the trench (Figure 1; e.g. Müller et al., 2008). Beyond the trench, it acquires a slab dip of 20-25°, which makes it a region of conventional subduction in-between two flat slab sections in Southern Peru (e.g. Bishop et al., 2017) and Central Chile (Ramos and Folguera, 2009). With a thermal parameter of 1500-1750 (e.g. Syracuse et al., 2010), the Northern Chile subduction zone can be classified as intermediate between young and warm subduction zones like Cascadia and old and cold ones like Tonga or NE Japan. The Northern Chile forearc is situated at the latitude where the Andean orogen reaches its largest width and exhibits two major ∼4 km high plateaux (Altiplano and Puna) in the backarc (e.g. Oncken et al., 2006; Beck et al., 2015). The Nazca Plate offshore Northern Chile features crustal thicknesses between 6 to 8 km in most places (e.g. Tassara et al., 2006; Patzwahl et al., 1999; Ranero and Sallarès, 2004), which conforms to the global average (Grevemeyer et al., 2018). Along the NE-to-NNE-striking Iquique Ridge (Figure 1), a hotspot track that formed 45-50 Ma ago and started colliding with South America 40 Ma ago (Bello-González et al., 2018; Contreras-Reyes et al., 2021b), crustal thickness values of up to 13 km have been detected (Myers et al., 2022). The margin is sediment-starved due to a lack of sediment delivery, a result of the extreme aridity in the forearc (e.g. von Huene and Scholl, 1991), readily exposing normal-faulting scarps in the Outer Rise region (e.g. Geersen et al., 2018) as well as the deep trench (>8000 m).

To the north of the study region, the entire margin describes a westward concave arc, the "Arica Bend". Onshore, the Northern Chile forearc is made up of a series of four older magmatic arcs which date back until the Jurassic, a setup that was formed due to long-term subduction erosion of the upper plate and stepwise arc retreat since that time (e.g. Rutland, 1971; von Huene and Scholl, 1991; Haschke et al., 2006). The present morphology of the forearc is characterized by the presence of the Coastal Cordillera - exposing the Jurassic magmatic arc (Figure 2) - which gives rise to significant topography close to the coastline (see inset in Figure 1). The Longitudinal Valley - overlying the Cretaceous arc - separates the Coastal Cordillera from the Precordillera (the Paleogene arc) and Western Cordillera, which sits on the western shoulder of the plateau and constitutes the current active magmatic arc. In the northern part of the Western Cordillera, recent volcanism is notably absent from a region between about 19.5 and 20.5°S, which is referred to as the Pica Volcanic Gap (Wörner et al., 1992, Figures 1 and 2). In the southeast of the study area, the Salar de Atacama is an anomalous crustal block (e.g. Reutter et al., 2006; Schurr and Rietbrock, 2004) with low topography, which prescribes a prominent eastward deflection of the magmatic arc (Figure 1). Neogene kinematics of the forearc is controlled by extensional structures in the upper crust of the outer forearc and the Coastal Cordillera (e.g. von Huene and Ranero, 2003) and by contractional to strike-slip tectonics in the Andes western flank monocline and Precordillera (Victor et al., 2004). Reflection seismic studies (Sick et al., 2006) and analysis of focal mechanisms of megathrust earthquake aftershocks (Schurr et al., 2012) provide evidence that kinematics at depth may be contraction-dominated throughout the forearc. As evidenced from the analysis of InSAR data (Shirzaei et al., 2012), this contraction regime may involve the upper forearc crust as well in certain stages of the megathrust seismic cycle. Finally, the central part of the study area near the symmetry axis of the Andes orocline at ∼20-21.5°S (Gephart, 1994) is closely linked to a zone of trench-parallel contraction of the entire forearc crust (Allmendinger and González, 2010).

3. Data

3.1. Seismic station deployment history

While Northern Chile was the focus of several short-term temporary deployments of seismic stations and regional triggered and telemetered short-period networks in the 1990s and early 2000s (e.g. Comte et al., 1999; Asch et al., 2006), modern permanent continuous broadband monitoring began with the installation of the first stations of the IPOC initiative in late 2006 (network CX; see GFZ and CNRS-INSU, 2006). Since then, the number of permanent stations of the backbone network has steadily increased (see http://ipoc-network.org), so that there is a total of 28 broadband stations in the region today, some of them part of the networks of the CSN (Centro Sismológico Nacional; Barrientos, 2018) and GEOFON. In addition to these permanent stations, several temporary deployments were conducted in the past 15 years, many of them in the wake of the two large megathrust earthquakes (the M_w 7.8 Tocopilla earthquake in November 2007 and the M_w 8.1 Iquique earthquake in April 2014). The configuration of the seismic networks, which formed and form the base for all the research that will be summarized in this article, is shown in Figure 3. All of these data are archived and freely available from GEOFON (https://geofon.gfz-potsdam.de/waveform/archive/) or IRIS (https://www.iris.edu/hq/).

3.2. IPOC seismicity catalog

This article makes use of the IPOC seismicity catalog, an extension of the previously published and analyzed catalog of Sippl et al. (2018). While the previous version of the catalog covers the years 2007-2014, the new IPOC catalog (freely available for download: see Acknowledgments) contains 7 more years of data (2007-2021). It is compiled in a semi-automated fashion, using a simple STA/LTA trigger (e.g. Withers et al., 1998) for initial pick generation, more sophisticated pickers (*MPX* and *spicker*; Di Stefano et al., 2006; Diehl et al., 2009) for the determination of P- and S-arrivals, and eventually yields a double-difference (Waldhauser and Ellsworth, 2000) relocated catalog with location uncertainties <5 km inside the utilized network geometry. Events with epicenters clearly outside the footprint of the station network (Figure 3) can have substantially larger location uncertainties. The procedure of automated event detection, waveform picking and hypocenter (re)location is described in detail in Sippl et al. (2018). Although the here presented IPOC catalog is an extension of the Sippl et al. (2018) catalog, there will be subtle location differences for most events between the two catalogs. This is a consequence of the use of relative relocation for all events, so that the addition of new events also modifies the locations of previously existing ones.

Sippl et al. (2018) categorized events based on their hypocentral depths and their location relative to the surface of the downgoing Nazca Slab (Figure 4). In the updip part of the slab, events in the upper plate (UP), on the plate interface (P1) as well as the upper (P2) and lower (P3) plane of intraslab earthquakes are distinguished based on their distance from the slab surface model of Sippl et al. (2018), as shown in Figure 4a. Intraslab events further east and at deeper depths are referred to as intermediate-depth seismicity (ID), whereas events outside the other class definitions as well as far outside the seismic network are given the class identifier NN (see Figure 4b). In the present article, we use the same classification scheme (details outlined in Table 1 of Sippl et al., 2018) and colors, but modified it in two ways. Firstly, we now require events that get classified as occurring within the upper plate (class UP) to have hypocentral depths shallower than 60 km. This was introduced to avoid mislabelling of some outlier intraslab events that end up located too shallowly, significantly above the slab surface, in the eastern part of the study area. Secondly, we defined an additional class MI that contains mining-related seismicity. We mapped visible mining locations in GoogleEarth (mining in Northern Chile occurs predominantly with open pits, so locations are clearly visible in satellite imagery), and defined all events that occur with less than 15 km epicentral distance from a mapped mining location and a hypocentral depth of less than 15 km as belonging to class MI. Figure 5 shows location plots of events from classes MI and UP, as well as histograms of event origin times, which show that nearly all events thus defined to belong to class MI occur during local daytime, most prominently between 10 am and 8 pm, which is a clear hint that they are related to human activity. The much more even distribution of origin times of class UP events throughout all 24 hours of the day lends confidence that the vast majority of these events has a tectonic origin.

The IPOC catalog 2007-2021 contains a total of 182,847 events, the vast majority of which (129,312) occurred inside the downgoing Nazca Plate (classes ID: 116,027; P2: 8,103; P3: 5,182). 15,162 events were classified as having occurred on the plate interface, 30,371 events in the upper plate (16,927 of which were classified as mining-related). Magnitudes for the IPOC catalog were determined using the calibrated approach of Münchmeyer et al. (2020). A summary of the spatial and temporal distribution of seismicity contained in the IPOC catalog is given in Figure 6, and a series of W-E cross sections is shown in Figure 7. We will analyze different parts and event classes of the IPOC catalog in greater detail in the following Sections.

4. The subduction megathrust

Megathrusts are the frictional contact between the two converging plates in subduction zones. As the prefix implies, their dimensions are huge, as they often measure thousands of kilometers in strike direction and hundreds of kilometers in width. They produce the largest known earthquakes. In Northern Chile, the megathrust measures ∼500 km along-strike, first striking north and then curving westward, and ∼150 km in downdip direction, reaching depths of 60 km beneath the coastal region. It has produced M>8 earthquakes in the past as well as within our observation period and constitutes the largest seismic hazard to the region. In the following, we collect current knowledge about its structure, properties, segmentation and recent significant earthquakes.

4.1. Historical megathrust earthquakes

Written historical records about past earthquakes in Northern Chile unfortunately do not extend far into the past. Due to the extremely arid and hostile environment, the region was very sparsely populated, particularly in the coastal region, providing few historical sources before the mid-19th century, when saltpeter mining caused a first boom of settlement and activity. Before the 19th century, the Peruvian coast to the north has longer and more complete historical records than Northern Chile. In Figure 1, we provide a summary of large earthquakes on the Northern Chile megathrust from the two large earthquakes of 1868 and 1877 onwards, while we discuss less well-constrained but significant earlier events in the following. The earliest giant megathrust earthquake (M_w ∼9.5) that has left traces along the Northern Chile margin was inferred to have occurred ∼3800 years ago based on archeological evidence and tsunami deposits (Salazar et al., 2022). This event may have caused an exceptional social disruption of prehistoric hunter gatherer communities reflected in archeological sites along the Chilean coast between 28°S and 20°S, corroborated by littoral deposits. If its inferred extent is correct, this rupture would have propagated across the Mejillones Peninsula, which acted as barrier for more recent earthquakes (1877, 1995, 2007; see below and Section 4.4.1) and is considered a possibly persistent rupture barrier based on long-term uplift patterns (Victor et al., 2011). Except for this one very early event, all evidence for historical earthquakes postdates the arrival of the Spanish in the region. An earthquake that was felt throughout the Tarapacá province and as far as southern Peru in 1543 was estimated to have occurred between 19°S and 20°S (Greve, 1964; Comte and Pardo, 1991). Since no reports of a tsunami exist, it may also have been a deeper intraplate event (Ruiz and Madariaga, 2018). Comte and Pardo (1991) assigned it a magnitude of 7.7 based on macroseismic observations. In 1615, a strong earthquake affected the city of Arica, now in northernmost Chile, and Tacna in southern Peru. Its epicenter was estimated at 19.5°S, 70.5°W (Figure 9) with a magnitude of 7.9 based on intensity estimates (Comte and Pardo, 1991). Reports of a tsunami likely make it an interplate event. Another event before 1768, estimated at a magnitude of 7.7 (Comte and Pardo, 1991), destroyed churches in the towns of Pica and Matilla (similar to, e.g., the 2005 M_w 7.8 intermediate depth Tarapacá event; see Section 5). Like the 1543 earthquake, this event may also have been an intraplate event (Ruiz and Madariaga, 2018). In the year 1871, an earthquake caused damage in the city of Iquique, was felt from Copiapó to Lima, and apparently caused a tsunami. An epicenter at 20.1°S, 71.3°W (Figure 9) and a magnitude between 7 and 7.5 were estimated (Comte and Pardo, 1991).

The earthquake of May 10th, 1877, was the first great earthquake that was well documented to affect northern Chile, and the last event to have ruptured the Northern Chile seismic gap. It occurred nine years after the 1868 Arequipa earthquake (M_w 8.5-8.8) that strongly affected the Peruvian coast to the north (e.g. Lomnitz, 2004). A strong tsunami was documented along the Chilean coast and across the Pacific. Comte and Pardo (1991), based on isoseismal intensity estimates, suggest an epicenter at 21°S, 70.25°W (Figure 9), and a rupture length of 420 km corresponding to a magnitude of 8.8. Vigny and Klein (2022), in this issue, make a careful reappraisal of the historical sources used by Comte and Pardo (1991) and Kausel (1986) and find that this suggested rupture length was likely overestimated. They critically evaluated original reports and tsunami run-ups, and conclude that the earthquake likely only had an extent of 200-250 km based on the intensity-VIII macroseismic proxy and the impact of the tsunami. This downsized rupture area (see Figures 1 and 9) would lead to a magnitude of only 8.5 for the slip deficit accumulated for a ∼150-year period, i.e. the proposed recurrence interval of Northern Chile (Comte and Pardo, 1991). Its magnitude may have been larger in case the actual recurrence interval is longer, as could be supposed from the historical record outlined above. If the conclusions of Vigny and Klein (2022) hold true, the 1877 event would have only ruptured the "Loa" segment of the Northern Chile margin, which was defined using interplate locking models (see Section 4.2). This would then probably also restrict the dimension of the current seismic gap to this segment alone, which limits the expected magnitude of the next megathrust earthquake (see Section 4.4.3).

4.2. Interplate locking models

Coupling or locking between the upper and lower plate during convergence elastically squeezes and buckles the upper plate; the resulting deformation can be measured with space geodetic methods like GNSS or InSAR. GNSS campaigns in Northern Chile started in the 1990s (Klotz et al., 1999, 2001; Ruegg et al., 1996), and sites were regularly re-measured and densified over time, and later supplemented by continuous GNSS instrumentation (Báez et al., 2018). Spatial variations of measured onshore deformation can be inverted for variations in interplate locking, making assumptions on plate interface rheology and geometry. In Chile, the deepest part of the seismogenic zone on the plate interface is below land, and the trench-coast distance is comparatively small, i.e., only ∼100 km compared to e.g., ∼200 km in Japan or Sumatra (Williamson and Newman, 2018). This allows inversions of land-based GNSS data to reasonably well constrain the locking state of at least the lower part of the megathrust. Interplate locking is quantified as the ratio between the modeled backslip (Savage, 1983) on the megathrust and the secular convergence velocity, so that a value of 1 implies complete locking, whereas a value of 0 stands for a completely unlocked (i.e. freely slipping) megathrust. For Northern Chile, numerous locking models have been created over the years (see compilation in Figure 8), mainly relying on similar multi-year GNSS observations and some also adding InSAR line-of-sight interseismic deformation maps.

The first simple model of interseismic locking in Northern and Central Chile was obtained by Khazaradze and Klotz (2003) based on GNSS campaign data from the 1990s. Their elastic dislocation models required nearly full locking of the offshore megathrust. Shortly after, a similar result was obtained in a study that employed additional interseismic InSAR data from a single multi-year interferogram (Chlieh et al., 2004), with which a tapering of locking in the deepest part of the megathrust was constrained. This model was later updated, allowing for along-strike and along-dip variations, and extended into Peru to cover the entire Arica Bend (Chlieh et al., 2011). For Northern Chile, the model inferred almost uniformly high locking ($\sim$0.8) with a small low-locking zone (LLZ) at the latitude of the city of Iquique (Figure 8). Lower locking values were retrieved north of 19°S and around the Arica Bend, constrained by GNSS data from Peru.

A whole line of locking models was created with the much denser datasets of Métois et al. (2013) and Métois et al. (2016), who used a total of 66 benchmark measurements acquired by various groups during different multi-year GNSS campaigns from the 1990s to 2012, as well as an additional 28 continuous sites. Métois et al. (2013) assumed a plane megathrust dipping at 20° and an elastic half space for inversion and tested a 2-plate and a 3-plate model; the latter includes an Andean sliver, which may move and deform independently. The 3-plate model reduces the average coupling of the megathrust by 30% ($\sim$0.5 average coupling degree), which shows that estimates of seismic potential are strongly dependent on such modeling assumptions. Both the raw GNSS data and the resulting locking models show clear along-strike variation, resulting in three strongly coupled segments (named Camarones, Loa, and Paranal from north to south; Figure 8) separated by narrow low-locking barriers at Mejillones Peninsula and around 20.2°S near Iquique (Figure 8). Schurr et al. (2014) adopted the data set of Métois et al. (2013) but inverted with a more realistic slab model (Hayes et al., 2012) and for a layered upper plate, applying a correction for Andean sliver movement and shortening. Similar to Métois et al. (2013), three distinct high coupling regions are resolved north and south of Mejillones Peninsula and north of Iquique. These are restricted by the coastline, with tapering of the locking degree further inland. Li et al. (2015) took GNSS data from Métois et al. (2013) and Kendrick et al. (2003) and used viscoelastic Green's functions calculated from a detailed 3D finite-element model of the upper and lower plate. Schurr et al. (2020) used the same modeling strategy and parameterization with an extended data set (40 continuously recording sites, 71 survey-type sites). Both resulting models show a similar segmentation as previous ones (Métois et al., 2013, 2016), with a LLZ north of Mejillones and south of Iquique. The model of Hoffmann et al. (2018) is purely elastic and was implemented with a detailed 3D plate geometry and Andean sliver motion. They inverted both campaign (51 sites) and continuous (50 sites) horizontal and vertical-component GNSS data. Their model shows several highs and lows, as well as low coupling near the trench and below the coast. The high-locking zone between Mejillones and 21°S present in all other models is here interrupted by a locking low near Tocopilla.

A second group of locking models was obtained from inverting InSAR data together with GNSS observations. Béjar-Pizarro et al. (2013) stacked 18 Envisat interseismic interferograms covering the coastal area north and south of the Mejillones Peninsula and used the vertical signal from sparse continuous GNSS stations. InSAR line-of-sight (LOS) displacement, which is subvertical, has a peak on land and paralleling the coastline, thereby constraining the down-dip limit of strong locking that is supposedly located there (Malatesta et al., 2021). The obtained downdip boundary of locking was found to skirt around Mejillones Peninsula, implying that frictional behavior on the megathrust influences coastal morphology. Jolivet et al. (2020) used seven years of Envisat data to derive interseismic LOS velocity maps and, combined with the GNSS data set of horizontal velocities of Métois et al. (2016), inverted for locking with a Bayesian formalism. They obtained an almost continuous, elongated, strongly locked region across Mejillones Peninsula that terminates at ~20.5°S, keeping the region to the north mostly unlocked except for an offshore patch near the Iquique earthquake rupture area. In this model, locking terminates sharply close to the coastline, leaving the megathrust beneath the onshore region largely unlocked. This feature is more or less common to all models using InSAR data (Chlieh et al., 2011; Béjar-Pizarro et al., 2013; Jolivet et al., 2020, Figure 8) and stems from the observation of uplift along the coast, which requires strong locking to terminate towards the shoreline in elastic models. Horizontal shortening observations from GNSS are less sensitive to this boundary.

Figure 8 shows all discussed locking models plotted within the same map and using the same color scale. They show significant differences, showcasing that differences in data coverage, modeling strategy, parameterization, and regularization strongly impact the resulting locking distributions. We calculated an average of those seven models that we could easily project onto a common grid (Métois et al., 2016; Chlieh et al., 2011; Jolivet et al., 2020; Hoffmann et al., 2018; Schurr et al., 2014, 2020; Li et al., 2015, Figure 8). At first glance, most models show a pattern of three locking highs, separated by lowly locked barriers at Mejillones Peninsula and south of Iquique. This segmentation is also retained by the average model, suggesting it to be a robust feature. In addition, a subdued LLZ offshore Tocopilla appears to be traceable in the average model. The tapering of locking towards the trench in the average model is probably caused by increasing disparity between individual models towards the trench due to increasing lack of resolution, and hence should not be trusted. The barrier at Mejillones Pensinsula may be long-lived, consistent with historical earthquakes (Figure 1, Section 4.1) and regional morphology (Victor et al., 2011). The LLZ south of Iquique may have acted as a barrier of the 1877 event (Vigny and Klein, 2022) and also limited the 2014 Iquique earthquake to the south. Interestingly, this LLZ seems to have been occupied by the M_w 7.6 Iquique aftershock (see Section 4.4.2), which may, however, have actually ruptured in two clearly separated asperities up- and downdip (e.g. Jara et al., 2018), too small to be resolved interseismically. As mentioned above, locking models derived using InSAR data show an eastward termination of locking around the coastline. An essentially uncoupled megathrust below the coastal region (slab depth 40-55 km) is, however, incompatible with the occurrence of large earthquakes at these depths (e.g. the M_w 7.8 2007 Tocopilla event, see Section 4.4.1), as well as the observation of microseismicity (Figure 9) and lower plate compressional earthquakes (Bloch et al., 2018a; Sippl et al., 2019, Figure 15) there. We also plot the residual gravity field (Figure 8, upper left panel) from satellite altimetry (Bassett and Watts, 2015) for the offshore region. The high locking zone of the Loa segment apparent in most models as well as in the average is co-located with a gravity high, and this correlation is particularly clear for the locking high in the model of Jolivet et al. (2020). This stands in contrast to global observations that asperities on megathrusts tend to be associated with gravity lows (Wells et al., 2003; Song and Simons, 2003), which was interpreted as indicating basal erosion of the upper plate in response to locally high friction on these patches of the megathrust (Wells et al., 2003). Maksymowicz et al. (2018) interpret the gravity high in the Loa segment as due to high density rocks in the upper plate, possibly related to a fossil volcanic arc (Bassett and Watts, 2015). These structures may cause high normal stress on the megathrust, which may cause locally higher friction. The asperity that ruptured in the 2014 Iquique earthquake (see Section 4.4.2) shows up as a locking high in all models, and this locking high is co-located with a gravity low (Meng et al., 2015; Schurr et al., 2020; Storch et al., 2023; González et al., 2023), the so-called Iquique Basin (Figure 8), thus conforming to the previously mentioned global trend. In conclusion, there is widespread incongruence between published locking models advising us to be careful when interpreting details in individual locking maps. The observed variability may well be a consequence of the non-uniqueness of data and inversion. However, the described major segmentation appears to be robust.

4.3. Plate Interface Seismicity

Interplate seismicity, categorized as class P1 in our catalog, comprises thrust earthquakes that presumably occur on the megathrust separating the oceanic Nazca Plate and the overlying continental South American Plate. This seismicity population is clearly visible in cross sections as a sharply defined, thin, eastward dipping (∼20°) layer present throughout the coastal area and reaching depths >60 km east of the coastline (Figures 4 and 7). Westward, these events shallow in hypocentral depth as well as dip angle (Figure 7). Offshore, it becomes increasingly hard to separate interplate events, upper plate events, and the upper plane of the double seismic zone (DSZ) inside the Nazca Plate (Sippl et al., 2018), which is due to decreasing location accuracy away from the land-based seismic stations. Where catalog resolution is good, event populations P1 and P2 (i.e. interplate and DSZ upper plane) are quite clearly separated (Figures 4 and 7), whereas it is hard to distinguish the deepest interplate events from upper plate events in the region between 20.5°S and 21.5°S, where a cluster of deep upper plate events is observed (see Section 7). There, categorization may not always be unique.

Interplate events are strongly clustered both in space and in time (Figure 9). A significant part of them are aftershocks of the two major megathrust ruptures in 2007 (M7.8 Tocopilla earthquake; Section 4.4.1) and 2014 (M8.1 Iquique earthquake; Section 4.4.2). Interplate earthquakes map out the seismogenic part of the plate interface, and provide important information for understanding the state and behavior of the megathrust. The complete absence of seismicity in parts of the megathrust is also meaningful, as it may signify either the predominance of aseismic deformation (creeping sections) or complete interseismic locking. We observe that background interplate seismicity mainly occurs in a swath along the coastline north of Mejillones Peninsula, at depths corresponding to the deeper half of the plate interface. In the region where the 2014 Iquique earthquake occurred, seismicity reaches further offshore, which coincides with where the trench starts to curve westward and the trench-coastline distance increases.

When analyzing the distribution of magnitudes in a seismicity population, the most commonly used parameter is the b-value, which is the slope of the magnitude-frequency distribution. High b-values (b>$\sim$1) indicate that low-magnitude events are more frequent and high-magnitude events less frequent than usual, low b-values the opposite. Interplate seismicity in Northern Chile features rather low b-values clearly below 1 ($\sim$0.6-0.8; Legrand et al., 2012; Sippl et al., 2019; Poulos et al., 2019), which is in line with global findings along megathrusts (Bilek and Lay, 2018). In the region of the Iquique earthquake, temporal variations of the b-value were detected prior to the main shock (Schurr et al., 2014, Section 4.4.2). Moreover, interplate earthquakes in the Iquique region feature relatively low stress drop values (median of 4.4 MPa; Folesky et al., 2021) as well as rupture directivities that are predominantly oriented eastwards, i.e. in downdip direction (Folesky et al., 2018a,b).

Along-strike, background seismicity shows two lulls at 23°S (Mejillones Peninsula) and 21°S (Figure 10), with the strongest maximum in-between those two. This region of high background activity was partly broken by the 2007 Tocopilla earthquake (Section 4.4.1). The lull at 21°S corresponds to a region of high oceanic plate lower plane seismicity (P3; Figure 25). There is a conspicuous complete lack of interplate seismicity offshore and updip of the coastal seismicity swath between latitudes $\sim$21°S and Mejillones Peninsula. This region has not broken since 1877 and forms a significant seismic gap capable of producing a great earthquake (e.g. Métois et al., 2013; Schurr et al., 2014; Hayes et al., 2014; Vigny and Klein, 2022). Interplate seismicity is also largely absent directly north of the Iquique earthquake's rupture area (Figure 6), where even the aftershocks of the Iquique earthquake terminate abruptly (Soto et al., 2019) despite the presence of significant afterslip in this region (Hoffmann et al., 2018; Shrivastava et al., 2019).

Figure 10 shows swath profiles through the locking models from Figure 8 parallel to the coast for the deeper part of the megathrust, where their resolution should be best and where most microseismicity is observed. In this representation, the correlation between the different locking model profiles is rather poor, confirming our conclusions from the previous Section. We compare the different along-strike variations of interplate locking with background seismicity, separated from aftershocks by a declustering algorithm

(Hainzl et al., 2019), as well as residual gravity. Background seismicity is highest along the Loa segment, just north of Mejillones Peninsula, where most models show strong locking. This is the region updip of the 2007 Tocopilla rupture, which still constitutes a significant seismic gap that has accumulated strain since 1877. Increased background seismicity at the downdip side of asperities has been observed in other places along the Chilean margin (Schurr et al., 2020; Sippl et al., 2021) and may be an indicator for stress buildup along the downdip termination of a mature asperity.

4.4. Significant instrumental megathrust earthquakes

The ISC-GEM catalog (Storchak et al., 2013) lists seven M7+ earthquakes between 1928 and 2006 (Figure 1) in our study area. They cluster in the Iquique and Mejillones regions and, as the entire background seismicity within the following years, skirt the seismic gap of the Loa segment. The largest of these events, with a moment magnitude of 7.4 (Malgrange and Madariaga, 1983) occurred in December 1967 north of Tocopilla (Figure 1). It had a shallow thrust mechanism and a depth >40 km constrained well by waveform modeling (Malgrange and Madariaga, 1983). It hence presumably occurred on the deepest part of the megathrust, similar to the 2007 Tocopilla earthquake slightly to the south (next Section).

4.4.1. The 2007 M_w 7.8 Tocopilla earthquake

The 2007 Tocopilla earthquake was the largest earthquake in the northern Chile gap since more than a century and very well recorded by the then newly installed IPOC network. It occurred mostly below land on the deepest part of the seismogenic megathrust, and its surface deformation pattern was clearly recorded by radar satellite data. Together, seismic and geodetic data led to well-constrained source models. The rupture was confined to an approximately 130×75 km swath covering a depth range between 30 and 55 km that roughly parallels the coastline (Figure 11; Delouis et al., 2009; Béjar-Pizarro et al., 2010; Motagh et al., 2010; Peyrat et al., 2010; Loveless et al., 2010; Schurr et al., 2012). The slip distribution shows two patches, with one near the hypocenter and one further south (Figure 11). Maximum slip was about 2-3 m on the southern patch. The two patches ruptured consecutively, separated by ∼20 s (Peyrat et al., 2010; Delouis et al., 2009). The earthquake terminated in the south, beneath the center of Mejillones Peninsula.
Early aftershocks clustered in and around the northern slip patch, updip of the southern slip patch and around the outline of Mejillones Peninsula (Schurr et al., 2012). Some of the aftershocks offshore Mejillones clearly occurred inside the upper plate (Motagh et al., 2010; Schurr et al., 2012), and some few of the shallowest ones had extensional source mechanisms (Schurr et al., 2012). Fuenzalida et al. (2013) used data from a dense temporary network, installed shortly after the mainshock, to derive very well constrained aftershock hypocenters. Those sharply image the megathrust with a thickness of only about 2 km. Cross sections through the aftershocks indicate a splay fault offshore and a slight kink in the slab. A small amount of afterslip was detected beneath and offshore Mejillones Peninsula (Figure 11; Béjar-Pizarro et al., 2010), where

two early aftershocks with M_w >6 were located (Schurr et al., 2012). On Dec 16, 2007, a M_w 6.8 aftershock occurred directly beneath the southern slip maximum (Figure 11), at about 46 km depth. In contrast to other aftershocks, which had locations and focal mechanisms consistent with slip along the plate interface, the so-called Michilla event occurred inside the downgoing slab along a near-vertical plane extending from the plate interface to about 10 km into the Nazca Plate (Figure 11; Fuenzalida et al., 2013). Its slab-push mechanism was possibly facilitated by Coulomb stress increase due to the mainshock rupture (Peyrat et al., 2010). The Michilla event started an anomalously productive aftershock sequence (Figures 11 and 18) still active years later (Pasten-Araya et al., 2018) and even today (this catalog).

The 2007 Tocopilla earthquake occurred just north of Mejillones Peninsula, a prominent morphological feature along the Northern Chile coast (Figure 1), which was also the rupture limit of the 1995 M_w 8.1 Antofagasta earthquake to the south (Figure 11; Ruegg et al., 1996; Klotz et al., 1999; Chlieh et al., 2004). Juxtaposing the slip distribution and aftershock sequences of both earthquakes reveals a conspicuous symmetry. Both aftershock seismicity and slip abut in the center of Mejillones Peninsula but do not overlap (Figure 11). Events instead seem to skirt around Mejillones Peninsula, leaving its center relatively quiet (Schurr et al., 2012). This agrees with the observation by Béjar-Pizarro et al. (2013) that locking likewise skirts the peninsula, which implies that the megathrust immediately beneath Mejillones Peninsula moves predominantly aseismically and hence forms a barrier to rupture. Strong aseismic afterslip beneath the peninsula following the Antofagasta earthquake (Figure 11; Pritchard and Simons, 2006) and the general absence of interplate earthquakes in our catalog for this region (Figure 9) corroborates this inference. The Tocopilla earthquake also has interesting implications for the along-dip segmentation of the plate interface. It only ruptured the deeper part of the seismogenic megathrust, and neither afterslip nor aftershocks penetrated to the shallower, strongly locked megathrust north of Mejillones. Similar earthquakes of $7<M<8$ have been observed just north of the Tocopilla rupture area in 1967 (see above) and south of Mejillones Peninsula in 1987 and 1998 (e.g. Ihmlé and Ruegg, 1997; Pritchard et al., 2006), and other examples along the entire Chilean and Peruvian margin can be found (e.g. Pritchard et al., 2007; Bravo et al., 2019; Moreno et al., 2018). Different explanations for this along-dip segmentation of the megathrust have been suggested. Several studies (Contreras-Reyes et al., 2012; Béjar-Pizarro et al., 2010; Fuenzalida et al., 2013) propose a kink in the downgoing slab that could have acted as an along-dip geometric barrier to seismic rupture. Contreras-Reyes et al. (2012) infer such a kink at about 20 km depth when trying to reconcile active refraction seismic data from an amphibious experiment with hypocenters of Tocopilla earthquake aftershocks, and link its presence to the creation of the coastal scarp directly above (this notion was first proposed by Armijo and Thiele, 1990). The kink identified by Fuenzalida et al. (2013), however, is located 10 km deeper and features a more steeply dipping shallow segment (18° rather than 10°). Since the depths of aftershock hypocenters, especially offshore, are highly dependent on the utilized velocity model (Fuenzalida et al., 2013), it is not completely clear whether such a kink actually exists offshore along the Loa segment. It is certainly not an ubiquitous feature along the entire Chilean margin (counter-examples include Oncken et al., 2003; Storch et al., 2021), thus cannot explain the more general dichotomy of megathrust earthquakes in Chile. Several authors have argued that the observed duality between shallow large earthquakes and deeper, somewhat smaller events like Tocopilla is due to a frictional segmentation of the megathrust (e.g. Schurr et al., 2012; Moreno et al., 2018). Following this argumentation, events along the deeper portion of the megathrust would occur in a transitional segment that may be only partially locked in the interseismic time period.

4.4.2. The 2014 M_w 8.1 Iquique earthquake

On 1 April 2014, a M_w 8.1 thrust earthquake ruptured the central part of the Northern Chile seismic gap. Considering its size, the event caused relatively little damage and only few fatalities. A 2.1 m tsunami hit the nearby coast ∼20 minutes after the earthquake. The event occurred just north of a lowly locked zone, and in or near a region of relatively high locking in most locking models (Section 4.2, Figure 8). According to Vigny and Klein (2022), this location would be north of the 1877 rupture region and, if true, possibly repeating an event from 1871 (Section 4.1). The mainshock was preceded by a two-week long foreshock sequence with several M6+ events, likely accompanied by aseismic transients, and followed by an intense aftershock sequence including an M_w 7.6 event that extended the rupture region southwards. The earthquake sequence was well recorded by seismic and geodetic networks in place, making it one of the best studied subduction earthquakes worldwide. The long-term observation by both seismic and geodetic instruments allows analyzing stress build-up and deformation over weeks, months and years leading up to the event. In the following, we describe the observations and analysis for the interseismic phase (years to months before the event), the two-week foreshock sequence, the co-seismic rupture, as well as the post-seismic period.

Interseismic phase

The Iquique earthquake occurred in a region of relatively high background seismicity in the Northern Chile seismic gap. In the seven years before the mainshock, excluding the immediate foreshock sequence, it activated an arc-like structure around the eastern, down-dip side of the future rupture zone (Figures 12 and 27), including three M6+ events in 2008 and 2009 (Schurr et al., 2020), and M5+ events in August 2013 and January 2014 (Schurr et al., 2014). Since approximately 2011, the b-value, which is sensitive to stress, decreased significantly from 0.75 to below 0.6 in the source region, indicative of a stress increase (Schurr et al., 2014). Repeating earthquakes embedded on the down-dip side of the asperity were regularly active over 6 years with no sign of acceleration (Figure 12d; Schurr et al., 2020). Starting in July 2013, an event swarm became active (Aden-Antóniow et al., 2020) on the southern updip limit of mainshock slip, including several repeating earthquake sequences (Figure 12c; Kato et al., 2016; Schurr et al., 2020). The same cluster had been intermittently active in the years before. In January and February 2014, clusters both at the northern and southern edge of the future mainshock and near the M7.6 aftershock got initiated (Figure 12; Kato and Nakagawa, 2014; Kato et al., 2016; Schurr et al., 2020). The repeating earthquakes indicate less than 2 cm of accumulated aseismic slip for both episodes (Kato et al., 2016). Events during this period were deficient in high frequency radiation compared to earlier ones, indicating smaller stress drops or slower ruptures (Socquet et al., 2017; Piña-Valdés et al., 2018). Concurrently, westward displacement of nearby coastal continuous GNSS stations accelerated by up to 2 mm/a (Socquet et al., 2017). Inverting the velocity anomaly for slip on the plate interface yielded up to 1 cm of dominantly aseismic slip, mostly concentrated in a patch south of the mainshock asperity (Figure 12c; Socquet et al., 2017). The Iquique sequence was also recorded by an extremely sensitive long-baseline tiltmeter located near the coast slightly south of the mainshock rupture. After an interruption, recording restarted in December 2013 (Boudin et al., 2022). It showed several episodes of accelerated tilt in the months before the Iquique main event. Tilt is much more sensitive to the distance to the source than GNSS displacement and hence, in combination with GNSS data, constrains its location better. Boudin et al. (2022) also carefully reprocessed continuous GNSS data and analyzed them together with tilt data to reassess location and amplitude of possible precursory aseismic slip. They located it south of the mainshock rupture in the gap between the two asperities of the M_w 7.6 aftershock, mostly constrained by the tilt data. Aseismic magnitudes of $M_w \sim 6$ for the different episodes are retrieved (Boudin et al., 2022).

In summary, there are clear observations of transient deformation measured both with GNSS displacement and tilt in summer 2013 and early 2014, partly accompanied by the activation of earthquake clusters including repeaters. The observed deformation cannot be explained by the earthquakes alone and must be caused by a significant component of aseismic slip (Boudin et al., 2022). Similar observations of precursory aseismic slip, years or possibly even decades before the megathrust earthquake, were made for the time interval preceding the 2011 M_w 9.0 Tohoku-Oki earthquake in Japan (Ozawa et al., 2012; Mavrommatis et al., 2014; Yokota and Koketsu, 2015) and have been proposed to occur for large megathrust earthquakes globally (Igarashi and Kato, 2021). However, robust observations of such processes are scarce, and the Iquique earthquake is one of very few examples where such results have been obtained. However, also here there are still significant discrepancies between different studies concerning the location and amplitude of aseismic slip. We have to keep in mind that the observed deformations with magnitudes of $\sim$1 mm/d are at the verge of the achievable resolution, and observations are quite sparse, leaving their sources poorly defined. To resolve such signals better, more sites with both continuous GNSS and tiltmeters would be necessary.

The 16 March foreshock sequence and deformation transient

The foreshock sequence proper set off with a M_w 6.7 event on 16 March 2014, two weeks before the mainshock (Figure 12). The epicenter of this event was located just up-dip of the zone of highest mainshock slip.

It had a thrust mechanism striking at a high angle to the trench, significantly different from the low-angle thrusts typical for interplate events in northern Chile, which have their slip vectors aligned to the direction of plate convergence. It occurred above the megathrust in the upper plate (Ruiz et al., 2014; Hayes et al., 2014; Schurr et al., 2014, 2020), possibly on a continuation of similarly striking faults onshore (González et al., 2015). Within a few hours after this earthquake, another M_w 6.3 event broke at ∼5 km epicentral distance to the north, but with a deeper depth and a mechanism compatible with interplate motion on the megathrust (Figure 12a,b; Schurr et al., 2020). Over the following days, a cloud of events formed above the plate interface near the 16/03/2014 foreshock hypocenter, whereas seismicity on the plate interface spread north, including two more events of $M_w > 6$ with low angle thrust mechanisms (Figure 12b). The final foreshock stage included a NW-striking linear cluster of events that represents reactivation of an earlier cluster. The mainshock rupture initiated at the edge of this cluster. Together, the multi-year background seismicity, which skirted the downdip margin of the asperity, and the two-week foreshock sequence, which outlined the udip margin of the asperity, formed a ring around the mainshock rupture, a so-called Mogi Doughnut (Figure 12a; Schurr et al., 2020). The northward event propagation included numerous repeating event sequences (Kato and Nakagawa, 2014; Kato et al., 2016; Meng et al., 2015; Schurr et al., 2020). Compared to other observations of foreshock sequences preceding large megathrust earthquakes, which have occasionally also shown a clear directional propagation (e.g. Kato et al., 2012), the Iquique earthquake foreshock sequence appears rather prominent in terms of duration and moment release.

The foreshock sequence was accompanied by a clear displacement transient of several mm during the two weeks picked up by the coastal GNSS stations. There was some debate about whether this deformation could be explained by accumulated coseismic deformation due to the foreshocks (Schurr et al., 2014) or whether it requires aseismic slip (Ruiz et al., 2014). Ruiz et al. (2014) corrected the displacement time series only for the effect of the largest foreshock, but not for the other multiple M6+ and M5+ events. Bedford et al. (2015) graphed displacement vs. time against coseismic predictions including uncertainties in source location, mechanism and medium parameters, and found that the final GNSS displacements are within the uncertainty bounds of the coseismic predictions but that two episodes in which the trajectory clearly deviates from predictions may point, nonetheless, to some aseismic slip periods. In contrast, both Socquet et al. (2017) and Herman et al. (2016) found that coseismic displacement predictions are significantly smaller than observations. This debate has not reached a concensus to this date, as illustrated by two recent studies. On the one hand, Boudin et al. (2022) carefully reprocessed GNSS data for the entire preseismic period and found only small deviations from coseismic predictions, accounting only for a relatively small contribution from an aseismic source. Based on GNSS and tiltmeter data, they placed the aseismic source south of the main rupture, closely to where aseismic slip may have occurred in the months before. Location and magnitude of aseismic slip predicted by Ruiz et al. (2014), Herman et al. (2016), and Socquet et al. (2017) could not be reconciled with their data. On the other hand, Twardzik et al. (2022) concluded based on Bayesian

inference that aseismic slip should have accounted for ∼80% of the displacement for this time interval, and found that this aseismic slip initiated before the start of the foreshock sequence proper. Their aseismic slip patch is located offshore, in direct vicinity of where the M_w 6.7 foreshock of March 16 occurred.
Further indication for aseismic slip comes from multiple repeater sequences embedded in the propagating foreshock seismicity (Figure 12a Kato and Nakagawa, 2014; Kato et al., 2016; Meng et al., 2015; Schurr et al., 2020). Repeating earthquakes are commonly interpreted as recurrent small asperity failures driven by surrounding aseismic slip (e.g. Nadeau and Johnson, 1998). Accumulative aseismic slip up to 30 cm (Kato et al., 2016; Meng et al., 2015) was calculated based on repeater magnitudes and scaling relations, amounting to a moment magnitude M_w ∼6.7. This is similar to estimates deduced from GNSS data by Socquet et al. (2017), which even reached a magnitude ∼7. This contradicts the findings of Boudin et al. (2022), that allow only little aseismic slip (accumulated M_w <6.5) within the foreshock region to agree with the residual GNSS displacements.

In summary, there is some indication of aseismic slip accompanying the foreshock sequence from both GNSS transients and earthquake repeaters, but individual studies disagree on location and magnitude of this slip. Although the preseismic period has been comparatively well recorded by both seismometers and GNSS receivers, denser and possibly more sensitive observations would be needed to unequivocally untangle seismic and aseismic processes. Besides triggering of the main shock by an aseismic transient, it is also possible that the foreshocks triggered the mainshock as a cascading sequence, where each event successively triggered the next. This was tested by Herman et al. (2016), who found that each of the largest foreshocks, as well as the hypocenter of the mainshock, took place in an area of increased Coulomb failure stress, indicating that the propagating events consecutively pushed each other closer to failure. González et al. (2015) argued that the 16 March upper plate foreshock reduced normal stress and hence unclamped the megathrust, possibly also facilitating rupture.

The 1 April M_w 8.1 mainshock

The 2014 M_w 8.1 Iquique earthquake broke the mostly aseismic “hole” of the Mogi doughnut that was left behind by the background seismicity and foreshock series (Figure 12a; Schurr et al., 2020). Published models for the cumulative slip during the mainshock generally agree on a single main slip patch south and downdip of the epicenter, but differ in size and amplitude (peak slip from 4.5 m to >10 m) depending on the choice and weighting of the different data sets (e.g., InSAR, high-rate and static GNSS, teleseismic and nearfield seismic, tsunami), as well as the parameterization and regularization of the inversion (Figure 13; Yagi et al., 2014; Ruiz et al., 2014; Lay et al., 2014; Schurr et al., 2014; Gusman et al., 2015; Bai et al., 2014; Duputel et al., 2015; Liu and Zhou, 2015; Jara et al., 2018; Boudin et al., 2022). Only Jara et al. (2018)

imaged a second separate asperity further downdip near the coastline. Accordingly, stress drop estimates differ considerably, with resulting values of ∼2.6 MPa from a teleseismic and tsunami inversion (Lay et al., 2014), 3 MPa from teleseismic, strong-motion and geodetic data (Liu and Zhou, 2015), 7.8 MPa from strong-motion and GNSS (Jara et al., 2018), 10 MPa using strong-motion, geodetic and tsunami data in a Bayesian inversion (Duputel et al., 2015) and 20 MPa from spectral ratios (Frankel, 2022). Both kinematic inversion (Schurr et al., 2014; Lay et al., 2014; Duputel et al., 2015) and high-frequency backprojection (Schurr et al., 2014; Lay et al., 2014; Meng et al., 2015) image a rupture propagation down-dip towards the SE. The rupture started slowly, with little moment release during the first 20 sec (e.g. Schurr et al., 2014; Duputel et al., 2015; Liu and Zhou, 2015; Jara et al., 2018) until the main asperity was reached. The entire rupture lasted for more than a minute. Backprojection indicates a complex kinematic pattern towards the end of the rupture, including a reactivation of the epicentral region (Schurr et al., 2014; Meng et al., 2015). Models employing tsunami data (An et al., 2014; Lay et al., 2014; Gusman et al., 2015; Bai et al., 2014; Duputel et al., 2015), which have the best resolution offshore, indicate that the rupture did not extend into the shallowest part of the megathrust. The updip termination of the rupture may have been preconditioned by the nature of the overlying upper plate wedge. Ma et al. (2022) reprocessed seismic reflection lines acquired offshore years before the Iquique earthquake, and found high reflectivity in the updip part of the megathrust as well as laterally beyond the rupture. In the region of the main shock rupture, in contrast, reflectivity was observed to be low to moderate. The observed high reflectivity in the shallowest part of the megathrust is probably caused by high fluid pressure, fostering stable slip and hence limiting the extent of the earthquake. Alternatively, it was also proposed that along-dip variations in slab topography may have prescribed the extent of the main shock rupture, with an extended topographic low coinciding with the rupture extent, whereas a topographic high directly updip may have inhibited rupture towards the trench (Storch et al., 2023). In along-strike direction, maps of interplate locking (Figure 8) appear to prescribe the extent of the Iquique rupture. Both to the north of the main shock as well as south of it, regions of rather low locking that may act as rupture barriers have been obtained, although the April 3 aftershock (M_w 7.6) apparently ruptured inside the lowly locked region to the south of the main shock (Figure 12a). Geersen et al. (2015) also found evidence for seamounts in time-migrated seismic reflection data along the updip and southern limits of main shock slip, suggesting that downgoing plate structure may have limited the rupture extent. However, this was challenged by Storch et al. (2021) who argue that the topographic high of reflectivity along the plate interface vanishes after depth migration and may therefore be caused by the medium velocity structure. Nevertheless, the presence of the Iquique Basin, a prominent depocenter in the marine forearc (Coulbourn, 1981; Reginato et al., 2020; González et al., 2023, see gravity map in Figure 8) appears to correlate with the extent of both the mainshock rupture and the locking high. A long-wavelength along-strike undulation of slab surface topography (Storch et al., 2023; Schaller et al., 2015) was suggested to underlie the Iquique Basin.

The postseismic period

On 3 April, three days into the postseismic period, a M_w 7.6 aftershock occurred about 100 km to the south of the mainshock epicenter. It started from a relatively shallow hypocenter and propagated downdip. The rupture shows two clearly separated asperities, the deeper one below the coast (Schurr et al., 2014; Duputel et al., 2015; Liu and Zhou, 2015; Jara et al., 2018; Boudin et al., 2022). The second largest aftershock with M_w 6.6 occurred only $\sim$2.5 minutes after and within the coda of the mainshock, and was located approximately between mainshock and M_w 7.6 aftershock (Bindi et al., 2014). Soto et al. (2019) studied the aftershock sequence in detail, and found that aftershocks concentrated mainly in two bands updip and downdip of the main asperity. The updip region is clearly separated from the trench (by about 30 km; Petersen et al., 2021) and contains conspicuous west-trending streaks (visible in Figure 6), which include embedded earthquake repeaters. These streaks, however, were not found by an OBS survey eight months after the mainshock (Petersen et al., 2021), which could either imply that they are a location artifact due to unfavorable event-station geometry, or that their activity was limited to the early part of the aftershock sequence. The updip limit of both coseismic rupture and the occurrence of aftershocks is probably limited by the onset of the frontal prism, which is characterized by low velocities in active and passive seismic studies (Petersen et al., 2021; Storch et al., 2021; Reginato et al., 2020; Maksymowicz et al., 2018). The lower band of aftershocks shows strong upper plate activation, with some extensional faulting (Cesca et al., 2016), indicating splay faulting (Soto et al., 2019) and significant megathrust topography. These aftershocks reach depths up to 60 km below land. Apart from the onset of extensional faulting, there is no significant change in the stress regime between the pre-seismic and post-seismic periods (Cesca et al., 2016). Postseismic stress heterogeneity, however, is indicated by strongly clustered and patchy seismicity (Soto et al., 2019) and a larger heterogeneity of source mechanisms (Cesca et al., 2016; León-Ríos et al., 2016). Postseismic slip has been obtained by inverting continuous GNSS data, showing a concentration of afterslip in two lobes north and south of the main asperity (Figure 12a; Hoffmann et al., 2018; Shrivastava et al., 2019). The northern lobe is almost completely aseismic, indicating that the megathrust here has velocity-strengthening frictional properties, in accordance with most locking models (Figure 8). The southern lobe overlaps with the M_w 7.6 aftershock rupture and is mostly surrounded by aftershock seismicity clusters, indicating heterogeneous frictional properties. Postseismic westward GNSS displacement is separated from interseismic eastward displacements across an apparently sharp boundary at $\sim$21°S (Hoffmann et al., 2018).

4.4.3. The remaining seismic potential

It is clear that the two most recent large earthquakes around the Arica Bend, the 2001 M_w 8.5 Arequipa event in southern Peru (Ruegg et al., 2001; Perfettini et al., 2005) and the M_w 8.1 Iquique event in northern Chile, did not close the gap left behind by the great 1868 and 1877 events (Figure 1). Large sections north and south of the Iquique rupture remain unbroken. The gap north of the Iquique event is quite elusive. Practically all locking models (Figure 8) show low locking there, but this may be an artefact due to the westward curvature of the trench here, which makes its distance to the coast increase, causing a deterioration of observational conditions. Likewise, the national boundary to Peru limits both the seismic and geodetic networks. Seismicity on the megathrust is low in this region, and at least immediately north of the Iquique rupture well enough resolved to be trustworthy. The coincidence of postseimic slip and the lack of aftershocks are strong hints that this section creeps aseismically and hence may form a barrier to seismic rupture. However, its northward extent and the behavior across the border to Peru is unclear. Only combining measurements from Chile and Peru can eventually cast more light on this region in the future. The area south of the Iquique ruptures, all the way to Mejillones Peninsula, is clearly imaged as a strongly locked patch in all locking models (Figure 8). It is now framed by recent large earthquakes on all sides, including its downdip part. The upper part of the megathrust there is seismically completely quiet, whereas the lower part shows the strongest background seismicity in our catalog. Concentrations of seismicty outlining locked asperities at depth have been observed for the Iquique event (Schurr et al., 2020) and in central Chile (Sippl et al., 2021), and may hint at stress build-up in the late interseismic period. The gap south of the Iquique ruptures probably coincides with the rupture of the 1877 event (Vigny and Klein, 2022), and if fully locked, as it appears, would have accumulated some 10 m of slip deficit, enough for at least a magnitude 8.5 event. This is likely the most mature seismic gap left along the Chilean margin (Lay and Nishenko, 2022). The Iquique earthquake demonstrated that having permanent observation infrastructure in place is essential and gainful in order to advance our understanding of megathrust behavior before, during and directly after a large earthquake. However, it also demonstrated that preseismic phenomena are so subtle that the existing observational infrastructure is not sufficient to unequivocally resolve them. Densification of existing seismic and geodetic networks, new measurements like e.g. tilt or strain, as well as the instrumentation of the offshore realm would be necessary in order to advance our detection capabilities in the advent of the next great earthquake, which would also advance our field as a whole.

5. The downgoing plate

Although the primary seismic hazard in Northern Chile stems from large earthquakes on the megathrust, the region has also experienced two strong intermediate-depth intraslab earthquakes of M$\sim$8 at depths of $\sim$100 km over the last century, the 1950 Calama earthquake (Kausel and Campos, 1992) and the 2005 Tarapacá earthquake (Peyrat et al., 2006; Delouis and Legrand, 2007). As the properties of the downgoing plate as well as their spatial variations are a key factor that governs subduction zone structure (including the long-term and short-term behavior of the megathrust), we here compile published knowledge on the downgoing plate's seismicity (Section 5.1) and its geometry, velocity and attenuation structure (Section

5.2). In Section 5.3, we then discuss a number of currently unresolved issues about the downgoing Nazca Plate in Northern Chile.

5.1. Intraplate Seismicity

Event geometry

In the offshore part of the Nazca Plate, the IPOC seismicity catalog shows virtually no seismicity beyond the trench (Figure 6). This stands in contrast to other subduction zones around the world, where Outer Rise seismicity is a common phenomenon (e.g. Craig et al., 2014). Global compilations of Outer Rise seismicity, which are based on global earthquake catalogs and hence only contain larger earthquakes (M>∼4.5), do not show Outer Rise events for Northern Chile either. However, the long-term catalog of the CSN (Barrientos, 2018) shows a small population of Outer Rise events between 21 and 22.5°S. Due to the location of these events far outside the station network, it is quite possible that the automated approach used for compiling the IPOC catalog failed to detect them.
Inside the downgoing slab beneath the Northern Chile forearc and arc, background seismicity rates are extremely high, which has been visible in seismicity studies over the decades (e.g. Barazangi and Isacks, 1976; Cahill and Isacks, 1992; Bloch et al., 2014; Sippl et al., 2018). In the 15 years spanned by the IPOC catalog, the amount of intraslab earthquakes totals nearly 10 times that of plate interface events (see Section 3), even though the latter group contains the prominent aftershock series of the 2007 Tocopilla and the 2014 Iquique earthquakes (Section 4.4). This stands in contrast to the regions immediately south (Copiapó region; e.g. Pasten-Araya et al., 2022) and north (southern Peru; e.g. Cahill and Isacks, 1992; Gutscher et al., 2000), where a much larger proportion of the background seismicity occurs on the plate interface. Intraslab seismicity in Northern Chile shows a prominent transition in downdip direction (Figure 7). At depths of <∼90 km, a double seismic zone (DSZ) with about 20 km separation distance between upper and lower plane is visible (see Figure 4, Sippl et al., 2018). DSZs are common features in subduction zones, and may be near-ubiquitous globally (Brudzinski et al., 2007; Sippl et al., 2022). At depths beyond ∼90 km, no DSZ can be observed any more, and seismicity outlines an about 25 km thick highly seismogenic volume (see profiles in Figure 7). The transition between DSZ and the thicker cluster is sharp and near-vertical (Sippl et al., 2019), although its appearance and position varies along strike.

Drastically increased seismicity rates and a thicker seismogenic volume at these depths were observed in previous local studies (e.g. Schurr et al., 1999; Haberland and Rietbrock, 2001) as well as using teleseismic depth phases (Craig, 2019), while two studies (Rietbrock and Waldhauser, 2004; Florez and Prieto, 2019) have also reported the existence of a DSZ to larger depths. Upon closer inspection, these results are not contradictory, but it appears that both observations are valid for different areas. Shape and event rates in both the DSZ and the deep cluster vary strongly along strike (Figure 7). North of 20°S, the lower plane of the DSZ is only very faint, and activity levels in the deep cluster are lower than further south. At the same time, the cluster terminates at a depth of ∼110 km, shallower than further south. North of 18.5°S, where the IPOC catalog has no resolution, a local seismic experiment showed that while the drastic increase in event numbers at ∼90 km depth is also observed there, the two planes of the DSZ remain distinguishable within the deep cluster in this region (Comte et al., 1999; Dorbath et al., 2008). This can also be observed in our northernmost cross sections (Figure 7). The slab to the north of 20°S appears to have a constant dip of about 25°. Between 20.5 and 22°S, event rates in the deep cluster are highest, and the DSZ at shallower depths is clearly outlined (Figure 7). The lower plane of the DSZ has its updip termination at only ∼45 km depth around 21°S, and shows a higher activity level than further north or south. Within the deep cluster, activity fills the entire ∼25 km thickness from close to the slab surface to the depth of the DSZ lower plane further updip. Two lateral offsets of the seismicity can be observed at 21 and 21.6°S; they are visible in map view (Figure 6) and by comparing the different profiles on either side of them (Figure 7). As shown in Sippl et al. (2018), these offsets do not represent tears or discontinuities in the subducting slab, but instead comprise sharp along-strike changes of the onset and termination of the seismically active volume within a continuous slab that does not show short-wavelength geometry changes. The general slab shape south of ∼21°S, however, is distinct from further north; it shows a flattening of the slab at depths of ∼70-80 km, followed by a steepening at depths of ∼110-120 km, roughly coincident with the downdip termination of the seismically highly active cluster (Sippl et al., 2019). South of 22°S, seismicity rates in the downgoing slab decay again. This may partially be due to the network geometry that was used for the IPOC catalog, but larger-scale studies with networks extending further south (e.g. Cahill and Isacks, 1992; Barrientos, 2018) made a similar observation. As north of ∼20°S, the DSZ lower plane is near-absent, and the intermediate-depth cluster is weaker and appears to feature two planes of increased activity again. This latter observation may be consistent with Rietbrock and Waldhauser (2004).

At ∼24°S, a cluster of strong, persistent seismicity is located at about 200-250 km depth, beneath the Chile-Argentinian border (Valenzuela-Malebran et al., 2022; Schurr et al., 1999). This "Jujuy cluster" occurs beneath where the volcanic arc is deflected eastwards (see Figure 1), and regularly features large earthquakes with magnitudes up to ∼6.5. While this feature was contained in an earlier version of the IPOC catalog (Sippl et al., 2018), it was removed in the present version due to its location far outside the station network, which would lead to a highly incomplete catalog with substantial location scatter and uncertainties. More weakly active structures at ∼200 km depth are retrieved east of the Argentinian border between 21 and 23°S (Figure 6).

Source properties

Stress drops for intraslab earthquakes were found to fall into the range 7-30 MPa (Cabrera et al., 2021; Herrera et al., 2023b), with the 2005 Tarapacá earthquake featuring a value at the upper end of that range (Kuge et al., 2010; Peyrat et al., 2006). Although these studies only investigated a small number of earthquakes, the results are in general agreement with values for intermediate-depth earthquakes in other subduction zones (e.g. Kita and Katsumata, 2015) as well as global compilations (Poli and Prieto, 2016), all of which have concluded that intraslab earthquakes feature higher stress drops than plate interface or intracrustal earthquakes. Derode et al. (2019) also found that intraslab events in Northern Chile likely have higher rupture velocities and suggested that their ruptures are shorter and more impulsive.

When looking at focal mechanisms, the overwhelming majority of intraslab earthquakes in Northern Chile show mechanisms with their T-axes oriented approximately E-W with a dip of 20-30°, i.e. aligned with the dip of the slab (Figures 15 and 16). Such downdip extensive (DDE) mechanisms are found throughout the highly active volume of seismicity at depths of ∼100 km (Rietbrock and Waldhauser, 2004; Bloch et al., 2018b; Sippl et al., 2019), in the deeper clusters across the Argentinian border (e.g. Schurr et al., 1999) as well as in the DSZ lower plane (Bloch et al., 2018b; Sippl et al., 2019). A more detailed look into the along-strike variation of T-axis azimuths reveals a deviation from the near perfect E-W orientation (azimuth ∼90°) to a more NNE-SSW orientation (azimuth ∼60°) between 20.5 to 21.5°S (see also Cesca, 2020). The upper plane of the DSZ shows an along-dip flip in focal mechanism orientation (Figure 15), from compressive mechanisms at shallower depths to DDE for deeper events, with a sudden transition between the two regimes at ∼60 km depth (Figure 15). As already noted by Bloch et al. (2018b), the shallow compressive intraslab mechanisms are not downdip compressive, with P-axes oriented along the slab and T-axes perpendicular to the slab dip. Rather, P-axes are oriented at an angle of 30-45° relative to the slab orientation. An earlier study in the very north of the area of interest has shown much more scattered results than what was retrieved here (Comte et al., 1999), but this may have been a result of using first motion polarities for focal mechanism retrieval with a very small seismic network.

Temporal evolution and magnitude-frequency trends

Figure 6 shows the temporal evolution of seismicity in the years 2007-2021. It can be recognized that the overall rate of intraslab events in the IPOC catalog has decreased from 2014 to 2021, which should mostly be due to changes in station geometry as well as prolonged station outages (see also Figure 17, blue curves). When only considering events of magnitude 2.7 and above (the overall completeness magnitude estimate of Hainzl et al., 2019), the trend of overall decreasing event numbers is hardly visible any longer (Figure 17), indicating that the main effect is not a true decrease of event rate, but a decrease in the detection capability of the station network. However, a substantial, continuous and robust decrease in event numbers is obtained when only looking at intermediate-depth events around 20°S, a trend that is also visible for M>2.7 events. This trend is likely connected to the 2005 M_w7.8 Tarapacá earthquake, which was the most prominent intermediate-depth earthquake in Northern Chile since 1950 and occurred in the northern part of our study area at a depth of approximately 100 km (e.g. Peyrat et al., 2006). As the Tarapacá event itself occurred before the start of the IPOC catalog, we use aftershock locations from a rapid-response local network (Peyrat et al., 2006) to identify its location relative to features in our catalog. These early aftershocks outline a gently west-dipping structure situated inside the highly seismogenic cluster we retrieve (yellow stars in Figure 14) and extending from ∼19.7 to 20.25°S along-strike. This along-strike extent is largely consistent with published rupture models of the Tarapacá main shock (Delouis and Legrand, 2007; Kuge et al., 2010). When we consider IPOC catalog event numbers for ID events only in this latitude range, we see a clear decrease of event rates from 2007 all the way to 2021, which is also robustly retrieved for events with M>2.7 (Figure 17). This implies that the 2005 Tarapacá earthquakes locally triggered increased rates of intraslab earthquakes for more than a decade.

Compared to seismicity on the plate interface, intraslab seismicity in Northern Chile is much less clustered in time, and to first order resembles constant background activity (Sippl et al., 2019). However, larger intraslab events still create aftershock series (e.g. Cabrera et al., 2021), although most of these are significantly less pronounced than for plate interface events of comparable magnitude, and there appears to be a subtle general trend of decreasing aftershock productivity with depth (Wimpenny et al., 2022), similar to observations in other subduction zones (Gomberg and Bodin, 2021; Chu and Beroza, 2022). Cabrera et al. (2021) analyzed six aftershock series in detail and found that aftershock productivity appears to decrease with depth below the slab surface, which they interpreted as aftershock productivity being related to hydration of the downgoing lithosphere. However, the much larger dataset analyzed by Wimpenny et al. (2022) did not show such a clear relationship, and most likely heterogeneity in several parameters (slab hydration being one of them) contribute to the observed differences in aftershock productivity. Figure 18 shows examples of aftershock sequences for M∼6 events in different settings within our catalog. While both chosen examples for event class ID, situated inside the deeper cluster of seismicity at depths >100 km, as well as the lower plane example show virtually no afterchocks, the Michilla event that occurred in the downgoing oceanic crust (Section 4.4.1) had a vigorous aftershock series with a longevity in excess of comparable series on the plate interface.

B-values of intraslab earthquakes in Northern Chile were found to be significantly higher than those of plate interface events (Legrand et al., 2012; Hainzl et al., 2019; Poulos et al., 2019; Sippl et al., 2019), although the exact values for the different event populations vary between studies. Sippl et al. (2019) separately analyzed the different intraslab populations, i.e. earthquakes in the upper and lower plane of the

DSZ and in the intermediate-depth cluster, and found that the intermediate-depth cluster has a significantly higher b-value than the DSZ further updip. This can also be seen in the maps of Legrand et al. (2012). When looking at the along-strike variation of b-values, Geersen et al. (2022) found that it is dependent on the depth within the slab. Whereas events close to the slab surface to first order feature constant b-values along strike, there are much larger variations in b-value for events deep inside the slab, with a clear maximum in the region between ∼20.7 and ∼22°S.

5.2. Structural observations

In the offshore part of the forearc, landward of the trench, seismic tomography studies of the downgoing slab show reduced v_p values (and increased v_p/v_s) in the oceanic crust and possibly into the uppermost mantle (Husen et al., 2000; Petersen et al., 2021). Such a reduction in shallow P-wavespeeds is also seen in active seismic studies (e.g. Ranero and Sallarès, 2004; Myers et al., 2022) and is likely due to partial serpentinization. Below the onshore part of the forearc, receiver function studies have imaged the downgoing oceanic crust as a 5-10 km thick low-velocity layer atop the descending slab, with a S-wavespeed contrast relative to the underlying mantle lithosphere of around 15% (Yuan et al., 2000). This low-velocity layer fades and eventually becomes invisible at depths of 100-120 km in migrated images (Yuan et al., 2000; Wölbern et al., 2009), whereas a faint trace of it can be discerned to deeper depths in unmigrated waveforms (Wölbern et al., 2009). When comparing receiver function results with seismicity, it becomes apparent that the upper plane of the DSZ is located close to the oceanic Moho, but likely still within the oceanic crust (Bock et al., 2000; Sippl et al., 2018), while the intermediate-depth cluster of seismicity is nearly entirely situated in the oceanic mantle lithosphere (ANCORP_working_group, 1999; Oncken et al., 2003; Sippl et al., 2018). Comparison of receiver function profiles at 20 and 22°S (Sodoudi et al., 2011) shows the changes in slab geometry (steeper, constant subduction angle in the north, slab flattening in the south) that were already seen in the seismicity distribution. Observations of guided waves that propagate in the crustal wave duct require a much thinner low-velocity layer of 1-4 km thickness that is continuous to depths in excess of 180-200 km (Martin et al., 2003; Garth and Rietbrock, 2017), as well as a kink in the slab at about 100 km depth that allows the guided waves to exit the crustal waveduct.

The downgoing Nazca Slab shows up as a continuous high-velocity and low-attenuation feature in a wide range of seismic tomography studies that use local and regional sources (e.g. Myers et al., 1998; Graeber and Asch, 1999; Haberland and Rietbrock, 2001; Schurr et al., 2006; Huang et al., 2019; Gao et al., 2021), whereas a number of studies that used teleseismic earthquakes could only image it robustly when using *a priori* constraints (e.g. Heit et al., 2008; Scire et al., 2015). It does not show first-order variations of velocity parameters or geometry within the study region and appears to be continuous beyond the bottom of the mantle transition zone (Bijwaard et al., 1998; Scire et al., 2015; Faccenna et al., 2017; Portner et al., 2020). Whereas values of P-wave attenuation (Q_p ~1000; Haberland and Rietbrock, 2001; Schurr et al., 2006) and v_p/v_s (~1.73-1.75; Schurr et al., 2006; Koulakov et al., 2006; Comte et al., 2016) do not vary significantly along strike, Gao et al. (2021) observed faster v_s values in the downgoing Nazca Plate south of 21°S, which can also be recognized in Schurr et al. (2006). Further south, v_s inside the slab appears to decrease again from 24°S southwards, accompanied by decaying intraslab seismicity (Gao et al., 2021). In downdip direction, some studies have obtained a sudden increase of v_p in the downgoing slab, from ~8 to ~8.5 km/s, at a depth of about 70 km (Graeber and Asch, 1999; Huang et al., 2019).

As most published studies have used intraslab seismicity as sources for the tomography, only the uppermost part of the downgoing slab is well resolved. Information on possible changes of seismic velocities with depth inside the slab is thus rare, and existing results are contradictory. The study of Dorbath et al. (2008) obtained large variations of both v_p and v_s between upper plane, intermediate region and lower plane of the DSZ in the very north of the study area. In their model, v_s is high (>4.6 km/s) everywhere, but v_p is reduced in the upper plane (7.7 km/s) as well as in the lower plane (7.4 km/s), but strongly elevated between (8.5 km/s). This leads to a high-v_p/v_s region between the planes of the DSZ, framed by low-v_p/v_s where the seismicity is located. Using the same dataset, Comte et al. (2016) retrieve intermediate to low values of v_p/v_s for all depths within the slab, which appears to be corroborated by teleseismic residuals of sP and pP from autocorrelations (Fang and van der Hilst, 2019). Bloch et al. (2018a), in contrast, obtained very high v_p/v_s values of ~2 about 30 km below the slab top by directly estimating v_p/v_s from traveltime differences (Lin and Shearer, 2007).

Anisotropy results for the downgoing Nazca Slab show an along-dip change from trench-normal fast directions in the shallow slab to trench-perpendicular fast axis orientations at deeper depths (Huang et al., 2019)

5.3. Processes

5.3.1. What mineralogical processes are responsible for the along-dip variation of seismicity?

Intermediate-depth seismicity in downgoing oceanic lithosphere is linked to the breakdown of hydrous minerals inside the slab (e.g. Peacock, 2001; Hacker et al., 2003a,b; Zhan, 2020). These hydrous phases originate mainly in the Outer Rise region of a subduction zone, where the plate gets bent and thus opens pathways for water to infiltrate deep into oceanic crust and lithosphere (Ranero et al., 2003; Cai et al., 2018). While the exact mechanism of intermediate-depth seismogenesis is still debated (e.g. Ferrand et al., 2017; Zhan, 2020), the link to the dehydration of hydrous minerals is widely accepted. Globally, earthquakes at intermediate depths tend to form double seismic zones (DSZs), i.e. alignments of two parallel planes of earthquakes separated by an aseismic region in-between (e.g. Brudzinski et al., 2007; Florez and Prieto, 2019). The most widely accepted explanation for this phenomenon is that the two planes represent the dehydration of different mineral phases. The lower plane is usually found close to the 600-650°C isotherm and has been linked to the dehydration of antigorite in oceanic mantle lithosphere (Peacock, 2001), whereas the upper plane may be linked to the eclogitization of gabbroic oceanic lower crust (e.g. Kita et al., 2006).

The observed seismicity inside the downgoing Nazca Plate in Northern Chile deviates significantly from global observations. While a double seismic zone is present at shallower depths, it disappears at $\sim$100 km depth, where a highly active, 25-30 km thick cluster of seismicity is observed (see Section 5.1; Figure 7). Although the regions in the north and south of the study region show a somewhat different geometry of the intermediate-depth cluster, the sudden increase of seismicity rates at this depth is observed everywhere along the Northern Chile subduction zone. Attenuation and v_p/v_s inside the mantle wedge directly above this cluster are significantly elevated (see Section 6; Graeber and Asch, 1999; Haberland and Rietbrock, 2001; Schurr et al., 2006), which can be interpreted as the signature of fluids that were liberated through dehydration reactions in the slab rising into the overlying mantle (e.g. Contreras-Reyes et al., 2021a). Thus, the observed along-dip transition likely corresponds to a sudden increase in the rate of dehydration reactions along dip. Although there are many hydrous phases whose breakdown could potentially occur in the pressure-temperature range investigated here (Ferrand, 2019), most of those are unlikely to be present in significant quantities. Antigorite dehydration, the most commonly invoked such reaction, occurs at a near-constant temperature of 600-650°C, which stands in contrast to the observation that the onset of the deep seismicity cluster clearly cuts across isotherms (Figure 19).

Sippl et al. (2019) proposed a conceptual model in which the seismicity cluster occurs due to a feedback loop initiated by temperature input into the slab from the overlying mantle wedge. The onset of the seismicity cluster is located where the slab top reaches the hot part of the overlying mantle wedge, so elevated temperature input there could cause some of the metastable antigorite in the slab to dehydrate. The densification of the slab that accompanies this reaction could then lead to an increase in strain rate due to slab bending, which again leads to an increased rate of antigorite dehydration. Such a setup could invoke a reaction cascade that may explain the abundance of seismicity at these depths. Obviously, many open questions remain around this feature, for instance it is unclear why it is not present further north or south along strike of the South American margin, where seismicity rates at intermediate depths are much lower (see Section 5.3.2; e.g. Cahill and Isacks, 1992). Globally, some trench-parallel belts of increased intraslab seismicity have been observed elsewhere (Kita et al., 2006; Ratchkovski and Hansen, 2002), but none of them feature geometries or event rate contrasts comparable to Northern Chile. This is surprising considering that Northern Chile is not at the extreme end of any of the most important subduction zone parameters, featuring downgoing crust of medium age ($\sim$50 Ma) and a moderate to fast subduction speed, leading to a thermal parameter of $\sim$1700, in the midfield of global subduction zones (Syracuse et al., 2010). However, the fractured nature of the seafloor offshore Northern Chile, with its prominent horst-and-graben structures nearly devoid of overlying sediments (e.g. Geersen et al., 2018), may allow for stronger hydration at the Outer Rise compared to other regions.

5.3.2. Anomalous seismicity features around 21° S

The shape of the Nazca Slab in Northern Chile is not constant along strike, but undergoes a transition from a straight geometry in the northern part of the study area (e.g. Comte et al., 1999) towards a more complex and partially flattened geometry south of about 21°S (Figure 14; e.g. Hayes et al., 2018; Sippl et al., 2018; Sandiford et al., 2020), where it may start to grade into the Pampean flat slab further south (Ramos et al., 2002). At the same time, we observe the highest event numbers of intraslab earthquakes at latitudes between about 20.8 and 21.6°S (Figure 6), with event numbers decreasing to the north and south of this segment. This observation can not only be an effect of instrumental coverage, as the CSN catalog (which has wider coverage at least to the south) shows a similar trend. At 21 and 21.6°S, two offsets of the intraslab seismicity are visible both in map view and in depth (Figure 6; more detail in Sippl et al., 2018). The lower plane of the DSZ is most pronounced at around 21°S, where it is pervasively active from depths as shallow as 45-50 km all the way to the deep cluster. Thus, we observe clearly increased seismicity especially deep inside the slab in a narrow along-strike region of the Northern Chile subduction zone.

Although some recent studies have claimed that some of the deeper intraslab seismicity may occur in a dry setting (e.g. Cabrera et al., 2021), it is commonly assumed that the occurrence of intermediate-depth seismicity is directly linked to deep slab hydration (e.g. Ranero et al., 2005), and event rates deep in the slab may be directly related to the presence or absence of hydrous minerals there (e.g. Geersen et al., 2022). This could imply that a slab segment with elevated (deep) hydration is subducted around 21°S. The hydration of the downgoing oceanic lithosphere is in most places related to faulting in the Outer Rise region, where normal faulting due to plate bending allows water to infiltrate deep into the oceanic plate (e.g. Faccenda et al., 2012). Increased fracturing of the seafloor in the Outer Rise region often occurs where features such as ridges, seamount chains or fracture zones are subducted (e.g. Sun et al., 2020), and the creation of these features may have already led to some hydration of the oceanic plate as well. Thus, increased rates of intermediate-depth seismicity can be expected where such a seafloor feature is subducted (e.g. Kirby et al., 1996; Shillington et al., 2015). It could thus be speculated that the increased event rates and deeper extent of seismicity between 20.8 and 21.6°S are a consequence of a subducted seafloor feature. The only such feature currently impinging onto the Northern Chile trench is the NE-to-NNE striking Iquique Ridge (Figure 1), a hotspot track that formed 45-50 Ma ago and started colliding with South America 40 Ma ago (Bello-González et al., 2018; Contreras-Reyes et al., 2021b). It features clearly elevated crustal thickness of up to 13 km close to the trench (Myers et al., 2022) and possibly more further offshore (Tassara et al., 2006), compared to an oceanic crust of 6 to 8 km thickness elsewhere offshore Northern Chile (see Figure 20; Patzwahl et al., 1999; Ranero and Sallarès, 2004; Tassara et al., 2006). While diminished crustal and possibly uppermost mantle P-wavespeeds, which may indicate pervasive hydration, have been imaged along the Iquique Ridge (Myers et al., 2022), the depth region of the DSZ lower plane or most of the activity of the deep cluster have not been resolved.

While the Iquique Ridge is a feature that could potentially create a signature like the one we observe at depth, its strike direction and location offshore is not compatible to the location of the seismicity anomalies (see Figure 1). The Iquique Ridge impinges onto the trench offshore Northern Chile around 20.5°S (Ma et al., 2023), and strikes NE to NNE, so that it should be situated more than 100-150 km north of where we observe the seismicity anomalies at depth. Moreover, it is unclear whether a significant portion of it has already been subducted, since several studies have deduced that its initial contact with the Northern Chile trench may only have been about 2 Ma ago (e.g. Rosenbaum et al., 2005; Bello-González et al., 2018). It thus appears unlikely that the increased hydration and intriguing geometries we observe at depth around 21°S can be linked to the Iquique Ridge. On the other hand, the Iquique Ridge is not a strictly linear feature offshore, but consists of several prominent seamounts that do not follow any simple linear trend (Figure 1), so that we cannot exclude that what we observe is an eastward protrusion off the main strike direction of the ridge. At the same time, seismicity rates at depth appear to correlate with the faulting pattern of the seafloor that is currently being subducted, with the region around 21°S corresponding to an area where two to three different fabric orientations are present, whereas only a single one dominates further north and south (Geersen et al., 2018, 2022). This may indicate that a more subtle difference in seafloor morphology, not necessarily involving a large feature like a seamount chain, can already have a significant influence on observed seismicity rates at depth.

5.3.3. What controls the intraslab stress field?

The pattern of intraslab stresses in Northern Chile, as outlined by earthquake focal mechanisms (Figure 15), is unusual in a global context. Following early findings in Japan and the Aleutians (Hasegawa et al., 1978; Engdahl and Scholz, 1977), double seismic zone earthquakes are thought to exhibit downdip compression in the upper plane and downdip extension in the lower plane, which has been associated with the unbending of the plate (e.g. Kawakatsu, 1986). While the downgoing Nazca Plate in Northern Chile shows such a pattern at shallow depths, its upper plane exhibits a flip of mechanisms to downdip extensive at a depth of ∼60-65 km, while the lower plane stays downdip extensive. The highly active cluster at deeper depth is likewise homogeneously downdip extensive. Interestingly, a downdip change in slab anisotropy appears to mirror the observed mechanism flip near the slab surface (Huang et al., 2019).

Different explanations for these findings have been proposed. Sandiford et al. (2020) and Cabrera et al. (2021) associate the change in mechanism signature with a transition from slab unbending to slab bending. This is compatible with the slab geometry (e.g. Figure 14), which shows a shallowing followed by slab steepening where the deeper cluster of earthquakes is located. Steady-state estimates of plate bending or unbending (from Sippl et al., 2022, shown in Figure 15) appear to confirm this (also seen by Sandiford et al., 2020). With this model, however, it is difficult to explain the missing flip to compressive mechanisms deeper inside the slab, so that no bending signature (i.e. extensive over compressive mechanisms) is observed there. In the aforementioned studies, the authors argue that the addition of in-plane extension due to slab pull may shift the plane of neutral stress deeper inside the slab, so that the compressive deeper part is not sampled by the seismicity, which is confined to the uppermost ∼30 km of the slab (e.g. Figure 7).

Other studies have noticed that the mechanism flip in the upper plane coincides with the downdip termination of seismicity along the plate interface (see Figure 15; Bloch et al., 2018b; Sippl et al., 2019; Comte et al., 1994). The observed pattern of stress orientations could thus also be explained by a dominance of in-plane extension (e.g. due to slab pull) in the slab, modified by compressive stress due to friction on the plate interface, which gets transmitted into the slab (Sippl et al., 2022). In a purely elastic slab, (un)bending stresses are much larger than stresses on the plate interface (e.g. Fourel et al., 2014; Dielforder et al., 2020). However, the presence of in-plane extension due to slab pull as well as slab weakening due to ongoing dehydration reactions may make such a scenario possible. In conclusion, it is currently not clear which combination of constituent stresses controls the intraslab stress field of Northern Chile, and whether the current temporal snapshot of intraslab stresses is stable over many seismic cycles.

6. The Mantle Wedge

6.1. Observations

The mantle wedge beneath Northern Chile appears to be aseismic. In those cross sections where the continental Moho has been drawn all the way to the slab (at 20 and 22°S; see Figure 14), only few small earthquakes in the IPOC catalog locate in the mantle wedge, but these are situated right above the strong intraslab seismicity cluster and likely represent mislocated events that have received too small hypocentral depths. No distinct clusters or mantle wedge events updip of the intermediate-depth cluster are obtained. Thus, the overwhelming majority of available information about the Northern Chile mantle wedge comes from tomography studies that utilize earthquakes from the underlying slab.

Beneath the Western Cordillera, the mantle wedge can be recognized as a region of clearly elevated seismic attenuation (Q_p ∼100; Haberland and Rietbrock, 2001; Schurr et al., 2003, 2006) and moderate seismic velocities (v_p between 7.7 and 8.3 km/s; e.g. Koulakov et al., 2006; Schurr et al., 2006; Gao et al., 2021), which stands in clear contrast to the underlying slab that is faster and has much lower attenuation. The high-attenuation anomaly of the mantle wedge is continuous into the continental crust and thus connects the region directly above the earthquake clusters in the slab with areas of recent volcanism (e.g. Schurr et al., 2003). The mantle wedge shows elevated v_p/v_s ratio values, most clearly so directly above the slab at depths >70 km (v_p/v_s >1.8; Graeber and Asch, 1999; Schurr et al., 2006; Comte et al., 2016), right above the highly seismogenic regions in the slab. This is also where the highest attenuation values are found (Q_p <100; Schurr et al., 2003). The high-attenuation anomaly of the mantle wedge is most pronounced between 22 and 23°S, and has lower amplitudes further north (Haberland and Rietbrock, 2001). It is displaced eastwards around 24°S, where the Salar de Atacama Block shows extremely low attenuation (Q_p >1000) down to the slab surface (Schurr and Rietbrock, 2004), and decreases in strength southwards from there (Gao et al., 2021). The along-strike variation of v_p/v_s is less clear; while Gao et al. (2021) see a stronger low-v_s anomaly south of 21°S and an "anomaly gap" between 19.8 and 21°S, Comte et al. (2016) retrieved a stronger high-v_p/v_s anomaly north of 21°S. Electric conductivity distributions determined from magnetotelluric experiments (Araya Vargas et al., 2019) appear to be more consistent with the former result.

At 21°S, low values of v_p and high v_p/v_s directly above the slab (Koulakov et al., 2006; Heit et al., 2008) correlate with the Nazca Reflector, a region of exceptionally strong reflectivity found in active seismic experiments (ANCORP_working_group, 1999; Oncken et al., 2003; Yoon et al., 2009; Storch et al., 2016). High attenuation and increased v_p/v_s connect this reflector to the Quebrada Blanca Bright Spot in the shallow crust (e.g. Bloch et al., 2014, see also Section 6). When visualizing the mantle wedge attenuation anomaly together with the slab surface and continental Moho, it is evident that the outermost region of the mantle wedge features high attenuation values, indicative of decreased temperatures and a so-called "cold nose" (e.g. Abers et al., 2017; Sippl et al., 2019). Anisotropy studies show mostly trench-normal fast directions above the mantle wedge, but conclude that the main source of these splitting times should be below the slab (Reiss et al., 2018; Huang et al., 2019).

6.2. Processes

The absence of seismicity inside the Northern Chile mantle wedge stands in contrast to the Colombia and Hellenic subduction zones, where seismicity clusters located inside the mantle wedge have been identified (Chang et al., 2017; Halpaap et al., 2019). In these regions, mantle wedge seismicity has been interpreted to track rising fluids that have been released from the slab, possibly having broken through the plate interface seal (Halpaap et al., 2019). While no mantle wedge seismicity as a direct sign of fluid ascent is observed in Northern Chile, images from attenuation and traveltime tomography imply significant hydration of the mantle wedge further east, below the magmatic arc (e.g. Gao et al., 2021; Schurr et al., 2006). Fluid ascent there apparently occurs aseismically, which may be a consequence of the thermal structure of the mantle wedge. The outer part of the mantle wedge could, however, receive hydration from the deepest part of the plate interface; upper plate seismicity above the deep part of the plate interface (Section 7) could indicate fluid ascent into the continental crust from the deeper part of the plate interface (also seen south of Mejillones Peninsula by Nippress and Rietbrock, 2007). Especially in regions where low permeability above the interface may hinder fluid ascent into the upper plate, this should effect fluid migration in downdip direction, into the outer "cold nose" of the mantle wedge.

According to larger-scale continental Moho maps (Figure 21; Tassara and Echaurren, 2012; Assumpção et al., 2013) as well as geometries retrieved from receiver function profiles (Yuan et al., 2000; Sodoudi et al., 2011; Wölbern et al., 2009), the continental crust thins west of the arc, which leads to a relatively narrow geometry of the outermost mantle wedge. Seismic attenuation in this outermost mantle wedge is quite low (Schurr et al., 2006), in stark contrast to the part of the mantle wedge below the arc. Similar observations have been made in other subduction zones (e.g. Stachnik et al., 2004), and interpreted as the formation of a "cold nose", an outermost part of the mantle wedge that is not part of the corner flow regime and thus cools over time, acquiring a mineral composition and rheology distinct from its convecting part (Abers et al., 2006; Syracuse et al., 2010). While this outer part of the mantle wedge is strongly hydrated and thus serpentinized in young and warm subduction zones like Cascadia (e.g. Bostock et al., 2002), it may be comparatively dry in most other subduction zones (Abers et al., 2017). The seismic evidence from Northern Chile summarized above appears to be consistent with an intermediate serpentinization degree that is lower than in Cascadia. While the velocity contrast between continental lower crust and mantle wedge, which is imaged with receiver functions, grows substantially less distinct towards the slab (Yuan et al., 2000; Wölbern et al., 2009; Sodoudi et al., 2011), no inverted Moho signalling strong serpentinization like in Cascadia (Bostock et al., 2002) is imaged. The Salar de Atacama Block in the south of the study area appears to displace the outermost mantle wedge eastward and likely has a strong effect on its geometry (Schurr and Rietbrock, 2004; Ślęzak et al., 2021), so that a substantially widened "cold nose" may exist in its vicinity.

Lastly, Soto et al. (2019) observed a population of deep aftershocks to the 2014 Iquique earthquake that occurred along the plate interface at a depth beyond the main shock rupture (Section 4.4.2), and that was separated from the remainder of the aftershock sequence by a largely aseismic depth level in-between. Similar observations for the 2010 Maule earthquake (Lange et al., 2012; Rietbrock et al., 2012) were interpreted as indicative of plate interface serpentinization, with an along-dip change in the dominant serpentine mineral due to temperature from lizardite/chrysotile (velocity strengthening, thus aseismic) to antigorite (Wang et al., 2020). While the population of deep aftershock seismicity resides below the outermost mantle wedge in Central Chile, a comparison to continental Moho geometries places it where continental crust still overlies the plate interface in Northern Chile (Soto et al., 2019). Liberated fluids from this region may thus rise into the upper plate, and not into the mantle wedge.

7. The upper plate

7.1. Observations

The South American Plate in the latitude range 18-25°S features substantially thickened crust beneath and east of the Western Cordillera, where receiver function evidence shows crustal thicknesses of ∼60-70 km (Figure 21 Yuan et al., 2000, 2002). Most available cross sections (Yuan et al., 2000; Wölbern et al., 2009; Sodoudi et al., 2011) show a shallowing of the continental Moho beneath the Longitudinal Valley and Coastal Cordillera, where crustal thicknesses of 50-55 km have been retrieved (see Figures 14 and 21). A similar trend is seen in the seismic velocity images of Gao et al. (2021). The contact point between continental Moho and the surface of the downgoing plate is not well resolved by receiver functions, possibly due to serpentinization of the outermost mantle wedge corner. The images of Sodoudi et al. (2011) suggest a depth of 55 km for this contact point at a latitude of 20°S, while it is situated at somewhat shallower depth (50 km or below) at 22°S. Available large-scale models of crustal thickness (e.g. Tassara and Echaurren, 2012; Assumpção et al., 2013, ; Figure 21), in contrast, show more pronounced thinning of the continental crust towards the coast. Evidence from seismic velocities (Husen et al., 2000) indicate that while the mantle wedge corner should not be shallower than 50 km in large parts of the study area, it may be significantly shallower under the Mejillones Peninsula (Schurr et al., 2012).

Seismicity in the upper plate shows significant variability along strike of the study region (Figure 22). In the north, crustal seismicity is sparse except for the aftermath of the Iquique earthquake, where parts of the foreshock sequence as well as the aftershock series occurred in the upper plate (Schurr et al., 2014; Petersen et al., 2021; Soto et al., 2019). Otherwise, background levels of upper plate seismicity are low in the north (e.g. Comte et al., 1999), but the IPOC catalog shows a few shallow clusters that are not related to any obvious mining activity north of 20°S (Figure 23). Seismicity levels beneath the onshore part of the upper plate increase southwards from about 20°S onwards (e.g. Bloch et al., 2014; Sippl et al., 2018; Herrera et al., 2021), and reach a distinct maximum around 21.6°S (Figure 22), where a wedge of background microseismicity in the entire continental crust, extending all the way to the plate interface, is imaged (Figures 14 and 22; Sippl et al., 2018). While seismicity appears to be distributed throughout the crustal volume here, a roughly E-W striking and steeply N-dipping structure of increased seismicity concentration is seen around 21.5°S at depths of 20-50 km. Further east, towards the Western Cordillera, earthquake hypocenters become shallower, possibly following isotherms (Bloch et al., 2014; Sippl et al., 2018; Herrera et al., 2023a). South of about 21.7°S, there is only very sparse upper plate background seismicity of tectonic origin (Figure 22; see also Husen et al., 1999); all retrieved shallow earthquake clusters can be attributed to mining-related activity (Figure 5). To the southeast of where the IPOC catalog has coverage, Graeber and Asch (1999) noted some deep crustal earthquakes (hypocentral depths of up to 40 km) beneath the Salar de Atacama. Several studies of aftershock sequences of major plate interface earthquakes in the study area (Soto et al., 2019; Fuenzalida et al., 2013; Pasten-Araya et al., 2021, for the 2014 Iquique, 2007 Tocopilla and 1995 Antofagasta earthquakes, respectively) have noted that splay faults through the offshore crustal wedge, usually separating Inner and Outer Wedge, get activated in the aftermath of large plate interface events and retain a signature of elevated v_p/v_s ratio in the interseismic period (Pasten-Araya et al., 2021).

Earthquake focal mechanisms in the Northern Chile upper plate show a systematic variation with longitude (Figure 22b,c). Most of the offshore upper plate events have P-axis orientations around E-W, whereas events under the Coastal Cordillera and Longitudinal Valley rather homogeneously show N-S oriented P-axes, either as strike-slip events with potential rupture planes oriented NW-SE and NE-SW, or as thrust events with E-W trending rupture planes. The observable onshore stress field in the forearc is thus margin-parallel compression (Herrera et al., 2021). Towards the Western Cordillera, P-axes again rotate to an E-W orientation, showing compression (sub)parallel to the plate convergence direction (Salazar et al., 2017; Herrera et al., 2021). Only one study has published stress drop estimates for upper plate events in Northern Chile to date, and the values retrieved in Herrera et al. (2023a) for the 2008 Pica earthquake (see below) and its larger aftershocks are very high (40-100 MPa; 255 MPa for the main shock). However, ongoing studies that analyze larger amounts of upper plate events obtain much lower values, which are lower than intraslab events (∼10 MPa; *G.M. Bocchini, pers. comm., 2022*) or even comparable to interplate events (2-4 MPa; *J. Folesky, pers. comm., 2022*). B-values of upper plate seismicity were found to be quite high (b>1; Hainzl et al., 2019), but it is unclear to what degree this result may have been biased by the inclusion of mining-related events. A previous study (Legrand et al., 2012) found values <1, but likely analyzed different events situated further east than most of the upper plate seismicity we retrieved here.

While most of the upper plate seismicity in Northern Chile throughout the last 15 years resembles constant background activity (Figure 22e), some notable event sequences have been registered. To the north of 20°S, several clusters of very shallow upper plate events have been identified (Figure 23). While located in immediate vicinity of each other, they show clear differences in the timing of their activity as well as in their focal mechanisms. The westernmost of these clusters (marked red in Figure 23a) was constantly active throughout the observation time of the IPOC deployment. The location and dominant focal mechanism type (strike-slip events with one plane oriented SSW-NNE; E-W to ENE-WSW oriented P-axes) of events in this cluster are consistent with the 2001 M_w 6.3 Aroma earthquake (Legrand et al., 2007). The remainder of clusters is located somewhat further east, and only showed short bursts of activity in the years 2007 (blue), 2008 (pink, orange and grey), 2009/2010 (yellow), 2011 (green) and 2014 (light blue). While the available focal mechanisms (from Herrera et al., 2021) show some scatter, it is still evident that there are two groups of dominant mechanisms between clusters. While all clusters show predominantly (but not exclusively) strike-slip mechanisms, the red and light blue cluster are dominated by events with E-W oriented P-axes, whereas the clusters east of this (blue, orange, pink, grey) show P-axes largely oriented N-S.
South of 20°S, background seismicity levels increase significantly, and events are largely situated deeper in the continental crust, all the way down to the plate interface (Figure 22). In the last 15 years, two larger events occurred within this "cloud" of background seismicity, each of them creating its own aftershock sequence. The 2008 Pica earthquake (M_w 5.7; green beachball in Figure 24) occurred at a depth of 33 km

and featured a strike-slip mechanism with N-S trending P-axis, thus corresponding well to the regional stress field (Figure 22). The locations and mechanisms of the aftershock sequence indicate that the NW-striking plane was likely the rupture plane (Herrera et al., 2023a). The 2020 Rio Loa earthquake (M_w 6.2; Figure 24) featured a very similar focal mechanism (Tassara et al., 2022) and occurred at a depth of ∼45 km close to the southern termination of the pervasive crustal activity (Figure 22). González et al. (2021) linked this earthquake to the deep continuation of the E-W striking Cerro Aguirre fault zone, whose surface expression is located just south of Rio Loa.

A wide range of seismic tomography studies has shown that the Northern Chilean forearc crust generally features low attenuation ($Q_p \geq 1000$), homogeneously fast P- and S-wavespeeds as well as moderate v_p/v_s around 1.72 (e.g. Husen et al., 2000; Haberland and Rietbrock, 2001; Schurr et al., 2003, 2006; Koulakov et al., 2006; Ward et al., 2013; Gao et al., 2021). v_p/v_s is significantly decreased directly above the plate interface (Husen et al., 2000; Comte et al., 2016), and shallow crustal seismic velocities appear to be subtly higher under the Coastal Cordillera compared to the Longitudinal Valley (Masson et al., 2000). Towards the Western Cordillera and the magmatic arc, v_p and v_s decrease substantially (v_s ∼3.25 instead of 3.6-4 km/s at 15-20 km depth; see Ward et al., 2013; Gao et al., 2021), while v_p/v_s increases to values in excess of 1.8 (Schurr et al., 2006). Attenuation beneath the magmatic arc is substantially elevated, with Q_p ∼100-150 (Schurr et al., 2003; Haberland and Rietbrock, 2001).

There are a number of along-strike variations and specific anomalies that modify this overall picture. The low-v_s (and thus high v_p/v_s) anomaly beneath the magmatic arc appears to be interrupted or at least strongly reduced in amplitude at latitudes of about 20-21°S (where the Pica Volcanic Gap is located) as well as around 24°S (Ward et al., 2013; Gao et al., 2021), whereas the lowest S-wavespeeds are detected under the arc between 21.5 and 23°S (Gao et al., 2021). The results of Comte et al. (2016) show a very different picture of a stronger high-v_p/v_s anomaly north of 21°S than south of this latitude, which may be an artifact due to the highly unbalanced event distribution used in this study. At around 24°S, the crust below the Salar de Atacama basin shows high seismic wavespeeds and very low attenuation (Q_p ∼2000) all the way to the continental Moho, which displaces the low-velocity, high-attenuation and high-v_p/v_s anomaly beneath the Western Cordillera to the east (Schurr and Rietbrock, 2004; Schurr et al., 2006; Gao et al., 2021). At 21°S, a strong low-v_p, low-v_s and high-v_p/v_s-anomaly is imaged in the upper and middle crust just east of 69°W (Heit et al., 2008; Koulakov et al., 2006), where an area of significantly increased reflectivity has been imaged with active seismic methods (the Quebrada Blanca Bright Spot; see ANCORP_working_group, 1999; Oncken et al., 2003; Yoon et al., 2009; Storch et al., 2016). To the south, regions of decreased v_p and elevated v_p/v_s were shown in the upper plate crust directly above the plate interface around the Mejillones Peninsula (Husen et al., 2000; Pasten-Araya et al., 2018, 2021).

Anisotropy observations from S-wave splitting using local intraslab earthquakes show fast directions mainly oriented in trench-parallel directions (Reiss et al., 2018) in the onshore part of the upper plate crust. In contrast, fast directions from an anisotropic tomography study using local earthquakes shows a pattern of fast directions that is radially converging to (or diverging from) the approximate epicenter of the 2014 Iquique earthquake (Huang et al., 2019). Since this pattern is located mostly offshore, the last two observations do not stand in direct contrast to each other.

7.2. Implications and processes

7.2.1. Link between seismicity and active geological structures in the forearc

In the geological record of the Northern Chile forearc, the most prominent structure is the Atacama Fault System (AFS) west of the Western Cordillera, which is a Mesozoic left-lateral strike-slip system (e.g. Scheuber and Andriessen, 1990; Cembrano et al., 2005). Geologically recent motion along the AFS appears to have accommodated mainly E-W extension (Delouis et al., 1998; Loveless et al., 2010), which has led to the assumption that the Northern Chile forearc is currently E-W extensive (e.g. Delouis et al., 1998; Metcalf and Kapp, 2015). Whether the current large-scale kinematics of the AFS are indeed extensional is, however, far from established, and it has been suggested that some fault systems in the region may reverse their fault slip directions through different stages of the seismic cycle (Shirzaei et al., 2012). Microseismicity along the AFS or along similarly oriented structures is absent in the IPOC catalog, which is significant as these features have been inferred to have produced the largest crustal paleoearthquakes in the region based on geomorphological analyses (e.g. González et al., 2006; Allmendinger and González, 2010; Ewiak et al., 2015). More focused short-term deployments close to the trace of the AFS (e.g. Comte et al., 1994) also failed to identify any crustal events there. Moreover, we observe a complete absence of normal faulting crustal events in the published focal mechanism solutions (Figure 22). Only Metcalf and Kapp (2015) reported a few crustal normal-faulting events in the 1990s, which featured N-S striking rupture planes. As these events were taken from global catalogs, we do not know how reliable their depth and thus their classification as upper plate events is.

The vast majority of current microseismicity in the Northern Chile upper plate have strike-slip or reverse mechanisms, and their P-axes trend roughly north-south under the Coastal Cordillera, then switch to a more E-W orientation towards the Western Cordillera (Figure 22; Herrera et al., 2021). At least the former observation is surprising, since geological studies have claimed that the Northern Chile forearc is E-W extensive, whereas geodetic evidence (e.g. Li et al., 2015) appears to indicate a prevalence of E-W compression throughout the forearc. Globally, most forearcs are either under margin-perpendicular compression or extension, and can shift from one to the other in the wake of a large earthquake (e.g. after the 2010 Maule earthquake in Central Chile; Farías et al., 2011). The observed margin-parallel compression in Northern

Chile may be related to the convex shape of the subduction zone (McCaffrey, 1992, 1996), which describes a sharp turn towards the west just north of the study region (the Arica Bend). Thus, the symmetry plane through the entire Andean orogen would run through the region we investigate in a SSW-NNE direction (Gephart, 1994). A number of E-W striking compressional surface structures have been described in the Northern Chile forearc (Allmendinger et al., 2005; Allmendinger and González, 2010), among them the Cerro Aguirre Fault System to the south of the Rio Loa (González et al., 2021). These may well be the surface expressions of faults that accommodate the observed N-S compression.

7.2.2. Fluid-driven crustal seismicity?

The vast majority of the observed upper plate seismicity, however, does not appear to occur along discrete planes reminiscent of faults, but forms a diffuse cloud at depths below about 25 km in a tightly defined latitudinal range (Figures 14 and 22). Seismicity is clearly limited by the thermal structure of the upper plate, occurring where the presence of the underlying slab effects cold temperatures ($<$300-350°C) throughout the continental crust (see Figure 19; Bloch et al., 2014; Sippl et al., 2018; Herrera et al., 2023a). Seismicity density is highest directly above the plate interface and decreases upwards, so that the shallow crust (uppermost 10-15 km) is largely aseismic (see e.g. Figure 7, profile at 21.5°S). This could imply that fluid ascent from the plate interface into the upper plate is responsible for the cloud of crustal seismicity in the center of the study region (as suggested by Bloch et al., 2014). Observations of crustal seismicity south of Mejillones Peninsula after the 1995 Antofagasta earthquake (Nippress and Rietbrock, 2007) were likewise interpreted as due to fluid ascent, possibly facilitated by the breaking of a permeability barrier above the plate interface due to the main shock rupture (Husen and Kissling, 2001). Such a mechanism gives a natural explanation for the lack of clear structures outlined by the seismicity, and as hydration would occur from below, the upward decrease of seismicity rate could be a consequence of less fluid reaching regions further from the plate interface. The earthquake sequence of the 2020 Rio Loa earthquake, shown in Figure 24 and described in more detail in Section 7.1 and in published studies (González et al., 2021; Tassara et al., 2022), may illustrate these processes. The magnitude 6.2 main shock originated in immediate vicinity of the plate interface, but its focal mechanism as well as the plane outlined by the aftershock locations clearly show that it occurred along a steeply dipping structure that penetrates from the plate interface into the upper plate. This earthquake sequence may thus have occurred through hydrofracture due to infiltration of water from below (e.g. Miller, 2013). At least in some cases, large non-double couple contributions ($\geq$15-20%) to the moment tensor were observed for earthquakes with such an origin (e.g. Miller et al., 1998; Vavryčuk and Hrubcová, 2017; Wang et al., 2018), which were not observed here (Tassara et al., 2022). Alternatively, the geometry of background upper plate seismicity could also be prescribed by the forearc's stress distribution, which should be prescribed by processes on the megathrust (e.g. Dielforder et al., 2023).

Pervasive excess hydration of one forearc segment compared to neighboring regions should create a signature of increased v_p/v_s ratio and high attenuation there. Published studies (e.g. Comte et al., 2016; Gao et al., 2021) do not show a clear difference in crustal velocity or attenuation structure between the latitudinal extent of the crustal seismicity (∼20-21.6°S) and the regions to the north and south of this segment. Previous studies, which mostly focussed on active and passive seismic transects collected along 21°S, have inferred strong dehydration from the downgoing slab at this latitude as visible in increased v_p/v_s and strong reflectivity at slab depths (the "Nazca reflector", see e.g. ANCORP_working_group, 1999; Oncken et al., 2003), but inferred a connection of the liberated fluids to the "Quebrada Blanca Bright Spot", a region of significantly increased reflectivity and v_p/v_s in the shallow and deeper crust further east, in close proximity to the Western Cordillera (e.g. Koulakov et al., 2006). There, no anomalous concentration of potentially fluid-related earthquakes has been observed, although strong mining activity in the area (see e.g. Figure 14, profile at 21°S) may obscure some such events. We think that while the strongest slab dehydration clearly occurs beneath the arc (see Section 5), where it creates a clear signature in tomographic images of the mantle wedge as well as in the overlying upper plate crust, upper plate seismicity in the forearc may be driven by the comparatively less intense dehydration of the slab at shallower depths (40-80 km). The wedge-shaped cloud of seismicity we observe is situated where the slab shows a clear DSZ (Figure 7), which hints at stronger dehydration than elsewhere along-strike (see also Section 8.1). Moreover, temperatures are low throughout the upper plate crust here (see isotherms in Figure 19) due to thermal shielding by the underlying slab, which enables brittle rock failure down to the plate interface. This stands in contrast to the sub-arc region further east, where excessive hydration has been inferred, but temperatures likely reach 300-350°C at depths as shallow as 10-15 km, so that brittle failure in the deeper parts of the upper plate, where fluid ascent should occur, is prevented.

8. Discussion

8.1. Spatial connections between seismicity populations

Figure 25 shows event density plots of different seismicity populations, which illuminate event concentrations better than the map view point plot in Figure 6. Looking only at intraslab seismicity from the intermediate-depth cluster, the density plot shows the excess activity in the rupture area of the 2005 Tarapacá earthquake, most of which occurred in the earlier part of the catalog (see Figure 17). Elsewhere, the highest event densities in the slab are found between ∼20.7 and 21.7°S, where three clusters of high event density are separated by completely aseismic gaps. Along those gaps, lateral offsets in the longitudinal onset and termination of seismicity as well as the depth range are observed (Figure 25; Sippl et al., 2018). When only visualizing seismicity deep within the slab, only two clusters separated by an aseismic gap are imaged. When looking at the lower plane of the DSZ (population P3), the map view density plot shows a peculiar distribution with three linear features that roughly strike in downdip direction, as well as an along-margin streak that is situated just beneath the coastline (Figure 25; upper right panel). Elsewhere, the lower plane of the DSZ is largely absent. Seismicity in the upper plate, lastly, is densest between about 20.7 and 21.6°S, where it mostly occurs at large depths, closer to the plate interface than to the surface (Figures 22 and 25). The clusters to the NE are shallow (see Figure 23), whereas the upper plate seismicity related to the 2014 Iquique earthquake in the northern part of the study area is much more diffuse.

When plotted together, the different distributions show a number of interesting spatial connections. The downdip oriented linear trends of active features in the lower DSZ plane line up with the event clusters at intermediate depth further downdip, and the gaps separating them are likewise continuous in downdip direction (Figure 25, lower panel). The concentration of deep upper plate seismicity around 20.7-21.6°S, in turn, is located vertically above where seismicity in the lower plane of the DSZ is most vigorous, although it does not follow the coast-parallel streak of P3 seismicity to the south. Taken together, these observations can be interpreted as evidence for increased fluid production and ascent along sharp and geometrically complex features in the downgoing plate, which may then lead to increased fluid ascent into the upper plate. We further observe that the position of the locking low on the plate interface that separates the Camarones and Loa segments (Figure 8) and coincides with the southern termination of the Iquique earthquake sequence ruptures is likewise located around 21°S. As plate interface locking has been shown to be anti-correlated with pore fluid pressure on the megathrust (Moreno et al., 2014), enhanced fluid processes in this latitude range could be an explanation for the observed potential seismic barrier. It is widely assumed that the hydration of the downgoing plate is enhanced along seafloor features such as fracture zones or ridges (e.g. Kopp et al., 2004; Contreras-Reyes et al., 2008), because the more strongly fractured anomalous oceanic crust and uppermost mantle lithosphere around such features offers more and deeper extending pathways for the infiltration of water. Since intermediate-depth earthquakes are a consequence of slab dehydration, their occurrence and rate should directly depend on the degree of hydration in the downgoing plate, so that one would expect high seismicity rates where features with excess hydration are subducted. Increased seismicity rates along the prolongations of currently subducted features have previously been reported (Kirby et al., 1996; Baillard et al., 2018), but these studies had significantly lower resolution, so that possible detailed signatures of subducted oceanic features in the seismicity geometries were not obtained.

We think that the subduction of an unusual piece of oceanic lithosphere is the cause of the prominent along-strike changes in seismicity that we observe. This subducted feature does likely not correspond to the Iquique Ridge, which is situated further north and has a significantly different strike direction (Figure 1), but appears to be discontinuous to today's seafloor patterns. Seismicity observations show that the inferred subducted feature has much higher activity rates in the deeper parts of the slab, i.e. at depths of more than $\sim$15-17 km beneath the slab surface (Figure 25), hinting at elevated hydration of the slab to deep depths. The observation that seismicity in the deep upper plate crust is confined to the same along-strike extent as the suspected subducted feature is a further indicator of enhanced fluid processes along this narrow region.

As discussed in Section 7.2, the diffuse upper plate seismicity between 20.7 and 21.6°S could well be related to fluid influx from below, and Figure 25 shows that its distribution lines up rather well with underlying clusters of lower-plane (P3) seismicity. That the linear streak of lower plane events that extends further south along the coastline is not accompanied by more upper plate seismicity could be a consequence of a lateral change in the permeability of the plate interface. The material directly above the plate interface is often imagined to form an impermeable seal, which prevents fluid influx into the upper plate unless it is broken (e.g. Husen and Kissling, 2001). Ongoing processes south of 21.6°S (see Section 4) may well have led to an intact seal in this region, whereas it could be less intact where we observe widespread lower crustal seismicity.

It is also worth noting that although a large number of ridges and fracture zones are currently being subducted along the Chilean margin (e.g. Contreras-Reyes and Carrizo, 2011), the seismicity features observed around 21°S both at depth and in the upper plate appear to be unique along the entire margin. Although the rate of intraslab seismicity varies along strike, similar intraslab seismicity rates or diffuse clouds of deep crustal seismicity have not been observed elsewhere (e.g. Barrientos, 2018).

8.2. Comparison latest interseismic to postseismic phase of Iquique earthquake

With the Iquique earthquake sequence (Section 4.4.2) situated around the middle of our 15 years of seismicity catalog, we can investigate the impact of a major megathrust earthquake onto the different parts of the forearc by comparing the seismicity before and after the Iquique sequence. In Figure 26, event rates for plate interface seismicity throughout the 15 years (subfigure a) as well as around the Iquique earthquake sequence (subfigure b) are shown. It can be seen that event rates are not drastically different before and after the Iquique sequence, and that event rates similar to before the sequence are reached again approximately 1.5 years after the Iquique main shock. We thus subdivide the catalog into three time slices: before the Iquique sequence (until January 1st, 2014), the Iquique sequence itself (years 2014 and 2015) as well as after the Iquique sequence (after January 1st, 2016). These phases may correspond to the latest interseismic, postseismic and earliest interseismic stage of the seismic cycle along this part of the Northern Chile subduction zone. Figure 27 shows the distributions of plate interface, upper plate and intraslab seismicity for the region around the Iquique earthquake in these three phases.

Plate interface seismicity before the Iquique sequence is mainly located in the deeper parts of the megathrust. A half-circle of seismicity, more clearly visible on the northern than on the southern side, surrounds the later main shock slip. This feature, discussed in detail in Schurr et al. (2020), likely reflects stress accumulation at the downdip edge of a locked asperity. Most of the Iquique earthquake sequence seismicity, including foreshocks (e.g. Cesca et al., 2016; Kato et al., 2016) as well as aftershocks (e.g. Soto et al., 2019; Petersen et al., 2021), occurred in the shallower part of the plate interface, updip of the main shock rupture. While parts of the deeper interface were also activated, the region of main shock slip itself shows low seismicity levels. The post-Iquique distribution of plate interface seismicity is markedly different from the time interval before the main shock. The half-"Mogi doughnut" around the main shock slip has disappeared, indicating that the asperity that ruptured during the Iquique earthquake has released a large part of the stress that had been accumulated before. Although it may have transitioned back to a locked state again, stress levels that could trigger microseismicity at its downdip edge have not been reached again yet. Moreover, the region updip of the main shock continues to be more active than before 2014, which could indicate that postseismic processes continue to be active in this time period, although overall seismicity rates on the plate interface have returned to interseismic levels.

Seismicity in the upper plate shows less dramatic changes through time. During the Iquique sequence, there is increased upper plate seismicity offshore, corresponding to the observation that parts of the foreshock and aftershock sequences occurred above the plate interface (e.g. Ruiz et al., 2019; Petersen et al., 2021). Some of the shallow clusters of seismicity around 69°W were only active in the earlier part of the analyzed time interval, but this activity is unlikely to be related to processes along the megathrust. Lastly, there does not appear to be any major change in the geometry and distribution of intraslab seismicity over time. The only clearly observable trend is the slow decay of activity around 20°S, where the Tarapacá earthquake had occurred in 2005 (see Figures 17 and 25).

8.3. Possible links between intraslab and plate interface processes

It is a matter of debate how and to what degree processes inside the downgoing slab and on the plate interface are coupled, and how these different regions interact. A number of large megathrust earthquakes have been preceded by large intermediate-depth earthquakes in the same region years to few decades before, just like the 2005 Tarapacá earthquake preceded the 2014 Iquique earthquake by ∼9 years. Such observations could be explained as the initiation of (precursory) slip on the plate interface through processes in the slab (e.g. Dmowska et al., 1988), which eventually leads to the rupture of the megathrust further updip. If and how such direct interaction occurs is not well known to date.

Bouchon et al. (2016) and Jara et al. (2017) have proposed direct interactions between intraslab and plate interface events in Northern Chile around the time of the 2014 Iquique earthquake. While the former study presented evidence for correlated moment release between slab and plate interface during the precursory phase of the Iquique earthquake, the latter study analyzed event rates over a longer time period, and concluded that the 2005 Tarapacá earthquake increased event rates of both intraslab and interface events leading to the 2014 Iquique event, which effected relative quiescence across both domains. As the aforementioned studies used global catalogs and thus operated with rather low event numbers and high location uncertainties, we performed a similar analysis with our much more complete catalog.

Figure 28a shows plots of moment release and seismicity rates for the entire time period, whereas Figure

28b presents a zoom-in onto the precursory phase of the Iquique earthquake. Since our catalog does not extend back to the 2005 Tarapacá earthquake, we can not evaluate what changes to the different seismicity rates this earthquake may have had. We clearly do not see a sudden decrease in intraslab seismicity after the Iquique earthquake, as stated in Jara et al. (2017). Both moment release and event rates show a slight decrease between earlier times (roughly 2007-2011) and later times, likely due to the previously mentioned long-term decay of seismicity in the years after the 2005 Tarapacá earthquake. The occurrence of the Iquique earthquake in 2014 does not appear to alter intraslab seismicity rates, moment release or seismicity distribution (see Figure 27) in a significant way. Analyzing ISC data as well as the catalog of Sippl et al. (2018), Wimpenny et al. (2022) likewise concluded that there is no robust evidence for changes in event rates of intermediate-depth earthquakes coinciding or caused by the Iquique earthquake.

Using our more complete catalog to focus on the precursory phase of the Iquique earthquake, we re-create the plot of Bouchon et al. (2016) (Figure 28b, left) while also analyzing event rates (right subplot). Event rates in the slab do not show significant variations throughout the plotted time interval. When looking at moment release, we see that while some large plate interface events indeed occurred in close temporal proximity to larger intraslab events, the correlation is much less straightforward than what is shown in Bouchon et al. (2016). This is likely due to the use of very low event numbers in this paper ($\sim$8 plate interface events in total), combined with an arbitrary choice of cut-off magnitudes (M>4 for plate interface but not intraslab events). While the occurrence of a large M6 intermediate-depth event just downdip of the later megathrust rupture on the day before the Iquique main shock is indeed intriguing, we do not consider the evidence for the proposed correlated seismicity bursts during the preparatory phase convincing. While we do not rule out possible triggering effects between intraslab and plate interface earthquakes, we think that there is not much compelling evidence for their occurrence in the time preceding the Iquique earthquake.

9. Conclusions

15 years of permanent seismic and geodetic monitoring of the Northern Chile forearc have provided a wealth of data, which have helped to considerably advance our understanding of ongoing processes throughout the different regions of a subduction margin.

The Northern Chile megathrust was the site of two major earthquakes during this 15-year period. Especially the 2014 M_w 8.1 Iquique earthquake, for which dense monitoring networks have been in place during the preparatory phase as well as during and after the main shock, has provided the community with new insights about how large megathrust earthquakes nucleate, and what precursory seismic and aseismic signals they may create. At least the region south of the 2014 Iquique ruptures remains a mature seismic gap, in which another large megathrust earthquake is likely to occur within the next decades. In spite of the large aftershock series of the Iquique and Tocopilla events, the vast majority of seismicity in Northern Chile occurs at intermediate depths (~80-130 km) and is linked to dehydration reactions inside the downgoing oceanic crust and mantle lithosphere. Along-strike variations in seismicity rate as well as geometry appear to be linked to structural features of the downgoing Nazca Plate, and the spatial variability of liberated fluids may condition the occurrence of seismicity in the upper plate as well as the coupling structure of the megathrust.

Thus, the presented seismological observations demonstrate that we can not fully understand any constituent part of the subduction system in isolation, but must strive to better resolve and understand the sometimes complex interaction between the different realms. The large amount of knowledge on Northern Chile that has been acquired over the past 15 years only begins to show us what links between the different parts of the subduction system, megathrust, upper and lower plate as well as mantle wedge, may control or influence our observations.

Acknowledgments

The IPOC initiative would have not been possible without the months of fieldwork by dedicated scientists and technicians. We want to thank in particular G. Asch, who almost single-handedly set up and operated IPOC multi-parameter stations over many years. The Universidad Católica del Norte, Antofagasta, Universidad de Chile, Santiago as well as Centro Sismológico Nacional (CSN) strongly supported these endeavors. Geodetic networks were operated over decades by multiple institutions including French IRD, ENS, Caltech, GFZ, CSN, and Univ. Catolica del Norte, Antofagasta. Comments from two anonymous reviewers as well as the Editor Eduardo Contreras-Reyes helped to improve the manuscript. We further thank Sebastian Hainzl for declustering the earthquake catalog, Carlos Herrera for making a manuscript available to us before publication, as well as all scientists who made datasets available for our use.

C. Sippl has received funding from the European Research Council (ERC) under the European Union's Horizon 2020 research and innovation progreamme (ERC Starting Grant MILESTONE; StG2020-947856). The IPOC catalog is available for download under https://doi.org/10.5880/GFZ.4.1.2023.004, details can be found in the accompanying data publication of Sippl et al. (2023). For the compilation of the catalog, we used data from seismic stations of the IPOC network (CX; GFZ and CNRS-INSU, 2006), complemented by selected stations of networks C1 (Universidad de Chile, 2013), C (no DOI), 8F (Wigger et al., 2016), 5E (Asch et al., 2011), IQ (Cesca et al., 2009) and GE (GEOFON_Data_Centre, 1993). This work was supported by the Ministry of Education, Youth and Sports of the Czech Republic through the e-INFRA CZ (ID:90140).

References

Abers, G.A., van Keken, P., Hacker, B.R., 2017. The cold and relatively dry nature of mantle forearcs in subduction zones. Nature Geoscience 10, 333–337.

Abers, G.A., van Keken, P., Kneller, E.A., Ferris, A., Stachnik, J.C., 2006. The thermal structure of subduction zones constrained by seismic imaging: Implications for slab dehydration and wedge flow. Earth and Planetary Science Letters 241, 387–397.

Aden-Antóniow, F., Satriano, C., Bernard, P., Poiata, N., Aissaoui, E.M., Vilotte, J.P., Frank, W.B., 2020. Statistical Analysis of the Preparatory Phase of the Mw 8.1 Iquique Earthquake, Chile. Journal of Geophysical Research: Solid Earth 125, 1–14.

Allmendinger, R.W., González, G., 2010. Invited review paper: Neogene to Quaternary tectonics of the coastal Cordillera, northern Chile. Tectonophysics 495, 93–110.

Allmendinger, R.W., González, G., Yu, J., Hoke, G., Isacks, B.L., 2005. Trench-parallel shortening in the Northern Chilean Forearc: Tectonic and climatic implications. Bulletin of the Geological Society of America 117, 89–104.

An, C., Sepúlveda, I., Liu, P.L., 2014. Tsunami source and its validation of the 2014 Iquique, Chile, earthquake. Geophysical Research Letters 41, 3988–3994.

ANCORP_working_group, 1999. Seismic reflection image revealing offset of Andean subduction-zone earthquake locations into oceanic mantle. Nature 397, 341–344.

Angermann, D., Klotz, J., Reigber, C., 1999. Space-geodetic estimation of the Nazca-South America Euler vector. Earth and Planetary Science Letters 171, 329–334.

Araya Vargas, J., Meqbel, N.M., Ritter, O., Brasse, H., Weckmann, U., Yáñez, G., Godoy, B., 2019. Fluid Distribution in the Central Andes Subduction Zone Imaged With Magnetotellurics. Journal of Geophysical Research: Solid Earth 124, 4017–4034.

Araya Vargas, J., Sanhueza, J., Yáñez, G., 2021. The Role of Temperature in the Along-Margin Distribution of Volcanism and Seismicity in Subduction Zones: Insights From 3-D Thermomechanical Modeling of the Central Andean Margin. Tectonics 40, e2021TC006879.

Armijo, R., Thiele, R., 1990. Active faulting in northern Chile: ramp stacking and lateral decoupling along a subduction plate boundary? Earth and Planetary Science Letters 98, 40–61.

Asch, G., Schurr, B., Bohm, M., Yuan, X., Haberland, C., Heit, B., Kind, R., Woelbern, I., Bataille, K., Comte, D., Pardo, M., Viramonte, J., Rietbrock, A., Giese, P., 2006. Seismological Studies of the Central and Southern Andes, in: Oncken, O., Chong, G., Franz, G., Giese, P., Götze, H.J., Ramos, V.A., Strecker, M., Wigger, P. (Eds.), The Andes. Springer Berlin Heidelberg, pp. 443–457.

Asch, G., Tilmann, F., Schurr, B., Ryberg, T., 2011. Seismic network 5E: MINAS Project (2011/2013).

Assumpção, M., Feng, M., Tassara, A., Julià, J., 2013. Models of crustal thickness for South America from seismic refraction, receiver functions and surface wave tomography. Tectonophysics 609, 82–96.

Báez, J.C., Leyton, F., Troncoso, C., Del Campo, F., Bevis, M., Vigny, C., Moreno, M., Simons, M., Kendrick, E., Parra, H., Blume, F., 2018. The Chilean GNSS network: Current status and progress toward early warning applications. Seismological Research Letters 89, 1546–1554.

Bai, Y., Cheung, K.F., Yamazaki, Y., Lay, T., Ye, L., 2014. Tsunami surges around the Hawaiian Islands from the 1 April 2014 North Chile Mw 8.1 earthquake. Geophysical Research Letters 41, 8512–8521.

Baillard, C., Crawford, W.C., Ballu, V., Pelletier, B., Garaebiti, E., 2018. Tracking subducted ridges through intermediate-depth seismicity in the Vanuatu subduction zone. Geology 46, 767–770.

Barazangi, M., Isacks, B.L., 1976. Spatial distribution of earthquakes and subduction of the Nazca plate beneath South America. Geology 4, 686–692.

Barrientos, S., 2018. The Seismic Network of Chile. Seismological Research Letters 89, 467–474.

Bassett, D., Watts, A.B., 2015. Gravity anomalies, crustal structure, and seismicity at subduction zones: 1. Seafloor roughness and subducting relief. Geochemistry, Geophysics, Geosystems 16, 1508–1540.

Beck, S.L., Zandt, G., Myers, S.C., Wallace, T.C., Silver, P.G., Drake, L., 1996. Crustal-thickness variations in the central

Andes. Geology 24, 407–410.

Beck, S.L., Zandt, G., Ward, K.M., Scire, A., 2015. Multiple styles and scales of lithospheric foundering beneath the Puna Plateau, central Andes. Geological Society of America Memoir 212, 43–60.

Bedford, J., Moreno, M., Schurr, B., Bartsch, M., Oncken, O., 2015. Investigating the final seismic swarm before the Iquique-Pisagua 2014 M<inf>w</inf> 8.1 by comparison of continuous GPS and seismic foreshock data. Geophysical Research Letters 42, 3820–3828.

Béjar-Pizarro, M., Carrizo, D., Socquet, A., Armijo, R., Barrientos, S., Bondoux, F., Bonvalot, S., Campos, J., Comte, D., De Chabalier, J.B., Charade, O., Delorme, A., Gabalda, G., Galetzka, J., Genrich, J., Nercessian, A., Olcay, M., Ortega, F., Ortega, I., Remy, D., Ruegg, J.C., Simons, M., Valderas, C., Vigny, C., 2010. Asperities and barriers on the seismogenic zone in North Chile: State-of-the-art after the 2007 Mw 7.7 Tocopilla earthquake inferred by GPS and InSAR data. Geophysical Journal International 183, 390–406.

Béjar-Pizarro, M., Socquet, A., Armijo, R., Carrizo, D., Genrich, J., Simons, M., 2013. Andean structural control on interseismic coupling in the North Chile subduction zone. Nature Geoscience 6, 462–467.

Bello-González, J.P., Contreras-Reyes, E., Arriagada, C., 2018. Predicted path for hotspot tracks off South America since Paleocene times: Tectonic implications of ridge-trench collision along the Andean margin. Gondwana Research 64, 216–234.

Bijwaard, H., Spakman, W., Engdahl, E.R., 1998. Closing the gap between regional and global travel time tomography. Journal of Geophysical Research 103, 30055–30078.

Bilek, S.L., Lay, T., 2018. Subduction zone megathrust earthquakes. Geosphere 14, 1468–1500.

Bindi, D., Parolai, S., Gómez Capera, A.A., Locati, M., Kalmetyeva, Z., Mikhailova, N., 2014. Locations and magnitudes of earthquakes in Central Asia from seismic intensity data. Journal of Seismology 18, 1–21.

Bishop, B.T., Beck, S.L., Zandt, G., Wagner, L.S., Long, M.D., Antonijevic, S.K., Kumar, A., Tavera, H., 2017. Causes and consequences of flat-slab subduction in southern Peru. Geosphere 13, 1392–1407.

Bloch, W., John, T., Kummerow, J., Salazar, P., Krüger, O.S., Shapiro, S.A., 2018a. Watching Dehydration: Seismic Indication for Transient Fluid Pathways in the Oceanic Mantle of the Subducting Nazca Slab. Geochemistry, Geophysics, Geosystems 19, 3189–3207.

Bloch, W., Kummerow, J., Salazar, P., Wigger, P., Shapiro, S.A., 2014. High-resolution image of the North Chilean subduction zone: Seismicity, reflectivity and fluids. Geophysical Journal International 197, 1744–1749.

Bloch, W., Schurr, B., Kummerow, J., Salazar, P., Shapiro, S.A., 2018b. From Slab Coupling to Slab Pull: Stress Segmentation in the Subducting Nazca Plate. Geophysical Research Letters 45, 5407–5416.

Bock, G., Schurr, B., Asch, G., 2000. High-resolution image of the oceanic Moho. Geophysical Research Letters 27, 3929–3932.

Bostock, M.G., Hyndman, R.D., Rondenay, S., Peacock, S.M., 2002. An inverted continental moho and serpentinization of the forearc mantle. Nature 417, 536–538.

Bouchon, M., Marsan, D., Durand, V., Campillo, M., Perfettini, H., Madariaga, R., Gardonio, B., 2016. Potential slab deformation and plunge prior to the Tohoku, Iquique and Maule earthquakes. Nature Geoscience 9, 380–383.

Boudin, F., Bernard, P., Meneses, G., Vigny, C., Olcay, M., Tassara, C., Boy, J.P., Aissaoui, E., Métois, M., Satriano, C., Esnoult, M.F., Nercessian, A., Vallée, M., Vilotte, J.P., Brunet, C., 2022. Slow slip events precursory to the 2014 Iquique Earthquake, revisited with long-base tilt and GPS records. Geophysical Journal International 228, 2092–2121.

Bravo, F., Koch, P., Riquelme, S., Fuentes Serrano, M., Campos, J., 2019. Slip Distribution of the 1985 Valparaíso Earthquake Constrained with Seismic and Deformation Data. Seismological Research Letters 9, 1–9.

Brudzinski, M.R., Thurber, C.H., Hacker, B.R., Engdahl, E.R., 2007. Global prevalence of double benioff zones. Science 316, 1472–1474.

Cabrera, L., Ruiz, S., Poli, P., Contreras-Reyes, E., Osses, A., Mancini, R., 2021. Northern Chile intermediate-depth earthquakes controlled by plate hydration. Geophysical Journal International 226, 78–90.

Cahill, T., Isacks, B.L., 1992. Seismicity and shape of the subducted Nazca Plate. Journal of Geophysical Research 97, 17503–17529.

Cai, C., Wiens, D.A., Shen, W., Eimer, M., 2018. Water input into the Mariana subduction zone estimated from ocean-bottom seismic data. Nature 563, 389–392.

Cembrano, J., González, G., Arancibia, G., Ahumada, I., Olivares, V., Herrera, V., 2005. Fault zone development and strain partitioning in an extensional strike-slip duplex: A case study from the Mesozoic Atacama fault system, Northern Chile. Tectonophysics 400, 105–125.

Cesca, S., 2020. Seiscloud, a tool for density-based seismicity clustering and visualization. Journal of Seismology 24, 443–457.

Cesca, S., Grigoli, F., Heimann, S., Dahm, T., Kriegerowski, M., Sobiesiak, M., Tassara, C., Olcay, M., 2016. The Mw 8.1 2014 Iquique, Chile, seismic sequence: A tale of foreshocks and aftershocks. Geophysical Journal International 204, 1766–1780.

Cesca, S., Sobiesiak, M., Tassara, A., Olcay, M., Günther, E., Mikulla, S., Dahm, T., 2009. The Iquique Local Network and PicArray.

Chang, Y., Warren, L.M., Prieto, G.A., 2017. Precise locations for intermediate-depth earthquakes in the Cauca Cluster, Colombia. Bulletin of the Seismological Society of America 107, 2649–2663.

Chlieh, M., De Chabalier, J.B., Ruegg, J.C., Armijo, R., Dmowska, R., Campos, J., Feigl, K.L., 2004. Crustal deformation and fault slip during the seismic cycle in the North Chile subduction zone, from GPS and InSAR observations. Geophysical Journal International 158, 695–711.

Chlieh, M., Perfettini, H., Tavera, H., Avouac, J.P., Remy, D., Nocquet, J.M., Rolandone, F., Bondoux, F., Gabalda, G., Bonvalot, S., 2011. Interseismic coupling and seismic potential along the Central Andes subduction zone. Journal of Geophysical Research: Solid Earth 116, B12405.

Chu, S.X., Beroza, G.C., 2022. Aftershock productivity of intermediate-depth earthquakes in Japan. Geophysical Journal International 230, 448–463.

Comte, D., Carrizo, D., Roecker, S.W., Ortega Culaciati, F., Peyrat, S., 2016. Three-dimensional elastic wave speeds in the northern Chile subduction zone: Variations in hydration in the supraslab mantle. Geophysical Journal International 207, 1080–1105.

Comte, D., Dorbath, L., Pardo, M., Monfret, T., Haessler, H., Rivera, L., Frogneux, M., Glass, B., Meneses, C., 1999. A double-layered seismic zone in Arica, northern Chile. Geophysical Research Letters 26, 1965–1968.

Comte, D., Pardo, M., 1991. Reappraisal of great historical earthquakes in the northern Chile and southern Peru seismic gaps. Natural Hazards 4, 23–44.

Comte, D., Pardo, M., Dorbath, L., Dorbath, C., Haessler, H., Rivera, L., Cisternas, A., Ponce, L., 1994. Determination of seismogenic interplate contact zone and crustal seismicity around Antofagasta, northern Chile using local data. Geophysical Journal International 116, 553–561.

Contreras-Reyes, E., Carrizo, D., 2011. Control of high oceanic features and subduction channel on earthquake ruptures along the Chile-Peru subduction zone. Physics of the Earth and Planetary Interiors 186, 49–58.

Contreras-Reyes, E., Díaz, D., Bello-González, J.P., Slezak, K., Potin, B., Comte, D., Maksymowicz, A., Ruiz, J., Osses, A., Ruiz, S., 2021a. Subduction zone fluids and arc magmas conducted by lithospheric deformed regions beneath the central Andes. Scientific Reports 11, 23078.

Contreras-Reyes, E., Grevemeyer, I., Flueh, E.R., Reichert, C., 2008. Upper lithospheric structure of the subduction zone offshore of southern Arauco peninsula, Chile, at 38S. Journal of Geophysical Research: Solid Earth 113, B07303.

Contreras-Reyes, E., Jara, J., Grevemeyer, I., Ruiz, S., Carrizo, D., 2012. Abrupt change in the dip of the subducting plate beneath north Chile. Nature Geoscience 5, 342–345.

Contreras-Reyes, E., Obando-Orrego, S., Geersen, J., Bello-González, J.P., 2021b. Density structure, flexure, and tectonics of the Iquique Ridge, northern Chile. Journal of South American Earth Sciences 111, 103423.

Coulbourn, W.T., 1981. Tectonics of the Nazca plate and the continental margin of western South America, 18S to 23S. Memoir of the Geological Society of America 154, 587–618.

Craig, T.J., 2019. Accurate Depth Determination for Moderate-Magnitude Earthquakes Using Global Teleseismic Data. Journal of Geophysical Research 124, 1759–1780.

Craig, T.J., Copley, A., Jackson, J., 2014. A reassessment of outer-rise seismicity and its implications for the mechanics of oceanic lithosphere. Geophysical Journal International 197, 63–89.

Delouis, B., Legrand, D., 2007. Mw 7.8 Tarapaca intermediate depth earthquake of 13 June 2005 (northern Chile): Fault plane identification and slip distribution by waveform inversion. Geophysical Research Letters 34, 1–6.

Delouis, B., Pardo, M., Legrand, D., Monfret, T., 2009. The Mw 7.7 Tocopilla earthquake of 14 November 2007 at the Southern edge of the Northern Chile seismic gap: Rupture in the deep part of the coupled plate interface. Bulletin of the Seismological Society of America 99, 87–94.

Delouis, B., Philip, H., Dorbath, L., Cisternas, A., 1998. Recent crustal deformation in the Antofagasta region (northern Chile) and the subduction process. Geophysical Journal International 132, 302–338.

Derode, B., Delouis, B., Campos, J., 2019. Systematic Determination of Focal Mechanisms over a Wide Magnitude Range: Insights from the RealTime FMNEAR Implementation in Chile from 2015 to 2017. Seismological Research Letters 90, 1285–1295.

Di Stefano, R., Aldersons, F., Kissling, E., Baccheschi, P., Chiarabba, C., Giardini, D., 2006. Automatic seismic phase picking and consistent observation error assessment: Application to the Italian seismicity. Geophysical Journal International 165, 121–134.

Diehl, T., Deichmann, N., Kissling, E., Husen, S., 2009. Automatic S-wave picker for local earthquake tomography. Bulletin of the Seismological Society of America 99, 1906–1920.

Dielforder, A., Bocchini, G.M., Kemna, K., Hampel, A., Harrington, R.M., 2023. Megathrust Stress Drop as Trigger of Aftershock Seismicity : Insights From the 2011 Tohoku Earthquake, Japan. Geophysical Research Letters 50, e2022GL101320.

Dielforder, A., Hetzel, R., Oncken, O., 2020. Megathrust shear force controls mountain height at convergent plate margins. Nature 582, 225–229.

Dmowska, R., Rice, J.R., Lovison, L.C., Josell, D., 1988. Stress transfer and seismic phenomena in coupled subduction zones during the earthquake cycle. Journal of Geophysical Research 93, 7869–7884.

Dorbath, C., Gerbault, M., Carlier, G., Guiraud, M., 2008. Double seismic zone of the Nazca plate in northern Chile: High-resolution velocity structure, petrological implications, and thermomechanical modeling. Geochemistry, Geophysics, Geosystems 9.

Dorbath, C., Granet, M., Poupinet, G., Martinez, C., 1993. A teleseismic study of the Altiplano and the Eastern Cordillera in northern Bolivia: new constraints on a lithospheric model. Journal of Geophysical Research 98, 9825–9844.

Duputel, Z., Jiang, J., Jolivet, R., Simons, M., Rivera, L., Ampuero, J.P., Riel, B., Owen, S.E., Moore, A.W., Samsonov, S., Ortega Culaciati, F., Minson, S.E., 2015. The Iquique earthquake sequence of April 2014: Bayesian modeling accounting for prediction uncertainty. Geophysical Research Letters 42, 7949–7957.

Engdahl, E.R., Scholz, C.H., 1977. A double Benioff zone beneath the Central Aleutians: an unbending of the lithosphere. Geophysical Research Letters 4, 473–476.

Ewiak, O., Victor, P., Oncken, O., 2015. Investigating multiple fault rupture at the Salar del Carmen segment of the Atacama Fault System (northern Chile): Fault scarp morphology and knickpoint analysis. Tectonics 34, 187–212.

Faccenda, M., Gerya, T.V., Mancktelow, N.S., Moresi, L., 2012. Fluid flow during slab unbending and dehydration: Implications for intermediate-depth seismicity, slab weakening and deep water recycling. Geochemistry, Geophysics, Geosystems 13, Q01010.

Faccenna, C., Oncken, O., Holt, A.F., Becker, T.W., 2017. Initiation of the Andean orogeny by lower mantle subduction. Earth and Planetary Science Letters 463, 189–201.

Fang, H., van der Hilst, R.D., 2019. Earthquake Depth Phase Extraction With P Wave Autocorrelation Provides Insight Into Mechanisms of Intermediate-Depth Earthquakes. Geophysical Research Letters 46, 14440–14449.

Farías, M., Comte, D., Roecker, S.W., Carrizo, D., Pardo, M., 2011. Crustal extensional faulting triggered by the 2010 Chilean earthquake: The Pichilemu Seismic Sequence. Tectonics 30, TC6010.

Ferrand, T., 2019. Seismicity and mineral destabilizations in the subducting mantle up to 6GPa, 200km depth. Lithos 334-335, 205–230.

Ferrand, T., Hilairet, N., Incel, S., Deldicque, D., Labrousse, L., Gasc, J., Renner, J., Wang, Y., Green, H., Schubnel, A., 2017. Dehydration-driven stress transfer triggers intermediate-depth earthquakes. Nature Communications 8, 1–11.

Florez, M.A., Prieto, G.A., 2019. Controlling Factors of Seismicity and Geometry in Double Seismic Zones. Geophysical Research Letters 46, 4174–4181.

Folesky, J., Kummerow, J., Asch, G., Schurr, B., Sippl, C., Tilmann, F., Shapiro, S.A., 2018a. Estimating Rupture Directions from Local Earthquake Data Using the IPOC Observatory in Northern Chile. Seismological Research Letters 89, 495–502.

Folesky, J., Kummerow, J., Shapiro, S.A., 2018b. Patterns of Rupture Directivity of Subduction Zone Earthquakes in Northern Chile. Journal of Geophysical Research: Solid Earth 123, 10,785–10,796.

Folesky, J., Kummerow, J., Shapiro, S.A., 2021. Stress Drop Variations in the Region of the 2014 M W 8.1 Iquique Earthquake, Northern Chile . Journal of Geophysical Research: Solid Earth 126.

Fourel, L., Goes, S., Morra, G., 2014. The role of elasticity in slab bending. Geochemistry, Geophysics, Geosystems 15, 4507–4525.

Frankel, A., 2022. High-Frequency Rupture Processes of the 2014 Mw 8.2 Iquique and 2015 Mw 8.3 Illapel, Chile, Earthquakes Determined from Strong-Motion Recordings. Bulletin of the Seismological Society of America 112, 1832–1852.

Fuenzalida, A., Schurr, B., Lancieri, M., Sobiesiak, M., Madariaga, R., 2013. High-resolution relocation and mechanism of aftershocks of the 2007 Tocopilla (Chile) earthquake. Geophysical Journal International 194, 1216–1228.

Gao, Y., Tilmann, F., Herwaarden, D., Thrastarson, S., Fichtner, A., Heit, B., Yuan, X., Schurr, B., 2021. Full Waveform Inversion Beneath the Central Andes: Insight Into the Dehydration of the Nazca Slab and Delamination of the BackArc Lithosphere. Journal of Geophysical Research: Solid Earth 126.

Garth, T., Rietbrock, A., 2017. Constraining the hydration of the subducting Nazca plate beneath Northern Chile using subduction zone guided waves. Earth and Planetary Science Letters 474, 237–247.

GEBCO_Compilation_Group, 2020. GEBCO 2020 Grid.

Geersen, J., Ranero, C.R., Barckhausen, U., Reichert, C., 2015. Subducting seamounts control interplate coupling and seismic rupture in the 2014 Iquique earthquake area. Nature Communications 6, 6–11.

Geersen, J., Ranero, C.R., Kopp, H., Behrmann, J.H., Lange, D., Klaucke, I., Barrientos, S., Diaz-Naveas, J., Barckhausen, U., Reichert, C., 2018. Does permanent extensional deformation in lower forearc slopes indicate shallow plate-boundary rupture? Earth and Planetary Science Letters 489, 17–27.

Geersen, J., Sippl, C., Harmon, N., 2022. Impact of bending-related faulting and oceanic-plate topography on slab hydration and intermediate-depth seismicity. Geosphere 18, 562–584.

GEOFON_Data_Centre, 1993. GEOFON Seismic Network.

Gephart, J.W., 1994. Topography and subduction geometry in the central Andes: Clues to the mechanics of a noncollisional orogen. Journal of Geophysical Research 99, 12279–12288.

GFZ, CNRS-INSU, 2006. IPOC Seismic Network: Integrated Plate boundary Observatory Chile - IPOC.

Global_Volcanism_Program, 2013. Volcanoes of the World, v. 4.10.6, Smithsonian Institution.

Gomberg, J., Bodin, P., 2021. The productivity of cascadia aftershock sequences. Bulletin of the Seismological Society of America 111, 1494–1507.

Gómez, J., Schobbenhaus, C., Montes, N., Compilers, 2019. Geological Map of South America 2019; Scale 1:5000000. Commission for the Geological Map of the World (CGMW), Colombian Geological Survey and Geological Survey of Brazil, Paris.

González, F.A., Bello-González, J.P., Contreras-Reyes, E., Tréhu, A.M., Geersen, J., 2023. Shallow structure of the Northern Chilean marine forearc between 19S - 21S using multichannel seismic reflection and refraction data. Journal of South American Earth Sciences 123, 104243.

González, G., Dunai, T., Carrizo, D., Allmendinger, R., 2006. Young displacements on the Atacama Fault System, northern Chile from field observations and cosmogenic 21Ne concentrations. Tectonics 25, 1–15.

González, G., Pasten-Araya, F., Victor, P., González, Y., Valenzuela, J., Shrivastava, M., 2021. The role of interplate locking on the seismic reactivation of upper plate faults on the subduction margin of northern Chile. Scientific Reports 11, 1–12.

González, G., Salazar, P., Loveless, J.P., Allmendinger, R.W., Aron, F., Shrivastava, M., 2015. Upper plate reverse fault reactivation and the unclamping of the megathrust during the 2014 northern Chile earthquake sequence. Geology 43, 671–674.

Graeber, F., Asch, G., 1999. Three-dimensional models of P wave velocity and P -to- S velocity ratio in the southern central Andes by simultaneous inversion of local earthquake data. Journal of Geophysical Research 104, 20237–20256.

Greve, F., 1964. Historia de la Sismología en Chile. Instituto de Geofísica y Sismología, Universidad de Chile, Santiago de Chile.

Grevemeyer, I., Ranero, C.R., Ivandic, M., 2018. Structure of oceanic crust and serpentinization at subduction trenches. Geosphere 14, 395–418.

Gusman, A.R., Murotani, S., Satake, K., Heidarzadeh, M., Gunawan, E., Watada, S., Schurr, B., 2015. Fault slip distribution of the 2014 Iquique, Chile, earthquake estimated from ocean-wide tsunami waveforms and GPS data. Geophysical Research Letters 42, 1053–1060.

Gutscher, M.A., Spakman, W., Bijwaard, H., Engdahl, E.R., 2000. Geodynamics of flat subduction: Seismicity and tomographic constraints from the Andean margin. Tectonics 19, 814–833.

Haberland, C., Rietbrock, A., 2001. Attenuation tomography in the western central Andes: A detailed insight into the structure of a magmatic arc. Journal of Geophysical Research 106, 11151–11167.

Hacker, B.R., Abers, G.A., Peacock, S.M., 2003a. Subduction factory 1. Theoretical mineralogy, densities, seismic wave speeds, and H 2 O contents. Journal of Geophysical Research 108, 2029.

Hacker, B.R., Peacock, S.M., Abers, G.A., Holloway, S.D., 2003b. Subduction factory 2. Are intermediate-depth earthquakes in subducting slabs linked to metamorphic dehydration reactions? Journal of Geophysical Research 108.

Hainzl, S., Sippl, C., Schurr, B., 2019. Linear Relationship Between Aftershock Productivity and Seismic Coupling in the Northern Chile Subduction Zone. Journal of Geophysical Research: Solid Earth 124.

Halpaap, F., Rondenay, S., Perrin, A., Goes, S., Ottemöller, L., Austrheim, H., Shaw, R.D., Eeken, T., 2019. Earthquakes track subduction fluids from slab source to mantle wedge sink. Science Advances 5, eaav7369.

Haschke, M., Günther, A., Melnick, D., Echtler, H., Reutter, K.J., Scheuber, E., Oncken, O., 2006. Central and Southern Andean Tectonic Evolution Inferred from Arc Magmatism, in: Oncken, O. (Ed.), The Andes - Active Subduction Orogeny. Springer, Berlin, Front. ear edition. pp. 337–353.

Hasegawa, A., Umino, N., Takagi, A., 1978. Double-planed structure of the deep seismic zone in the northeastern Japan arc. Tectonophysics 47, 43–58.

Hayes, G.P., Herman, M.W., Barnhart, W.D., Furlong, K.P., Riquelme, S., Benz, H., Bergman, E., Barrientos, S., Earle, P.S., Samsonov, S., 2014. Continuing megathrust earthquake potential in Chile after the 2014 Iquique earthquake. Nature 512, 295–298.

Hayes, G.P., Moore, G., Portner, D.E., Hearne, M., Flamme, H., Furtney, M., Smoczyk, G.M., 2018. Slab2, a comprehensive subduction zone geometry model. Science 362, 58–61.

Hayes, G.P., Wald, D.J., Johnson, R.L., 2012. Slab1.0: A three-dimensional model of global subduction zone geometries. Journal of Geophysical Research 117, 1–15.

Heit, B., Bianchi, M., Yuan, X., Kay, S.M., Sandvol, E., Kumar, P., Kind, R., Alonso, R.N., Brown, L.D., Comte, D., 2014. Structure of the crust and the lithosphere beneath the southern Puna plateau from teleseismic receiver functions. Earth and Planetary Science Letters 385, 1–11.

Heit, B., Koulakov, I., Asch, G., Yuan, X., Kind, R., Alcocer-Rodriguez, I., Tawackoli, S., Wilke, H., 2008. More constraints to determine the seismic structure beneath the Central Andes at 21S using teleseismic tomography analysis. Journal of South American Earth Sciences 25, 22–36.

Herman, M.W., Furlong, K.P., Hayes, G.P., Benz, H.M., 2016. Foreshock triggering of the 1 April 2014 Mw 8.2 Iquique, Chile, earthquake. Earth and Planetary Science Letters 447, 119–129.

Herrera, C., Cassidy, J.F., Dosso, S.E., Dettmer, J., Bloch, W., Sippl, C., Salazar, P., 2021. The Crustal Stress Field Inferred from Focal Mechanisms in Northern Chile. Geophysical Research Letters 48, 1–10.

Herrera, C., Cassidy, J.F., Dosso, S.E., Dettmer, J., Rivera, E., Ruiz, S., Vasyura-Bathke, H., 2023a. Source Parameters of the Mw 5.7 Pica Crustal Earthquake in Northern Chile. Seismological Research Letters 94, 100–112.

Herrera, C., Pasten-Araya, F., Cabrera, L., Potin, B., Rivera, E., Ruiz, S., Madariaga, R., Contreras-Reyes, E., 2023b. Rupture properties of the 2020 Mw 6.8 Calama (northern Chile) intraslab earthquake. Comparison with similar intraslab events in the region. Geophysical Journal International 232, 2070–2079.

Hoffmann, F., Metzger, S., Moreno, M., Deng, Z., Sippl, C., Ortega Culaciati, F., Oncken, O., 2018. Characterizing Afterslip and Ground Displacement Rate Increase Following the 2014 Iquique-Pisagua Mw 8.1 Earthquake, Northern Chile. Journal of Geophysical Research 123, 4171–4192.

Huang, Z., Tilmann, F., Comte, D., Zhao, D., 2019. P Wave Azimuthal Anisotropic Tomography in Northern Chile: Insight Into Deformation in the Subduction Zone. Journal of Geophysical Research: Solid Earth 124, 742–765.

von Huene, R., Ranero, C.R., 2003. Subduction erosion and basal friction along the sediment-starved convergent margin off Antofagasta, Chile. Journal of Geophysical Research: Solid Earth 108, 2079.

von Huene, R., Scholl, D.W., 1991. Observations at convergent margins concerning sediment subduction, subduction erosion, and the growth of continental crust. Reviews of Geophysics 29, 279–316.

Husen, S., Kissling, E., 2001. Postseismic fluid flow after the large subduction earthquake of Antofagasta, Chile. Geology 29, 847–850.

Husen, S., Kissling, E., Flueh, E.R., 2000. Local earthquake tomography of shallow subduction in north Chile: A combined onshore and offshore study. Journal of Geophysical Research 105, 28183–28198.

Husen, S., Kissling, E., Flueh, E.R., Asch, G., 1999. Accurate hypocenter determination in the shallow part of the Nazca subduction one in Northern Chile using a combined on-/offshore network. Geophysical Journal International 138, 687–701.

Igarashi, T., Kato, A., 2021. Evolution of aseismic slip rate along plate boundary faults before and after megathrust earthquakes. Communications Earth & Environment 2, 1–7.

Ihmlé, P.F., Ruegg, J.C., 1997. Source tomography by simulated annealing using broad-band surface waves and geodetic data: Application to the Mw = 8.1 Chile 1995 event. Geophysical Journal International 131, 146–158.

Jara, J., Sánchez-Reyes, H., Socquet, A., Cotton, F., Virieux, J., Maksymowicz, A., Díaz-Mojica, J., Walpersdorf, A., Ruiz, J., Cotte, N., Norabuena, E., 2018. Kinematic study of Iquique 2014 Mw 8.1 earthquake: Understanding the segmentation of the seismogenic zone. Earth and Planetary Science Letters 503, 131–143.

Jara, J., Socquet, A., Marsan, D., Bouchon, M., 2017. Long-Term Interactions Between Intermediate Depth and Shallow Seismicity in North Chile Subduction Zone. Geophysical Research Letters 44, 9283–9292.

Jarrin, P., Nocquet, J.M., Rolandone, F., Mora-Páez, H., Mothes, P., Cisneros, D., 2022. Current motion and deformation of the Nazca Plate: new constraints from GPS measurements. Geophysical Journal International 232, 842–863.

Jolivet, R., Simons, M., Duputel, Z., Olive, J.A., Bhat, H.S., Bletery, Q., 2020. Interseismic Loading of Subduction Megathrust Drives Long-Term Uplift in Northern Chile. Geophysical Research Letters 47, 1–11.

Kato, A., Fukuda, J., Kumazawa, T., Nakagawa, S., 2016. Accelerated nucleation of the 2014 Iquique, Chile Mw 8.2 Earthquake. Scientific Reports 6, 1–9.

Kato, A., Nakagawa, S., 2014. Multiple slow-slip events during a foreshock sequence of the 2014 Iquique, Chile Mw 8.1 earthquake. Geophysical Research Letters 41, 5420–5427.

Kato, A., Obara, K., Igarashi, T., Tsuruoka, H., Nakagawa, S., Hirata, N., 2012. Propagation of Slow Slip Leading Up to the 2011Mw 9.0 Tohoku-Oki Earthquake. Science 335, 705–708.

Kausel, E., 1986. Los terremotos de agosto 1868 y mayo 1877 que afectaron el sur del Peru y norte de Chile.pdf. Boletín Academia Chilena de Ciencias , 8–13.

Kausel, E., Campos, J., 1992. The Ms = 8 tensional earthquake of 9 December 1950 of northern Chile and its relation to the seismic potential of the region. Physics of the Earth and Planetary Interiors 72, 220–235.

Kawakatsu, H., 1986. Double seismic zones: Kinematics. Journal of Geophysical Research 91, 4811–4825.

Kendrick, E., Bevis, M., Smalley, R., Brooks, B., Vargas, R.B., Lauría, E., Fortes, L.P.S., 2003. The Nazca-South America Euler vector and its rate of change. Journal of South American Earth Sciences 16, 125–131.

Khazaradze, G., Klotz, J., 2003. Short- and long-term effects of GPS measured crustal deformation rates along the south central Andes. Journal of Geophysical Research: Solid Earth 108, 1–15.

Kirby, S., Engdahl, E.R., Denlinger, R., 1996. Intermediate-depth intraslab earthquakes and arc volcanism as physical expressions of crustal and uppermost mantle metamorphism in subducting slabs. Geophysical Monograph Series 96, 195–214.

Kita, S., Katsumata, K., 2015. Stress drops for intermediate-depth intraslab earthquakes beneath Hokkaido, northern Japan: Differences between the subducting oceanic crust and mantle events. Geochemistry, Geophysics, Geosystems 16, 552–562. arXiv:1605.08479.

Kita, S., Okada, T., Nakajima, J., Matsuzawa, T., Hasegawa, A., 2006. Existence of a seismic belt in the upper plane of the double seismic zone extending in the along-arc direction at depths of 70-100 km beneath NE Japan. Geophysical Research Letters 33, L24310.

Klotz, J., Angermann, D., Michel, G.W., Porth, R., Reigber, C., Reinking, J., Viramonte, J., Perdomo, R., Rios, V.H., Barrientos, S., Barriga, R., Cifuentes, O., 1999. GPS-derived deformation of the central andes including the 1995 antofagasta M(w) = 8.0 earthquake. Pure and Applied Geophysics 154, 709–730.

Klotz, J., Khazaradze, G., Angermann, D., Reigber, C., Perdomo, R., Cifuentes, O., 2001. Earthquake cycle dominates contemporary crustal deformation in Central and Southern Andes. Earth and Planetary Science Letters 193, 437–446.

Kopp, H., Flueh, E.R., Papenberg, C., Klaeschen, D., 2004. Seismic investigations of the O'Higgins Seamount Group and Juan Fernández Ridge: Aseismic ridge emplacement and lithosphere hydration. Tectonics 23, TC2009.

Koulakov, I., Sobolev, S.V., Asch, G., 2006. P - And S-velocity images of the lithosphere-asthenosphere system in the Central Andes from local-source tomographic inversion. Geophysical Journal International 167, 106–126.

Kuge, K., Kase, Y., Urata, Y., Campos, J., Perez, A., 2010. Rupture characteristics of the 2005 Tarapaca, northern Chile, intermediate-depth earthquake: Evidence for heterogeneous fluid distribution across the subducting oceanic plate? Journal of Geophysical Research 115, 1–15.

Lange, D., Tilmann, F., Barrientos, S., Contreras-Reyes, E., Methe, P., Moreno, M., Heit, B., Agurto-Detzel, H., Bernard, P., Vilotte, J.P., Beck, S.L., 2012. Aftershock seismicity of the 27 February 2010 Mw 8.8 Maule earthquake rupture zone. Earth and Planetary Science Letters 317-318, 413–425.

Lay, T., Nishenko, S., 2022. Updated concepts of seismic gaps and asperities to assess great earthquake hazard along South America. Proceedings of the National Academy of Sciences 119, e2216843119.

Lay, T., Yue, H., Brodsky, E.E., An, C., 2014. The 1 April 2014 Iquique, Chile, Mw 8.1 earthquake rupture sequence. Geophysical Research Letters 41, 3818–3825.

Legrand, D., Delouis, B., Dorbath, L., David, C., Campos, J., Marquéz, L., Thompson, J., Comte, D., 2007. Source parameters of the M w = 6.3 Aroma crustal earthquake of July 24, 2001 (northern Chile), and its aftershock sequence. Journal of South American Earth Sciences 24, 58–68.

Legrand, D., Tassara, A., Morales, D., 2012. Megathrust asperities and clusters of slab dehydration identified by spatiotemporal characterization of seismicity below the Andean margin. Geophysical Journal International 191, 923–931.

León-Ríos, S., Ruiz, S., Maksymowicz, A., Leyton, F., Fuenzalida, A., Madariaga, R., 2016. Diversity of the 2014 Iquique's foreshocks and aftershocks: clues about the complex rupture process of a Mw 8.1 earthquake. Journal of Seismology 20, 1059–1073.

Li, S., Moreno, M., Bedford, J., Rosenau, M., Oncken, O., 2015. Revisiting viscoelastic effects on interseismic deformation and locking degree: A case study of the peru-north chile subduction zone. Journal of Geophysical Research 120, 4522–4538.

Lin, G., Shearer, P.M., 2007. Estimating local Vp/Vs ratios within similar earthquake clusters. Bulletin of the Seismological Society of America 97, 379–388.

Liu, L., Zhou, Q., 2015. Deep recycling of oceanic asthenosphere material during subduction. Geophysical Research Letters 42, 2204–2211.

Lomnitz, C., 2004. Major Earthquakes of Chile: A Historical Survey, 1535-1960. Seismological Research Letters 75, 368–378.

Loveless, J.P., Allmendinger, R.W., Pritchard, M.E., González, G., 2010. Normal and reverse faulting driven by the subduction zone earthquake cycle in the northern Chilean fore arc. Tectonics 29, 1–16.

Ma, B., Geersen, J., Klaeschen, D., Contreras-Reyes, E., Riedel, M., Xia, Y., Tréhu, A.M., Lange, D., Kopp, H., 2023. Impact of the Iquique Ridge on structure and deformation of the north Chilean subduction zone. Journal of South American Earth Sciences 124, 104262.

Ma, B., Geersen, J., Lange, D., Klaeschen, D., Grevemeyer, I., Contreras-Reyes, E., Petersen, F., Riedel, M., Xia, Y., Tréhu, A.M., Kopp, H., 2022. Megathrust reflectivity reveals the updip limit of the 2014 Iquique earthquake rupture. Nature Communications 13, 3969.

Maksymowicz, A., Ruiz, J., Vera, E., Contreras-Reyes, E., Ruiz, S., Arraigada, C., Bonvalot, S., Bascuñan, S., 2018. Heterogeneous structure of the Northern Chile marine forearc and its implications for megathrust earthquakes. Geophysical Journal International 215, 1080–1097.

Malatesta, L.C., Bruhat, L., Finnegan, N.J., Olive, J.A.L., 2021. Co-location of the Downdip End of Seismic Coupling and the Continental Shelf Break. Journal of Geophysical Research: Solid Earth 126, e2020JB019589.

Malgrange, M., Madariaga, R., 1983. Complex distribution of large thrust and normal fault earthquakes in the Chilean subduction zone. Geophysical Journal of the Royal Astronomical Society 73, 489–505.

Martin, S., Rietbrock, A., Haberland, C., Asch, G., 2003. Guided waves propagating in subducted oceanic crust. Journal of Geophysical Research 108, 2536.

Masson, F., Dorbath, C., Martinez, C., Carlier, G., 2000. Local earthquake tomography of the Andes at 20S: Implications for the structure and building of the mountain range. Journal of South American Earth Sciences 13, 3–19.

Mavrommatis, A., Segall, P., Johnson, K.M., 2014. A decadal-scale deformation transient prior to the 2011 Mw 9.0 Tohoku-oki earthquake. Geophysical Research Letters 41, 4486–4494.

McCaffrey, R., 1992. Oblique Plate Convergence, Slip Vectors, and Forearc Deformation. Journal of Geophysical Research 97, 8905–8915.

McCaffrey, R., 1996. Estimates of modern arc-parallel strain rates in fore arcs. Geology 24, 27–30.

McGlashan, N., Brown, L., Kay, S., 2008. Crustal thickness in the central Andes from teleseismically recorded depth phase precursors. Geophysical Journal International 175, 1013–1022.

Meng, L., Huang, H., Bürgmann, R., Paul, J., Strader, A., 2015. Dual megathrust slip behaviors of the 2014 Iquique earthquake sequence. Earth and Planetary Science Letters 411, 177–187.

Metcalf, K., Kapp, P., 2015. Along-strike variations in crustal seismicity and modern lithospheric structure of the central Andean forearc. Geological Society of America Memoir 212, 61–78.

Métois, M., Socquet, A., Vigny, C., Carrizo, D., Peyrat, S., Delorme, A., Maureira, E., Valderas-Bermejo, M.C., Ortega, I., 2013. Revisiting the North Chile seismic gap segmentation using GPS-derived interseismic coupling. Geophysical Journal International 194, 1283–1294.

Métois, M., Vigny, C., Socquet, A., 2016. Interseismic Coupling, Megathrust Earthquakes and Seismic Swarms Along the Chilean Subduction Zone (3818S). Pure and Applied Geophysics 173, 1431–1449.

Miller, D., Foulger, G.R., Julian, B.R., 1998. Non-double-couple earthquakes - 2. Observations. Reviews of Geophysics 36, 551–568.

Miller, S.A., 2013. The Role of Fluids in Tectonic and Earthquake Processes. volume 54. Elsevier Inc.

Moreno, M., Haberland, C., Oncken, O., Rietbrock, A., Angiboust, S., Heidbach, O., 2014. Locking of the Chile subduction zone controlled by fluid pressure before the 2010 earthquake. Nature Geoscience 7, 292–296.

Moreno, M., Li, S., Melnick, D., Bedford, J., Baez, J.C., Motagh, M., Metzger, S., Vajedian, S., Sippl, C., Gutknecht, B.D., Contreras-Reyes, E., Deng, Z., Tassara, A., Oncken, O., 2018. Chilean megathrust earthquake recurrence linked to frictional contrast at depth. Nature Geoscience 11, 285–290.

Motagh, M., Schurr, B., Anderssohn, J., Cailleau, B., Walter, T.R., Wang, R., Vilotte, J.P., 2010. Subduction earthquake deformation associated with 14 November 2007, Mw 7.8 Tocopilla earthquake in Chile: Results from InSAR and aftershocks. Tectonophysics 490, 60–68.

Müller, R.D., Sdrolias, M., Gaina, C., Roest, W.R., 2008. Age, spreading rates, and spreading asymmetry of the world's ocean crust. Geochemistry, Geophysics, Geosystems 9, Q04006.

Münchmeyer, J., Bindi, D., Sippl, C., Leser, U., Tilmann, F., 2020. Low uncertainty multifeature magnitude estimation with 3-D corrections and boosting tree regression : application to North Chile. Geophysical Journal International 220, 142–159.

Myers, E.K., Roland, E.C., Tréhu, A.M., Davenport, K., 2022. Crustal Structure of the Incoming Iquique Ridge Offshore Northern Chile. Journal of Geophysical Research: Solid Earth 127.

Myers, S.C., Beck, S.L., Zandt, G., Wallace, T., 1998. Lithospheric-scale structure across the Bolivian Andes from tomographic images of velocity and attenuation for P and S waves. Journal of Geophysical Research 103, 21,233–21,252.

Nadeau, R.M., Johnson, L.R., 1998. Seismological studies at Parkfield VI: moment release rates and estimates of source parameters for small repeating earthquakes. Bulletin of the Seismological Society of America 88, 790–814.

Nippress, S.E., Rietbrock, A., 2007. Seismogenic zone high permeability in the Central Andes inferred from relocations of micro-earthquakes. Earth and Planetary Science Letters 263, 235–245.

Norabuena, E., Leffler-Griffin, L., Mao, A., Dixon, T., Stein, S., Sacks, I.S., Ocola, L., Ellis, M., 1998. Space Geodetic Observations of Nazca-South America Convergence Across the Central Andes. Science 279, 358–362.

Oncken, O., Hindle, D., Kley, J., Elger, K., Victor, P., Schemmann, K., 2006. Deformation of the Central Andean Upper Plate System Facts, Fiction, and Constraints for Plateau Models, in: The Andes, pp. 3–27.

Oncken, O., Sobolev, S.V., Stiller, M., Asch, G., Haberland, C., Mechie, J., Yuan, X., Lüchen, E., Giese, P., Wigger, P., Lueth, S., Scheuber, E., Götze, H.J., Brasse, H., Buske, S., Yoon, M., Shapiro, S.A., Rietbrock, A., Chong, G., Wilke, H., González, G., Bravo, P., Vieytes, H., Martinez, E., Rössling, R., Ricaldi, E., 2003. Seismic imaging of a convergent continental margin and plateau in the central Andes (Andean Continental Research Project 1996 (ANCORP'96). Journal of Geophysical Research 108, 2328.

Ozawa, S., Nishimura, T., Munekane, H., Suito, H., Kobayashi, T., Tobita, M., Imakiire, T., 2012. Preceding, coseismic, and postseismic slips of the 2011 Tohoku earthquake, Japan. Journal of Geophysical Research: Solid Earth 117, B07404.

Panning, M., Romanowicz, B., 2006. A three-dimensional radially anisotropic model of shear velocity in the whole mantle. Geophysical Journal International 167, 361–379.

Pasten-Araya, F., Potin, B., Azua, K., Sáez, M., AdenAntoniów, F., Ruiz, S., Cabrera, L., Ampuero, J., Nocquet, J.M., Rivera, L., Duputel, Z., 2022. AlongDip Segmentation of the Slip Behavior and Rheology of the Copiapó Ridge Subducted in NorthCentral Chile. Geophysical Research Letters , 1–11.

Pasten-Araya, F., Potin, B., Ruiz, S., Zerbst, L., Aden-Antoniow, F., Azua, K., Rivera, E., Rietbrock, A., Salazar, P., Fuenzalida, A., 2021. Seismicity in the upper plate of the Northern Chilean offshore forearc: Evidence of splay fault south of the Mejillones Peninsula. Tectonophysics 800.

Pasten-Araya, F., Salazar, P., Ruiz, S., Rivera, E., Potin, B., Maksymowicz, A., Torres, E., Villarroel, J., Cruz, E., Valenzuela, J., Jaldín, D., González, G., Bloch, W., Wigger, P., Shapiro, S.A., 2018. Fluids Along the Plate Interface Influencing the Frictional Regime of the Chilean Subduction Zone, Northern Chile. Geophysical Research Letters 45, 10,378–10,388.

Patzwahl, R., Mechie, J., Schulze, A., Giese, P., 1999. Two-dimensional velocity models of the Nazca Plate subduction zone between 19.5S and 25S from wide-angle seismic measurements during the CINCA95 project. Journal of Geophysical Research 104, 7293–7317.

Peacock, S.M., 2001. Are the lower planes of double seismic zones caused by serpentine dehydration in subducting oceanic mantle? Geology 29, 299–302.

Perfettini, H., Avouac, J.P., Ruegg, J.C., 2005. Geodetic displacements and aftershocks following the 2001 Mw = 8.4 Peru earthquake: Implications for the mechanics of the earthquake cycle along subduction zones. Journal of Geophysical Research 110, B09404.

Petersen, F., Lange, D., Ma, B., Grevemeyer, I., Geersen, J., 2021. Relationship Between Subduction Erosion and the Up-Dip Limit of the 2014 Mw 8.1 Iquique Earthquake. Geophysical Research Letters 48, e2020GL092207.

Peyrat, S., Campos, J., de Chabalier, J.B., Perez, A., Bonvalot, S., Bouin, M.P., Legrand, D., Nercessian, A., Charade, O., Patau, G., Clévédæ, E., Kausel, E., Bernard, P., Vilotte, J.P., 2006. Tarapacá intermediate-depth earthquake (Mw 7.7, 2005, northern Chile): A slab-pull event with horizontal fault plane constrained from seismologic and geodetic observations. Geophysical Research Letters 33, L22308.

Peyrat, S., Madariaga, R., Buforn, E., Campos, J., Asch, G., Vilotte, J.P., 2010. Kinematic rupture process of the 2007 Tocopilla earthquake and its main aftershocks from teleseismic and strong-motion data. Geophysical Journal International 182, 1411–1430.

Phillips, K., Clayton, R.W., Davis, P., Tavera, H., Guy, R., Skinner, S., Stubailo, I., Audin, L., Aguilar, V., 2012. Structure of the subduction system in southern Peru from seismic array data. Journal of Geophysical Research: Solid Earth 117.

Piña-Valdés, J., Socquet, A., Cotton, F., Specht, S., 2018. Spatiotemporal variations of ground motion in northern Chile before and after the 2014 mw8.1 iquique megathrust event. Bulletin of the Seismological Society of America 108, 801–814.

Poli, P., Prieto, G.A., 2016. Global rupture parameters for deep and intermediate-depth earthquakes. Journal of Geophysical Research 121, 8871–8887.

Portner, D.E., Rodríguez, E.E., Beck, S., Zandt, G., Scire, A., Rocha, M.P., Bianchi, M.B., Ruiz, M., França, G.S., Condori, C., Alvarado, P., 2020. Detailed Structure of the Subducted Nazca Slab into the Lower Mantle Derived From Continent-Scale Teleseismic P Wave Tomography. Journal of Geophysical Research: Solid Earth 125, 1–26.

Poulos, A., Monsalve, M., Zamora, N., de la Llera, J.C., 2019. An updated recurrence model for chilean subduction seismicity and statistical validation of its poisson nature. Bulletin of the Seismological Society of America 109, 66–74.

Pritchard, M.E., Ji, C., Simons, M., 2006. Distribution of slip from 11 Mw > 6 earthquakes in the northern Chile subduction zone. Journal of Geophysical Research: Solid Earth 111, B10302.

Pritchard, M.E., Norabuena, E.O., Ji, C., Boroschek, R., Comte, D., Simons, M., Dixon, T.H., Rosen, P.A., 2007. Geodetic, teleseismic, and strong motion constraints on slip from recent southern Peru subduction zone earthquakes. Journal of

Geophysical Research: Solid Earth 112, B03307.

Pritchard, M.E., Simons, M., 2006. An aseismic slip pulse in northern Chile and along-strike variations in seismogenic behavior. Journal of Geophysical Research: Solid Earth 111, 1–14.

Ramos, V.A., Cristallini, E.O., Pérez, D.J., 2002. The Pampean flat-slab of the Central Andes. Journal of South American Earth Sciences 15, 59–78.

Ramos, V.A., Folguera, A., 2009. Andean flat-slab subduction through time. Geological Society, London, Special Publications 327, 31–54.

Ranero, C.R., Morgan, J.P., McIntosh, K.D., Reichert, C., 2003. Flexural faulting and mantle serpentinization at the Middle American. Nature 425, 367–373.

Ranero, C.R., Sallarès, V., 2004. Geophysical evidence for hydration of the crust and mantle of the Nazca plate during bending at the north Chile trench. Geology 32, 549–552.

Ranero, C.R., Villaseñor, A., Morgan, J.P., Weinrebe, W., 2005. Relationship between bend-faulting at trenches and intermediate-depth seismicity. Geochemistry, Geophysics, Geosystems 6, Q12002.

Ratchkovski, N.A., Hansen, R., 2002. New Evidence for Segmentation of the Alaska Subduction Zone. Bulletin of the Seismological Society of America 92, 1754–1765.

Reginato, G., Vera, E., Contreras-Reyes, E., Tréhu, A.M., Maksymowicz, A., Bello-González, J.P., González, F., 2020. Seismic structure and tectonics of the continental wedge overlying the source region of the Iquique Mw8.1 2014 earthquake. Tectonophysics 796, 228629.

Reiss, M.C., Rümpker, G., Wölbern, I., 2018. Large-scale trench-normal mantle flow beneath central South America. Earth and Planetary Science Letters 482, 115–125.

Reutter, K.J., Charrier, R., Götze, H.J., Schurr, B., Wigger, P., Scheuber, E., Giese, P., Reuther, C.D., Schmidt, S., Rietbrock, A., Chong, G., Belmonte-Pool, A., 2006. The Salar de Atacama Basin: a Subsiding Block within the Western Edge of the Altiplano-Puna Plateau, in: The Andes, pp. 303–325.

Rietbrock, A., Ryder, I., Hayes, G.P., Haberland, C., Comte, D., Roecker, S.W., Lyon-Caen, H., 2012. Aftershock seismicity of the 2010 Maule Mw=8.8, Chile, earthquake: Correlation between co-seismic slip models and aftershock distribution? Geophysical Research Letters 39, L08310.

Rietbrock, A., Waldhauser, F., 2004. A narrowly spaced double-seismic zone in the subducting Nazca plate. Geophysical Research Letters 31, L10608.

Rivadeneyra-Vera, C., Bianchi, M., Assumpção, M., Cedraz, V., Julià, J., Rodríguez, M., Sánchez, L., Sánchez, G., Lopezmurua, L., Fernandez, G., Fugarazzo, R., Neves, F., Galhardo, L., Barbosa, J.R., Barbosa, C., Collaço, B., Calhau, J., Brasilio, E., Azevedo, P., Rocha, M., Facincani, E., Silva, T., Condori, F., Andujar, L., Fugarazzo, R., Gadea, M., Figueres, V., Latorres, E., Castro, H., Curbelo, A., 2019. An Updated Crustal Thickness Map of Central South America Based on Receiver Function Measurements in the Region of the Chaco, Pantanal, and Paraná Basins, Southwestern Brazil. Journal of Geophysical Research: Solid Earth 124, 8491–8505.

Rosenbaum, G., Giles, D., Saxon, M., Betts, P.G., Weinberg, R.F., Duboz, C., 2005. Subduction of the Nazca Ridge and the Inca Plateau: Insights into the formation of ore deposits in Peru. Earth and Planetary Science Letters 239, 18–32.

Ruegg, J.C., Campos, J., Armijo, R., Barrientos, S., Briole, P., Thiele, R., Arancibia, M., Cañuta, J., Duquesnoy, T., Chang, M., Lazo, D., Lyon-Caen, H., Ortlieb, L., Rossignol, J.C., Serrurier, L., 1996. The M W =8.1 Antofagasta (North Chile) Earthquake of July 30, 1995: First results from teleseismic and geodetic data. Geophysical Research Letters 23, 917–920.

Ruegg, J.C., Olcay, M., Lazo, D., 2001. Co-, post- and pre(?)-seismic displacements associated with the Mw 8.4 southern Peru earthquake of 23 June 2001 from continuous GPS measurements. Seismological Research Letters 72, 673–678.

Ruiz, J.A., Maksymowicz, A., Ortega-Culaciati, F., Rivera, L., Comte, D., 2019. Source characteristics of the March 16, 2014 Mw 6.7 earthquake and its implications for the Mw 8.2 Pisagua mainshock. Tectonophysics 767, 228170.

Ruiz, S., Madariaga, R., 2018. Historical and recent large megathrust earthquakes in Chile. Tectonophysics 733, 37–56.

Ruiz, S., Métois, M., Fuenzalida, A., Ruiz, J., Leyton, F., Grandin, R., Vigny, C., Madariaga, R., Campos, J., 2014. Intense foreshocks and a slow slip event preceded the 2014 Iquique Mw 8.1 earthquake. Science 345, 1165–1170.

Rutland, R.W., 1971. Andean orogeny and ocean floor spreading. Nature 233, 252–255.

Ryan, J., Beck, S., Zandt, G., Wagner, L., Minaya, E., Tavera, H., 2016. Central Andean crustal structure from receiver function analysis. Tectonophysics 682, 120–133.

Salazar, D., Easton, G., Goff, J., Guendon, J.L., González-Alfaro, J., Andrade, P., Villagrán, X., Fuentes, M., León, T., Abad, M., Izquierdo, T., Power, X., Sitzia, L., Álvarez, G., Villalobos, A., Olguín, L., Yrarrázaval, S., González, G., Flores, C., Borie, C., Castro, V., Campos, J., 2022. Did a 3800-year-old Mw ˜9.5 earthquake trigger major social disruption in the Atacama Desert? Science Advances 8.

Salazar, P., Kummerow, J., Wigger, P., Shapiro, S.A., Asch, G., 2017. State of stress and crustal fluid migration related to west-dipping structures in the slab-forearc system in the northern Chilean subduction zone. Geophysical Journal International 208, 1403–1413.

Sandiford, D., Moresi, L., Sandiford, M., Farrington, R., Yang, T., 2020. The fingerprints of flexure in slab seismicity. Tectonics 39, e2019TC005894.

Savage, J.C., 1983. A dislocation model of strain accumulation and release at a subduction zone. Journal of Geophysical Research 88, 4984–4996.

Schaller, T., Andersen, J., Götze, H.J., Koproch, N., Schmidt, S., Sobiesiak, M., Splettstößer, S., 2015. Segmentation of the Andean margin by isostatic models and gradients. Journal of South American Earth Sciences 59, 69–85.

Scheuber, E., Andriessen, P.A.M., 1990. The kinematic and geodynamic significance of the Atacama fault zone, northern Chile. Journal of Structural Geology 12, 243–257.

Schurr, B., Asch, G., Hainzl, S., Bedford, J., Hoechner, A., Palo, M., Wang, R., Moreno, M., Bartsch, M., Zhang, Y., Oncken, O., Tilmann, F., Dahm, T., Victor, P., Barrientos, S., Vilotte, J.P., 2014. Gradual unlocking of plate boundary controlled initiation of the 2014 Iquique earthquake. Nature 512, 299–302.

Schurr, B., Asch, G., Rietbrock, A., Kind, R., Pardo, M., Heit, B., Monfret, T., 1999. Seismicity and average velocities beneath the Argentine Puna plateau. Geophysical Research Letters 26, 3025–3028.

Schurr, B., Asch, G., Rietbrock, A., Trumbull, R., Haberland, C., 2003. Complex patterns of fluid and melt transport in the central Andean subduction zone revealed by attenuation tomography. Earth and Planetary Science Letters 215, 105–119.

Schurr, B., Asch, G., Rosenau, M., Wang, R., Oncken, O., Barrientos, S., Salazar, P., Vilotte, J.P., 2012. The 2007 M7.7 Tocopilla northern Chile earthquake sequence: Implications for along-strike and downdip rupture segmentation and megathrust frictional behavior. Journal of Geophysical Research 117, B05305.

Schurr, B., Moreno, M., Tréhu, A.M., Bedford, J., Kummerow, J., Li, S., Oncken, O., 2020. Forming a Mogi Doughnut in the Years Prior to and Immediately Before the 2014 M8.1 Iquique, Northern Chile, Earthquake. Geophysical Research Letters 47.

Schurr, B., Rietbrock, A., 2004. Deep seismic structure of the Atacama basin, northern Chile. Geophysical Research Letters 31, 10–13.

Schurr, B., Rietbrock, A., Asch, G., Kind, R., Oncken, O., 2006. Evidence for lithospheric detachment in the central Andes from local earthquake tomography. Tectonophysics 415, 203–223.

Scire, A., Biryol, C.B., Zandt, G., Beck, S.L., 2015. Imaging the Nazca slab and surrounding mantle to 700 km depth beneath the central Andes (18 S to 28 S). Geological Society of America Memoir 212, 23–41.

Shillington, D.J., Becel, A., Nedimovic, M.R., Kuehn, H., Webb, S.C., Abers, G.A., Keranen, K.M., Li, J., Delescluse, M., Mattei-Salicrup, G.A., 2015. Link between plate fabric, hydration and subduction zone seismicity in Alaska. Nature Geoscience 8, 961–964.

Shirzaei, M., Bürgmann, R., Oncken, O., Walter, T.R., Victor, P., Ewiak, O., 2012. Response of forearc crustal faults to the megathrust earthquake cycle: InSAR evidence from Mejillones Peninsula, Northern Chile. Earth and Planetary Science Letters 333-334, 157–164.

Shrivastava, M., González, G., Moreno, M., Soto, H., Schurr, B., Salazar, P., Báez, J.C., 2019. Earthquake segmentation in northern Chile correlates with curved plate geometry. Scientific Reports 9, 1–10.

Sick, C., Yoon, M.K., Rauch, K., Buske, S., Lüth, S., Araneda, M., Bataille, K., Chong, G., Giese, P., Krawczyk, C., Mechie, J., Meyer, H., Oncken, O., Reichert, C., Schmitz, M., Shapiro, S., Stiller, M., Wigger, P., 2006. Seismic Images of Accretive and Erosive Subduction Zones from the Chilean Margin, in: Oncken, O. (Ed.), The Andes - Active Subduction Orogeny. Springer, Berlin, Front. ear edition. pp. 147–169.

Sippl, C., Dielforder, A., John, T., Schmalholz, S.M., 2022. Global Constraints on Intermediate-Depth Intraslab Stresses From Slab Geometries and Mechanisms of Double Seismic Zone Earthquakes. Geochemistry, Geophysics, Geosystems 23, e2022GC010498.

Sippl, C., Moreno, M., Benavente, R., 2021. Microseismicity appears to outline highly coupled regions on the Central Chile megathrust. Journal of Geophysical Research: Solid Earth 126, e2021JB022252.

Sippl, C., Schurr, B., Asch, G., Kummerow, J., 2018. Seismicity Structure of the Northern Chile Forearc from >100,000 double-difference relocated hypocenters. Journal of Geophysical Research 123, 4063–4087.

Sippl, C., Schurr, B., John, T., Hainzl, S., 2019. Filling the gap in a double seismic zone : Intraslab seismicity in Northern Chile. Lithos 346-347, 105155.

Sippl, C., Schurr, B., Münchmeyer, J., Barrientos, S., Oncken, O., 2023. Catalogue of Earthquake Hypocenters for Northern Chile from 2007-2021 using IPOC (plus auxiliary) seismic stations.

Ślęzak, K., Díaz, D., Vargas, J.A., Cordell, D., Reyes-Cordova, F., Segovia, M.J., 2021. Magnetotelluric image of the Chilean subduction zone in the Salar de Atacama region (23-24S): Insights into factors controlling the distribution of volcanic arc magmatism. Physics of the Earth and Planetary Interiors 318, 106765.

Socquet, A., Valdes, J.P., Jara, J., Cotton, F., Walpersdorf, A., Cotte, N., Specht, S., Ortega Culaciati, F., Carrizo, D., Norabuena, E., 2017. An 8month slow slip event triggers progressive nucleation of the 2014 Chile megathrust. Geophysical Research Letters 44, 4046–4053.

Sodoudi, F., Yuan, X., Asch, G., Kind, R., 2011. High-resolution image of the geometry and thickness of the subducting Nazca lithosphere beneath northern Chile. Journal of Geophysical Research 116, B04302.

Song, T.R.A., Simons, M., 2003. Large trench-parallel gravity variations predict seismogenic behavior in subduction zones. Science 301, 630–633.

Soto, H., Sippl, C., Schurr, B., Kummerow, J., Asch, G., Tilmann, F., Comte, D., Ruiz, S., Oncken, O., 2019. Probing the Northern Chile megathrust with seismicity-The 2014 M8.1 Iquique earthquake sequence. Journal of Geophysical Research 124, 12,935–12,954.

Springer, M., 1999. Interpretation of heat-flow density in the Central Andes, in: Tectonophysics, pp. 377–395.

Stachnik, J.C., Abers, G.A., Christensen, D., 2004. Seismic attenuation and mantle wedge temperatures in the Alaska subduction zone. Journal of Geophysical Research 109, B10304.

Storch, I., Buske, S., Schmelzbach, C., Wigger, P., 2016. Seismic imaging of a megathrust splay fault in the North Chilean subduction zone (Central Andes). Tectonophysics 689, 157–166.

Storch, I., Buske, S., Victor, P., Oncken, O., 2021. Seismic images of the Northern Chilean subduction zone at 1940S, prior to the 2014 Iquique earthquake. Geophysical Journal International 225, 1048–1061.

Storch, I., Buske, S., Victor, P., Oncken, O., 2023. A Topographic Depression on the Subducting Nazca Plate Controls Rupture Processes of the April 1st 2014 M8.1 Iquique Earthquake in Northern Chile. Tectonophysics 847, 229684.

Storchak, D.A., Giacomo, D.D., Bondár, I., Engdahl, E.R., Harris, J., Lee, W.H., Villaseñor, A., Bormann, P., 2013. Public release of the ISC-GEM global instrumental earthquake catalogue (1900-2009). Seismological Research Letters 84, 810–815.

Sun, T., Saffer, D., Ellis, S., 2020. Mechanical and hydrological effects of seamount subduction on megathrust stress and slip. Nature Geoscience 13, 249–255.

Syracuse, E., van Keken, P., Abers, G.A., Suetsugu, D., Bina, C., Inoue, T., Wiens, D.A., Jellinek, A.M., 2010. The global range of subduction zone thermal models. Physics of the Earth and Planetary Interiors 183, 73–90.

Tassara, A., Echaurren, A., 2012. Anatomy of the Andean subduction zone: Three-dimensional density model upgraded and compared against global-scale models. Geophysical Journal International 189, 161–168.

Tassara, A., Götze, H.J., Schmidt, S., Hackney, R., 2006. Three-dimensional density model of the Nazca plate and the Andean continental margin. Journal of Geophysical Research 111, B09404.

Tassara, C., Cesca, S., Miller, M., Sippl, C., Cort, J., Schurr, B., 2022. Seismic source analysis of two anomalous earthquakes in Northern Chile. Journal of South American Earth Sciences 119, 103948.

Twardzik, C., Duputel, Z., Jolivet, R., Klein, E., Rebischung, P., 2022. Bayesian inference on the initiation phase of the 2014 Iquique, Chile, earthquake. Earth and Planetary Science Letters 600, 117835.

Universidad de Chile, 2013. Red Sismologica Nacional. International Federation of Digital Seismograph Networks.

Valenzuela-Malebran, C., Cesca, S., López-Comino, J., Zeckra, M., Krüger, F., Dahm, T., 2022. Source mechanisms and rupture processes of the Jujuy seismic nest, Chile-Argentina border. Journal of South American Earth Sciences 117, 103887.

Vavryčuk, V., Hrubcová, P., 2017. Seismological evidence of fault weakening due to erosion by fluids from observations of intraplate earthquake swarms. Journal of Geophysical Research: Solid Earth 122, 3701–3718.

Victor, P., Oncken, O., Glodny, J., 2004. Uplift of the western Altiplano plateau: Evidence from the Precordillera between 20and 21S (northern Chile). Tectonics 23, TC4004.

Victor, P., Sobiesiak, M., Glodny, J., Nielsen, S.N., Oncken, O., 2011. Long-term persistence of subduction earthquake segment boundaries: Evidence from Mejillones Peninsula, northern Chile. Journal of Geophysical Research 116, B02402.

Vigny, C., Klein, E., 2022. The 1877 megathrust earthquake of North Chile may be two times smaller than previously thought: a review of ancient articles. Journal of South American Earth Sciences , 103878.

Wada, I., Wang, K., 2009. Common depth of slab-mantle decoupling: Reconciling diversity and uniformity of subduction zones. Geochemistry, Geophysics, Geosystems 10, Q10009.

Waldhauser, F., Ellsworth, W.L., 2000. A Double-difference Earthquake location algorithm: Method and application to the Northern Hayward Fault, California. Bulletin of the Seismological Society of America 90, 1353–1368.

Wang, K., Huang, T., Tilmann, F., Peacock, S.M., Lange, D., 2020. Role of Serpentinized Mantle Wedge in Affecting Megathrust Seismogenic Behavior in the Area of the 2010 M = 8.8 Maule Earthquake. Geophysical Research Letters 47, e2020GL090482.

Wang, R., Gu, Y.J., Schultz, R., Chen, Y., 2018. Faults and Non-Double-Couple Components for Induced Earthquakes. Geophysical Research Letters 45, 8966–8975.

Ward, K.M., Porter, R.C., Zandt, G., Beck, S.L., Wagner, L.S., Minaya, E., Tavera, H., 2013. Ambient noise tomography across the Central Andes. Geophysical Journal International 194, 1559–1573.

Wells, R.E., Blakely, R.J., Sugiyama, Y., Scholl, D.W., Dinterman, P.A., 2003. Basin-centered asperities in great subduction zone earthquakes: A link between slip, subsidence, and subduction erosion? Journal of Geophysical Research 108, 2507.

Wigger, P., Salazar, P., Kummerow, J., Bloch, W., Asch, G., Shapiro, S.A., 2016. West–Fissure- and Atacama-Fault Seismic Network (2005/2012).

Williamson, A.L., Newman, A.V., 2018. Limitations of the Resolvability of Finite-Fault Models Using Static Land-Based Geodesy and Open-Ocean Tsunami Waveforms. Journal of Geophysical Research: Solid Earth 123, 9033–9048.

Wimpenny, S., Craig, T.J., Marcou, S., 2022. Re-examining temporal variations in intermediate-depth seismicity. Preprint on EarthArXiV .

Withers, M., Aster, R.C., Young, C., Beiriger, J., Harris, M., Moore, S., Trujillo, J., 1998. A comparison of select trigger algorithms for automated global seismic phase and event detection. Bulletin of the Seismological Society of America 88, 95–106.

Wölbern, I., Heit, B., Yuan, X., Asch, G., Kind, R., Viramonte, J., Tawackoli, S., Wilke, H., 2009. Receiver function images from the Moho and the slab beneath the Altiplano and Puna plateaus in the Central Andes. Geophysical Journal International 177, 296–308.

Wörner, G., Moorbath, S., Harmon, R.S., 1992. Andean Cenozoic volcanic centers reflect basement isotopic domains. Geology 20, 1103–1106.

Yagi, Y., Okuwaki, R., Enescu, B., Hirano, S., Yamagami, Y., Endo, S., Komoro, T., 2014. Rupture process of the 2014 Iquique Chile earthquake in relation with the foreshock activity. Geophysical Research Letters 41, 4201–4206.

Yokota, Y., Koketsu, K., 2015. A very long-term transient event preceding the 2011 Tohoku earthquake. Nature Communications 6, 5934.

Yoon, M., Buske, S., Shapiro, S.A., Wigger, P., 2009. Reflection Image Spectroscopy across the Andean subduction zone. Tectonophysics 472, 51–61.

Yuan, X., Sobolev, S.V., Kind, R., 2002. Moho topography in the Central Andes and its geodynamic implications. Earth and Planetary Science Letters 199, 389–402.

Yuan, X., Sobolev, S.V., Kind, R., Oncken, O., Bock, G., Asch, G., Schurr, B., Graeber, F., Rudloff, A., Hanka, W., Wylegalla, K., Tibi, R., Haberland, C., Rietbrock, A., Giese, P., Wigger, P., Roewer, P., Zandt, G., Beck, S.L., Wallace, T., Pardo, M., Comte, D., 2000. Subduction and collision processes in the Central Andes constrained by converted seismic phases. Nature 408, 958–961.

Zhan, Z., 2020. Mechanisms and Implications of Deep Earthquakes. Annual Review of Earth and Planetary Sciences 48, 147–174.

Figure 1.

Overview map for the Northern Chile region, showing bathymetry/topography from the GEBCO grid (GEBCO_Compilation_Group, 2020). Colored dashed lines in the ocean show isolines of oceanic plate age (after Müller et al., 2008), blue solid lines onshore show depth contours of the slab surface according to the slab2 model (Hayes et al., 2018). The green barbed line marks the location of the megathrust at the surface. Black and red triangles represent volcanoes that have been active since the Pleistocene (black) or Holocene (red) according to the Global Volcanism Program (Global_Volcanism_Program, 2013). The two violet east-west trending lines describe the extent of the topography profiles that are plotted in the upper right inset. CC - Coastal Cordillera; WC - Western Cordillera; PVG - Pica Volcanic Gap. Left panel shows the approximate rupture extents of past megathrust earthquakes with $M>8$ (red lines) and $7<M<8$ (green lines), compiled from Ruiz and Madariaga (2018) and Schurr et al. (2014). The dashed red line shows the possibly shorter extent of the 1877 event advocated by Vigny and Klein (2022).

Figure 2.

Geological map of forearc, arc and backarc of Central South America. Map is based on Geological Map of South America (at the scale 1:5.000.000; Gómez et al., 2019).

Figure 3.

Overview over permanent and temporary seismic networks in Northern Chile since 2006. Permanent stations are shown with large triangles, and their names and year of installation is given. Stations from temporary deployments are indicated with smaller triangles, and colored according to the network as listed in the legend.

Figure 4.

Classification of seismicity into different event classes. a) In the updip part of the slab, distance from the slab surface model of Sippl et al. (2018) is used as a criterion to differentiate between upper plate (UP; magenta) and plate interface (P1; blue) earthquakes, as well as events in the upper plane (P2; green) and lower plane (P3; red) of the double seismic zone. b) Example cross section (W-E at 21.75°S) with the different event classes indicated by color.

Figure 5.

Separation of shallow events into upper plate (UP) and mining-related (MI) classes. Colored dots are earthquake epicenters color-coded by hypocentral depth, inverted red triangles mark the location of mining activity as determined from GoogleEarth imagery. a) Map view plots of the different event classes as defined in the text. (left) All events that fall into the upper plate categorization of Sippl et al. (2018). (center) with mining-related events (epicenter within 15 km distance from a mapped mining location; hypocentral depth <15 km) removed. (right) events that were classified as mining-related. b) Histograms of time-of-day (in Chilean local time) of earthquake occurrence within the newly defined classes UP and MI. It is evident that MI events (upper subplot) occur exclusively during daytime, and most frequently between 10 am and 8 pm. UP events (lower subplot), in contrast, are rather evenly distributed across all hours of the day. The slight peak around 1-2 pm that correlates with the maximum of the mining-related activity may indicate that some few mining-related events are still contained in class UP.

Figure 6.

Summary plot of the IPOC seismicity catalog, which contains 182,847 events throughout the years 2007 to 2021. The map view plot in the upper left shows epicenters color-coded by hypocentral depths, the projections onto a single longitudinal and latitudinal plane as well as the plots of latitude, longitude and depth against time show logarithmic event densities instead of single hypocenters.

Figure 7.

W-E cross sections through the IPOC catalog at different latitudes (noted in the different subplots), showing logarithmic event densities of a 100 km wide swath centered on the nominal latitude. The shown profiles are identical in terms of placement and swath width to the ones shown in Sippl et al. (2018), but differ in the visualized catalog (more events) as well as the type of visualization.

Figure 8.

Overview of published maps of interplate locking plus their average for Northern Chile. Depending on their parameterization, locking models are either shown with blocks of constant locking (Béjar-Pizarro et al., 2013; Métois et al., 2016) or as interpolated maps with contour lines every 0.2 units of locking degree (Chlieh et al., 2011; Schurr et al., 2014; Li et al., 2015; Hoffmann et al., 2018; Schurr et al., 2020; Jolivet et al., 2020). Green lines show rupture contours of the 2014 Iquique earthquake and its largest aftershock (in the north; after Schurr et al., 2014), the 2007 Tocopilla earthquake (center; after Schurr et al., 2012) and the 1995 Antofagasta earthquake (in the south; after Ruegg et al., 1996). The upper left map shows residual gravity after Bassett and Watts (2015), and contains labels for the three highly locked segments of Métois et al. (2013) (Paranal, Loa, Camarones). IB - Iquique Basin.

Figure 9.

Left: Map of interplate seismicity superimposed on dimmed average locking structure (see Figure 8). Epicenters of historical earthquakes (after Comte and Pardo, 1991) are shown with diamonds, epicenters of instrumental earthquakes with blue stars (from ISC-GEM catalog; Storchak et al., 2013). The blue ellipse is the estimated rupture size of the 1877 earthquake (after Vigny and Klein, 2022). Green stars denote epicenters of major earthquakes from our catalog, and green contour lines show their 1 m slip contours. Right: Time versus latitude for interplate seismicity. The aftershock series of the 2 major earthquakes covered by our catalog, the M7.8 2007 Tocopilla event and the M8.1 2014 Iquique event with its M7.6 aftershock, are clearly visible. Circle size in both subfigures scales with rupture size, scaling for the right subplot is indicated in the bottom right corner.

Figure 10.

a) Background seismicity (blue circles) from our catalog, plotted together with slip contours of the Iquique, Tocopilla and Antofagasta earthquakes. The swath width used for the profiles in b) is indicated along the coast. b) Swath profiles across the different locking models, residual gravity and normalized background event density.

Figure 11.

Slip and aftershocks of the M8.1 1995 Antofagasta and M7.8 2007 Tocopilla earthquakes. Green circles are relocated aftershocks of the Antofagasta event (Nippress and Rietbrock, 2007); red circles are from our new catalog (6 months of data from 1/11/2007 to 1/5/2008). Slip and net aseismic afterslip of the Antofagasta event are from Chlieh et al. (2004), afterslip for the Tocopilla event from Béjar-Pizarro et al. (2010). The slip values indicated in the boxes are in meters. The epicenters of the main shocks are shown as stars. Three previous events with M>7 are also plotted (Malgrange and Madariaga, 1983; Pritchard et al., 2006). Blue beachballs correspond to the Dec. 16 2007 Michilla aftershock that broke the lower plate.

Figure 12.

a) Overview map of inter-, pre-, co-, and post-seismic phenomena accompanying the April 1 2014 M8.1 Iquique earthquake. Green circles and beachballs depict events before the March 16, 2014 foreshock, red circles and beachballs depict foreshocks after March 16, 2014, the orange beachball shows the first and largest foreshock in the upper plate. Black contours are 2 m of mainshock slip (black beachball); purple contours are 0.5 m slip of the largest M7.6 aftershock on April 3, 2014 (Duputel et al., 2015). Stars depict earthquake repeater sequences (Schurr et al., 2020) in the inter-seismic (green) and pre-seismic (red) periods. Symbol size is scaled by number of repeaters per sequence (27). Symbol filling allows to identify clusters in (d). Red ellipse outlines the aseismic slip region accompanying the foreshock sequence, as suggested by several studies (Socquet et al., 2017; Kato et al., 2016; Meng et al., 2015; Ruiz et al., 2014; Twardzik et al., 2022). Light green contours outline 5 mm preseismic (8 months prior to mainshock) slip (Socquet et al., 2017), blue contours outline 60/80 cm postseismic slip (Hoffmann et al., 2018). The green ellipse shows the suggested 2-month slow slip by Boudin et al. (2022), and the dark red ellipse the suggested 2-week slow slip by the same authors from tilt and GNSS. b) Time vs. latitude for the two-week foreshock sequence. Black arrow indicates the observed northward propagation of the sequence. Background arrows indicate accompanying aseismic slip. c) multi-month aseismic slip precursor according to Socquet et al. (2017) and Boudin et al. (2022), also showing earthquake and repeater clusters that may have set off the transients. d) Multi-year time versus latitude plot showing earthquake repeater clusters. The filling of the stars is the same as in the map view plot (subfigure a).

Figure 13.
Published slip models for the 2014 M_w 8.1 Iquique mainshock. 1 m slip contour lines are drawn in green.

Figure 14.
Series of W-E profiles through the IPOC seismicity catalog, showing earthquake hypocenters as hollow black circles. In the left column, four different available models of the slab geometry, slab1.0 (Hayes et al., 2012), slab2 (Hayes et al., 2018), the model derived from an earlier version of the IPOC catalog (Sippl et al., 2018) as well as the model of Tassara and Echaurren (2012), are overlain. In the right column, seismicity is plotted atop profile sections through the S-wave velocity model of Gao et al. (2021). Additionally, geometries of the oceanic (orange) and continental (red) Moho, taken from receiver function studies, is plotted for the cross sections where they are available. For the sections at 20 and 22°S, these are taken from Sodoudi et al. (2011), in the section at 21°S the Moho geometries are from Wölbern et al. (2009). Yellow stars in the cross section at 20°S mark the hypocenters of the aftershock series of the 2005 Tarapacá earthquake (taken from Peyrat et al., 2006).

Figure 15.
Projection of T-axis orientations of intraslab earthquakes (mechanism compilation of Sippl et al., 2019) into a W-E profile. The profile is centered at 21.5°S, seismicity hypocenters are shown with black circles, T-axis orientations are displayed with bars. Bar orientations correspond to T-axis dip angles, their lengths are proportional to the in-plane part of their azimuthal orientation (azimuth 90° means in-plane only, i.e. maximum bar length; azimuth 0° means azimuth perpendicular to the projection plane, i.e. shown as a dot only). Bar color is green when the dip angle deviates by more than 30 degrees from the slab dip, if the deviation is smaller the color is red. Blue curve shows an estimate of slab bending and unbending derived from slab geometry (Sippl et al., 2022).

Figure 16.
a) Map view projection of T-axis orientations (dataset of Sippl et al., 2019) for earthquakes inside the deep cluster. Bar length corresponds to T-axis dip angle (full length means horizontal, minimum length means vertical orientation). b) Along-strike evolution of mean T-axis azimuth (solid line; dashed lines show mean

plus and minus standard deviation), computed in a 0.5° moving window.

Figure 17.

Temporal evolution of monthly event numbers of all intermediate-depth earthquakes (blue) compared to the latitudinal range of the Tarapacá rupture (red; 19.7 to 20.25°S). The upper panel shows all events, the lower one only events with magnitudes above 2.7 (the completeness magnitude estimated by Hainzl et al., 2019). Total event numbers decline in the upper plot, whereas they stay largely constant in the lower one, which is a hint that the detection threshold of events may have deteriorated as a consequence of changing network geometry. For the Tarapacá region, both plots show a clear decrease of event numbers over time.

Figure 18.

Comparison of aftershock productivity for roughly similar-sized (M∼6) earthquakes from different tectonic regimes. (Left) Overview map that shows the epicenters of the six investigated events in the context of the entire seismicity catalog, marked by stars. Their colors indicate the classification of the events (same color scheme as in Figure 4), and the number next to each event is the hypocentral depth in kilometers. (Right) Magnitude-vs-time plot of events within a volume of +-20 km around each hypocenter in all three dimensions. Magnitudes of all events within that volume within a timespan from one year before to two years after the main event (black cross and line) are shown. Grey shading means that the catalog contains no data for this time interval. Note that events 1 and 2 (situated in the upper plate and within the uppermost part of the slab) feature clear aftershock series, with seismicity still clearly above background levels one year after the main event. On the plate interface, aftershock series appear to decay faster but are still clearly discernible, while it is hard to identify any aftershock activity in the deeper parts of the slab.

Figure 19.

Comparison of published thermal models for the Northern Chile subduction zone. All models are plotted on top of a seismicity W-E section at 21.5°S. Dashed lines show isotherms every 200°C, with coloring explained in the legend at the bottom. Note that the models were produced for different latitudes, which results in small geometrical discrepancies relative to the seismicity due to along-strike changes in slab shape. a) Section through the 3D model of Araya Vargas et al. (2021), taken at 22°S. b) 2D model of Cabrera et al. (2021) (at ∼19°S) c) 2D model of Springer (1999) (for ∼21°S) d) 2D model of Wada and Wang (2009) (for 24°S). Note that the lower plane of double seismic zone seismicity is situated in the vicinity of the 600°C isotherm for all models except Springer (1999), where it plots on the 400°C isotherm.

Figure 20.

Thickness of the oceanic crust of the Nazca Plate offshore Northern Chile. The background map is from

Tassara et al. (2006), interpolated based on the vertices shown with colored circles. Small inverted triangles are crustal thicknesses from 2D seismic velocity models based on CINCA95 reflection profiles (Patzwahl et al., 1999), large inverted triangles are seismic reflection results from Ranero and Sallarès (2004, to the south) and Myers et al. (2022, to the north).

Figure 21.

Crustal thickness map of Northern Chile. The background map shows the interpolated map of Assumpção et al. (2013), in the version modified by Rivadeneyra-Vera et al. (2019). Circles represent the crustal thickness values that were used to derive this map, compiled from a number of seismological studies (Dorbath et al., 1993; Beck et al., 1996; Yuan et al., 2000, 2002; McGlashan et al., 2008; Wölbern et al., 2009; Phillips et al., 2012; Heit et al., 2014; Ryan et al., 2016). The triangles represent crustal thicknesses along the two receiver function profiles of Sodoudi et al. (2011), as also shown in Figure 14.

Figure 22.

Summary of seismicity and seismic velocity structure of the upper plate forearc in Northern Chile. a) Color-coded hypocenters of upper plate events (class UP) in the IPOC catalog, overlain onto the 20 km depth slice of the tomography model of Gao et al. (2021). As in the original study, the tomography model is shown as v_s determined from v_{SV} and v_{SH} using the Voigt average (Panning and Romanowicz, 2006), green contour lines mark the velocity isolines at 3.25 and 3.75 km/s. b) Epicenters (black circles) and lower-hemisphere projections of focal mechanisms (only double-couple part) from the compilation of Herrera et al. (2021) that comprises the years 2005-2017 (blue), scaled by magnitude. Green focal mechanisms are from the 2001 Aroma earthquake sequence (Legrand et al., 2007), pink ones are taken from the GEOFON database. Red frame shows the extent of Figure 23. c) P-axis orientations from the focal mechanisms in subfigure b), with the length of each bar representing the dip angle of the P axis as shown in the legend. Blue axes are oriented closer to E-W, red axes closer to N-S. d) Projection of all hypocenters onto a single latitudinal plane. e) Temporal evolution of upper plate seismicity, shown in a latitude vs. time plot.

Figure 23.

Zoom-in to the region marked with a red square in Figure 22b. Shown are epicenters color-coded by hypocentral depth, plotted on top of a topography relief map, and beachballs that show the lower-hemisphere projection of focal mechanisms. Locations were taken from the IPOC catalog, the focal mechanisms are from Herrera et al. (2021). Dark green stars mark the location of the 2001 M_w 6.3 Aroma earthquake and its largest aftershock, their locations and focal mechanisms were taken from Legrand et al. (2007). Colored ellipses mark the different event clusters and are mirrored in the beachball coloring. The bottom panel is a longitude-time plot that visualizes the temporal activity patterns in the area. Colored frames correspond to the clusters marked in the upper panel.

Figure 24.

Upper plate seismicity and mechanisms between 20 and 22°S. a) Epicenters color-coded for hypocentral depths as well as lower-hemisphere projections of focal mechanisms plotted atop a topographic map. Locations are from the IPOC catalog, focal mechanisms in blue from Herrera et al. (2021). The green mechanism is the 2008 M_w 5.7 Pica earthquake, taken from Herrera et al. (2023a), the purple one the 2020 M_w6.2 Rio Loa earthquake taken from Tassara et al. (2022). b) Latitude vs. time plot, with the aftershock sequences of the Pica and Rio Loa events highlighted by green and purple boxes, respectively. c) W-E profile through the location of the 2020 Rio Loa earthquake. Red circles highlight hypocenters of events occurring within 20 days after the main event. Dashed lines mark the approximate locations of the plate interface (blue), upper (green) and lower (purple) plane of the DSZ. d) Zoom into the region marked by a red box in subfigure a), showing only those events that are contained in the profile projection of subfigure e. The blue line marks the profile orientation (perpendicular to the rupture plane as determined by Tassara et al., 2022), red circles again mark events within 20 days after the main event. e) Profile projection as outlined in subfigure d).

Figure 25.

Map view plots of event density for the different event classes. Due to the widely different seismicity rates, we chose different scales for the different classes, as well as a finer grid for the intermediate-depth events (ID). The upper panel shows (left) all ID events, (middle) only ID events in the deep part of the slab, i.e. situated >17 km below the slab surface as defined by the IPOC slab model, and (right) only events in the lower plane of the DSZ (P3). In the lower panel, we show upper plate events (UP; left), as well as overlays between ID and P3 (middle) and ID, P3 and UP (right).

Figure 26.

Event numbers of plate interface seismicity between 19 and 21°S, within a ten-day moving window. a) Overall event rates for the entire analyzed timespan. The red box corresponds to the zoom-in shown in subfigure b). b) Zoom into the time period just after the Iquique earthquake, showing the transition from an exponential decay in event numbers with time following the Omori law (green line) to a stable background rate roughly equivalent to pre-main shock levels (red line).

Figure 27.

Comparison of seismicity distributions of different event populations through time. Plate interface seismicity (upper row), upper plate (center row) as well as intraslab seismicity (lower row) between 19 and 21°S are compared for the time periods before, during and after the Iquique sequence. While hypocenters are visualized with hollow circles for plate interface (blue) and upper plate (magenta) events, intraslab events are shown with a color scale for event density to accommodate the much higher event numbers there. Blue, green, yellow, orange and red contour lines correspond to slip contours of the 2014 Iquique earthquake (2, 4, 6, 8 and 10 m of slip according to the model of Duputel et al., 2015).

Figure 28.

Analysis of event numbers (right column) and moment release (left column) for the entire catalog (a) as well as the preparatory phase of the Iquique earthquake (b). Following the plots in Bouchon et al. (2016) and Jara et al. (2017), we show intraslab earthquakes with the blue curve and plate interface earthquakes with the red curve. We limited our analysis to the along-strike region between 18.5 and 21°S, and excluded the M_w 8.1 Iquique main shock as well as the M_w 7.6 aftershock from the moment summation. Only events with magnitudes larger than M_c were included in the analysis. The left plot in b) is similar to Figure 3 in Bouchon et al. (2016), and the cyan markers show to time periods where they inferred interaction between the slab and the plate interface seismicity.

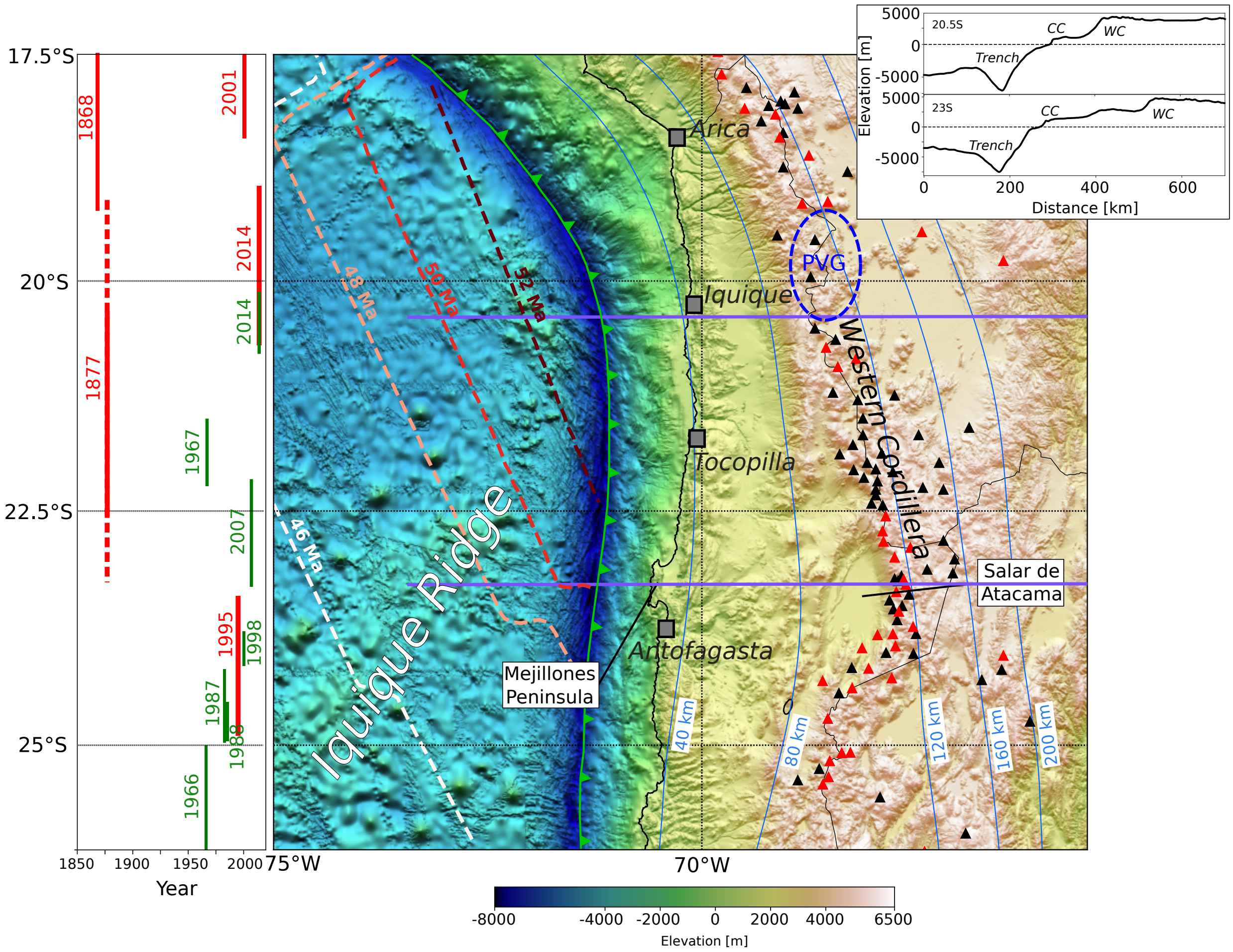

17.5°S
20°S
22.5°S
25°S
1868
1877
1967
1966
1987
1988
1995
1998
2007
2014
2014
2001
1850
1900
1950
2000
Year
75°W
70°W
Arica
Iquique
Tocopilla
Antofagasta
Mejillones Peninsula
Salar de Atacama
Iquique Ridge
Western Cordillera
PVG
48 Ma
50 Ma
52 Ma
46 Ma
40 km
80 km
120 km
160 km
200 km
Elevation [m]
-8000
-4000
-2000
0
2000
4000
6500
20.5S
23S
Trench
CC
WC
5000
-5000
Distance [km]
200
400
600

Figure 1:

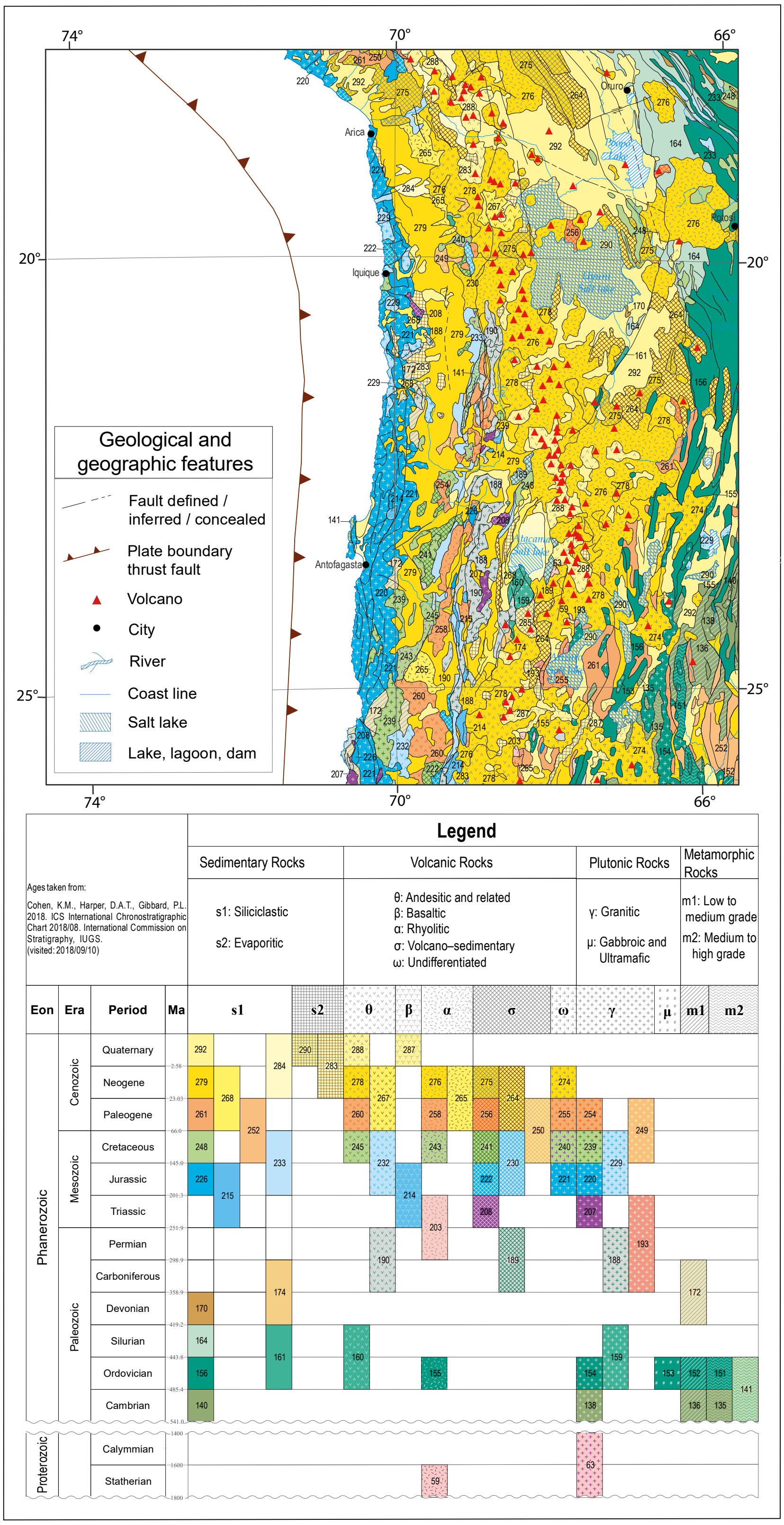
74°
70°
66°
20°
25°
Arica
Iquique
Antofagasta
Oruro
Potosí
Geological and geographic features
Fault defined / inferred / concealed
Plate boundary thrust fault
Volcano
City
River
Coast line
Salt lake
Lake, lagoon, dam
Legend
Sedimentary Rocks
Volcanic Rocks
Plutonic Rocks
Metamorphic Rocks
Ages taken from:
Cohen, K.M., Harper, D.A.T., Gibbard, P.L. 2018. ICS International Chronostratigraphic Chart 2018/08. International Commission on Stratigraphy, IUGS. (visited: 2018/09/10)
s1: Siliciclastic
s2: Evaporitic
θ: Andesitic and related
β: Basaltic
α: Rhyolitic
σ: Volcano–sedimentary
ω: Undifferentiated
γ: Granitic
μ: Gabbroic and Ultramafic
m1: Low to medium grade
m2: Medium to high grade
Eon
Era
Period
Ma
s1
s2
θ
β
α
σ
ω
γ
μ
m1
m2
Phanerozoic
Cenozoic
Mesozoic
Paleozoic
Proterozoic
Quaternary
Neogene
Paleogene
Cretaceous
Jurassic
Triassic
Permian
Carboniferous
Devonian
Silurian
Ordovician
Cambrian
Calymmian
Statherian

Figure 2:

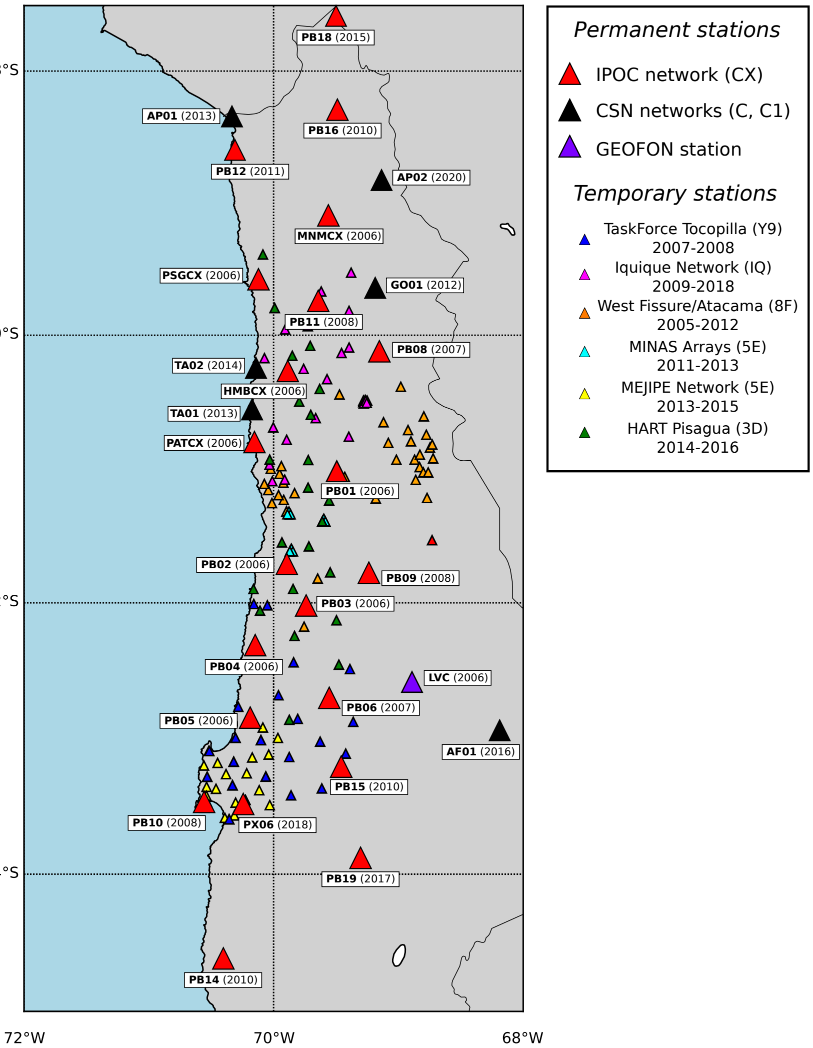

Permanent stations
IPOC network (CX)
CSN networks (C, C1)
GEOFON station
Temporary stations
TaskForce Tocopilla (Y9) 2007-2008
Iquique Network (IQ) 2009-2018
West Fissure/Atacama (8F) 2005-2012
MINAS Arrays (5E) 2011-2013
MEJIPE Network (5E) 2013-2015
HART Pisagua (3D) 2014-2016
PB18 (2015)
AP01 (2013)
PB16 (2010)
PB12 (2011)
AP02 (2020)
MNMCX (2006)
PSGCX (2006)
GO01 (2012)
PB11 (2008)
PB08 (2007)
TA02 (2014)
HMBCX (2006)
TA01 (2013)
PATCX (2006)
PB01 (2006)
PB02 (2006)
PB09 (2008)
PB03 (2006)
PB04 (2006)
LVC (2006)
PB06 (2007)
PB05 (2006)
AF01 (2016)
PB15 (2010)
PB10 (2008)
PX06 (2018)
PB19 (2017)
PB14 (2010)
18°S
20°S
22°S
24°S
72°W
70°W
68°W

Figure 3:

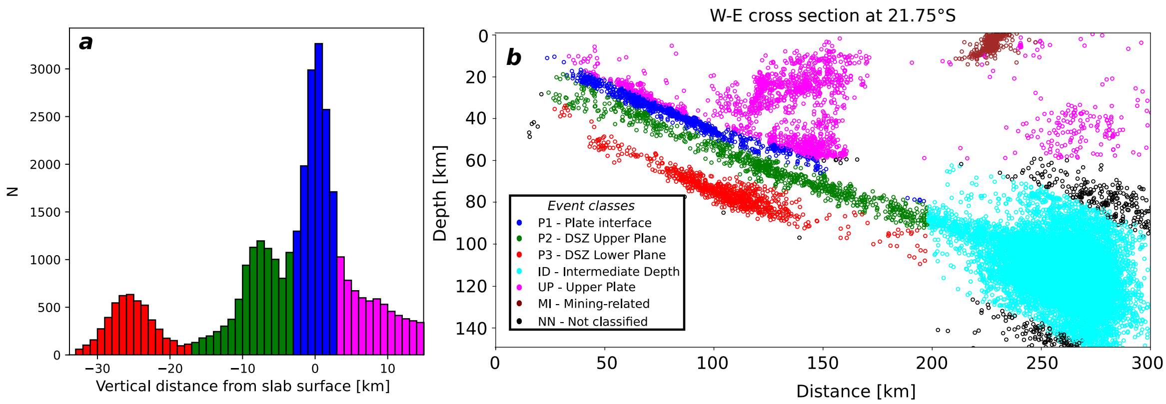

Figure 4:

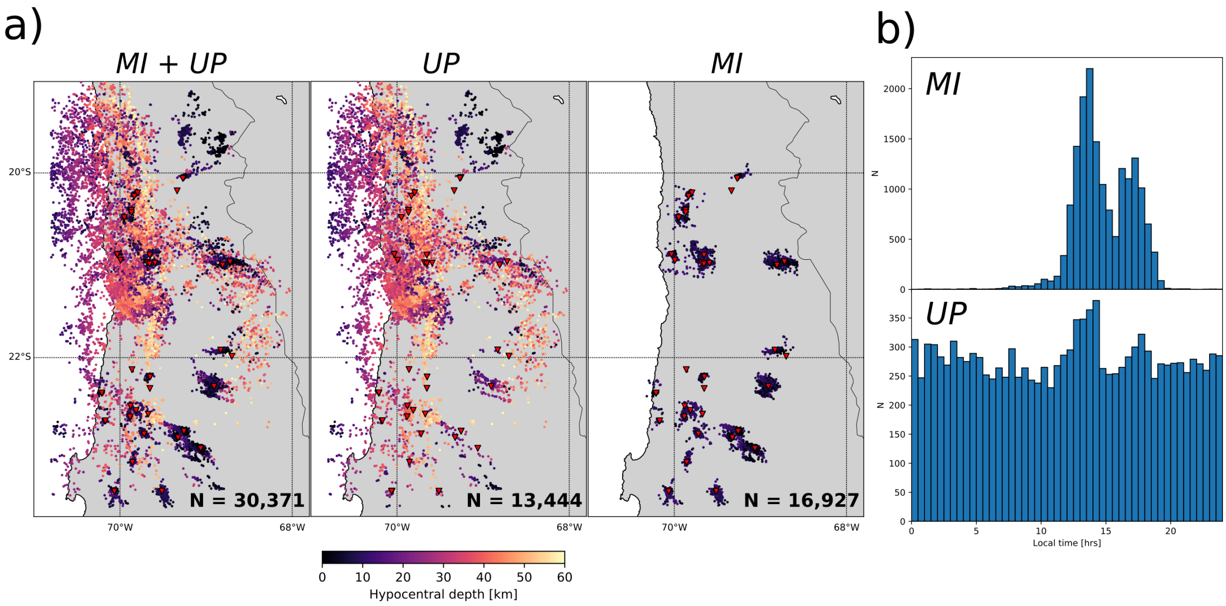

Figure 5:

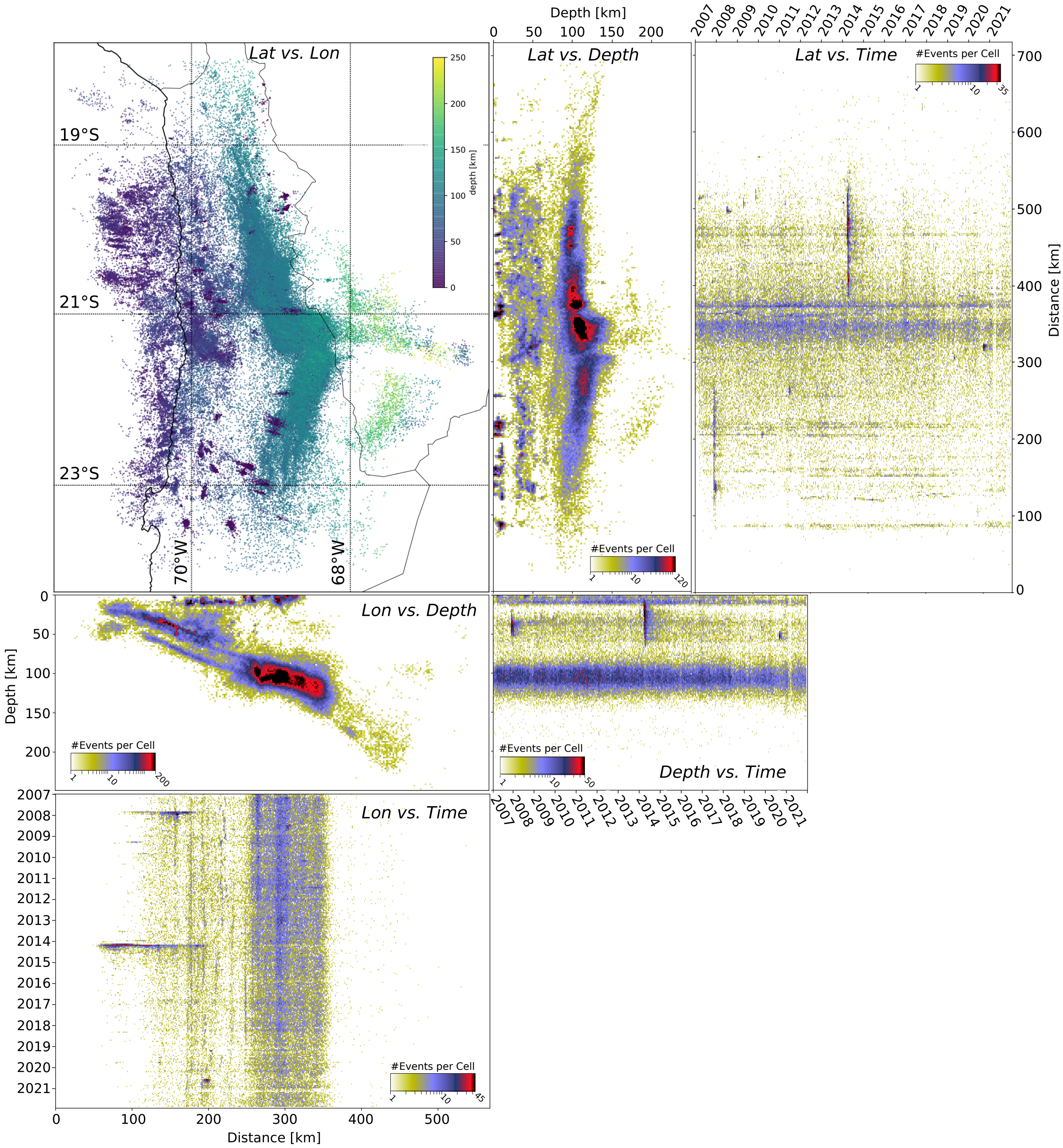

Lat vs. Lon
19°S
21°S
23°S
70°W
68°W
depth [km]
Lat vs. Depth
Depth [km]
#Events per Cell
Lat vs. Time
Distance [km]
Lon vs. Depth
Depth [km]
Depth vs. Time
Lon vs. Time
Distance [km]

Figure 6:

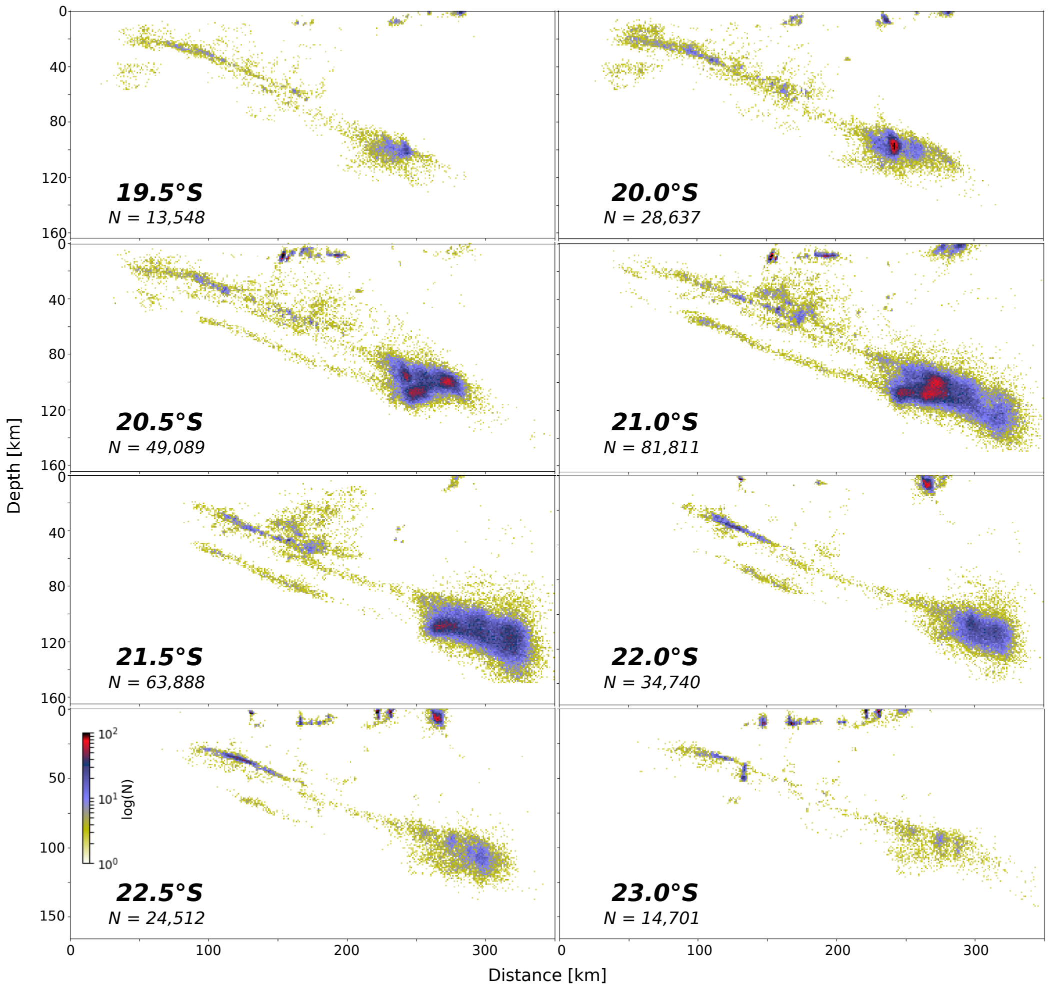
19.5°S
N = 13,548
20.0°S
N = 28,637
20.5°S
N = 49,089
21.0°S
N = 81,811
21.5°S
N = 63,888
22.0°S
N = 34,740
22.5°S
N = 24,512
23.0°S
N = 14,701
Depth [km]
Distance [km]
log(N)

Figure 7:

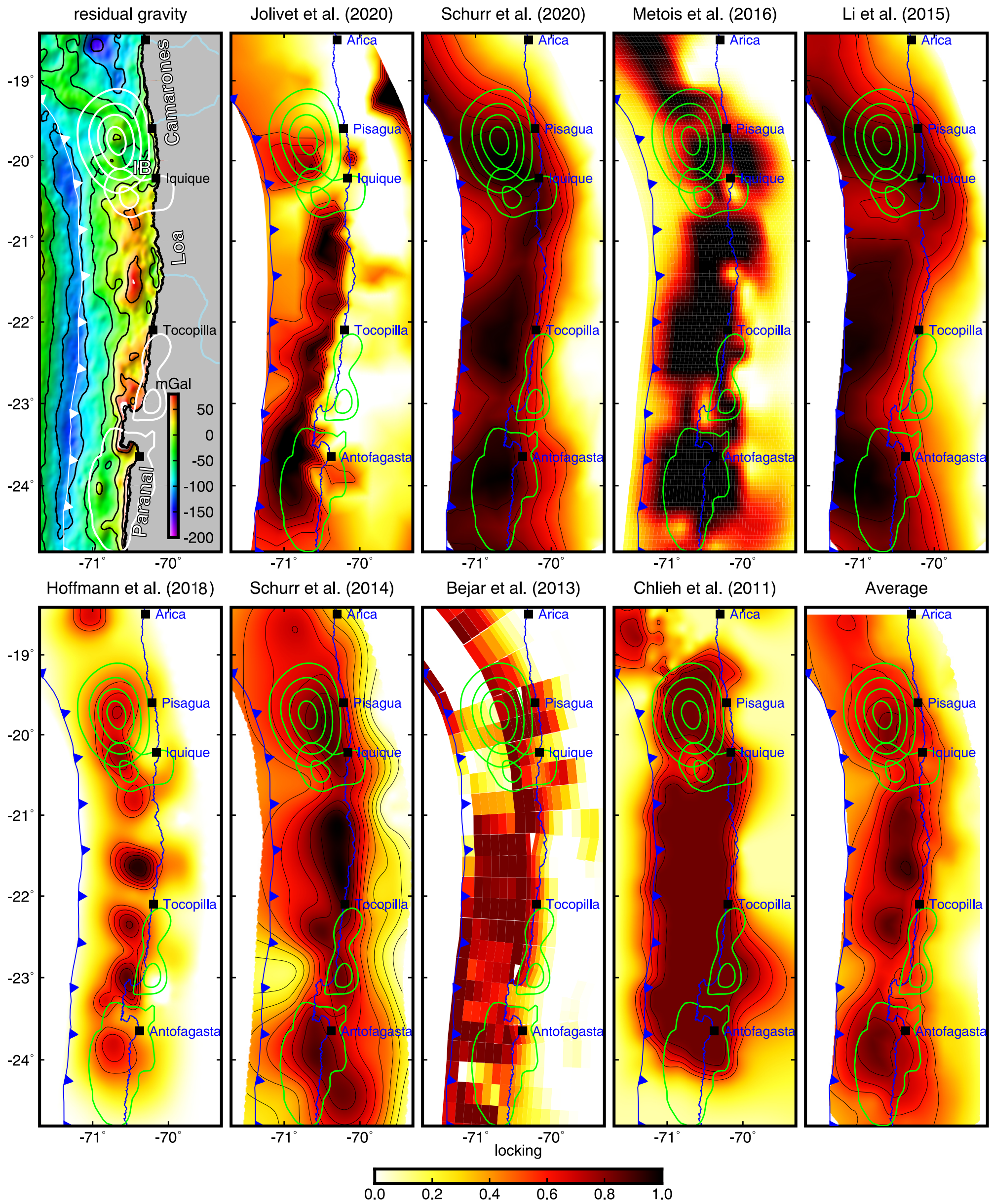
residual gravity
Jolivet et al. (2020)
Schurr et al. (2020)
Metois et al. (2016)
Li et al. (2015)
Hoffmann et al. (2018)
Schurr et al. (2014)
Bejar et al. (2013)
Chlieh et al. (2011)
Average
Arica
Pisagua
Iquique
Tocopilla
Antofagasta
Camarones
IB
Loa
Paranal
mGal
50
0
-50
-100
-150
-200
-19˚
-20˚
-21˚
-22˚
-23˚
-24˚
-71˚
-70˚
locking
0.0
0.2
0.4
0.6
0.8
1.0

Figure 8:

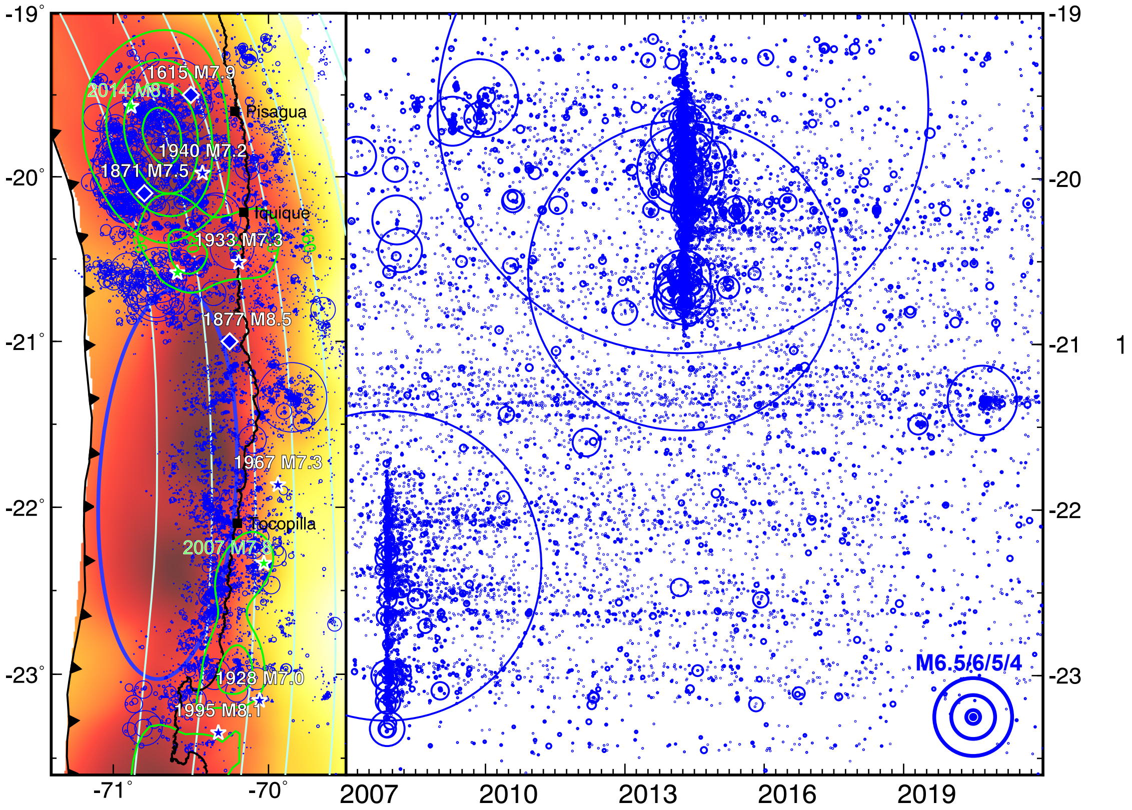

Figure 9:

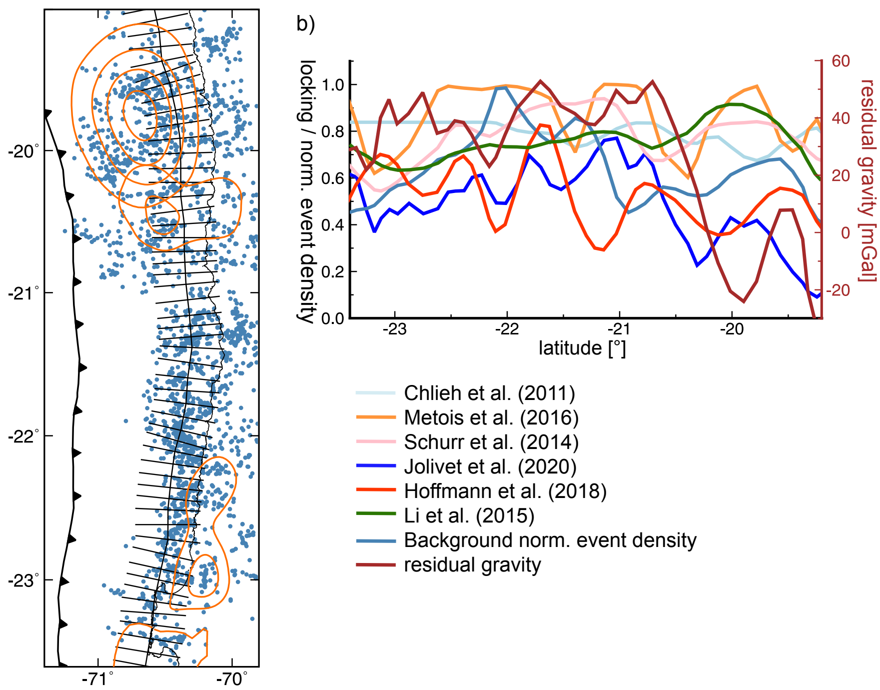

Figure 10:

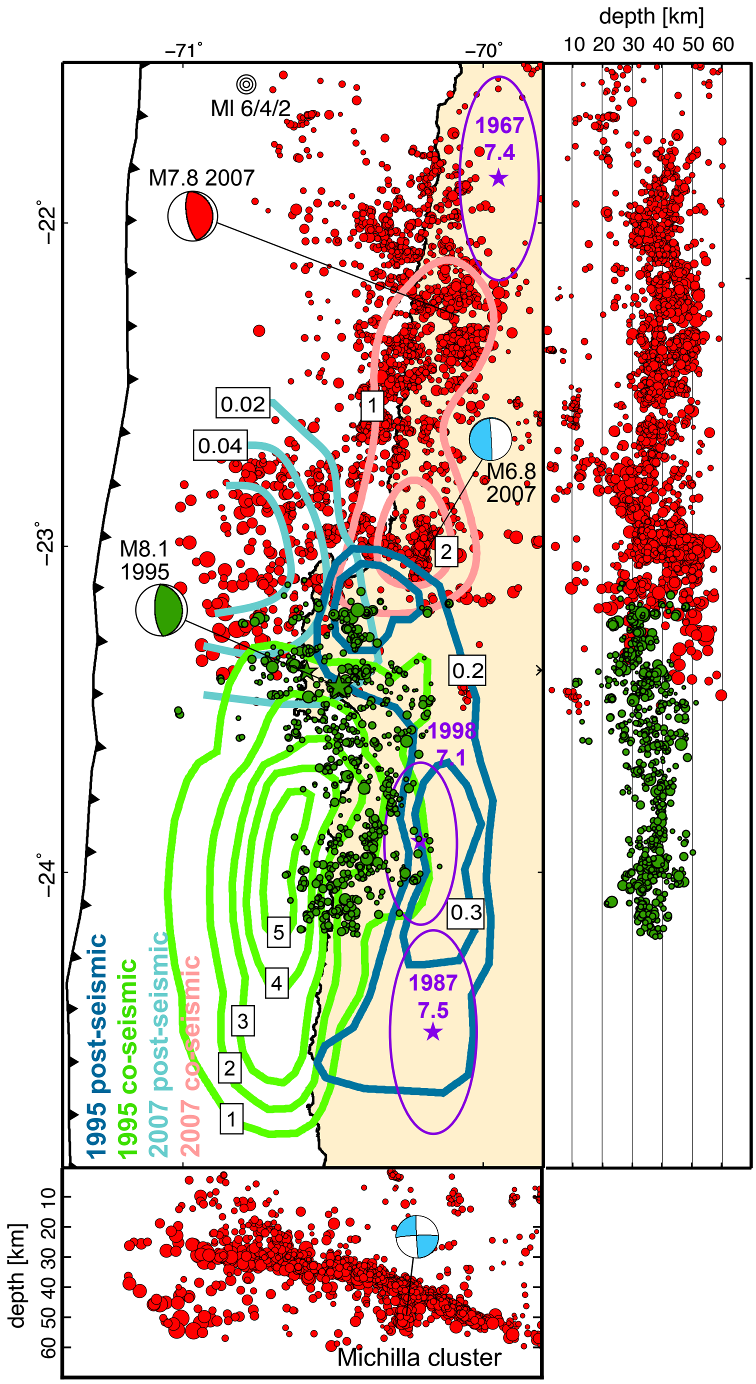

depth [km]
10 20 30 40 50 60
-71°
-70°
-22°
-23°
-24°
Ml 6/4/2
M7.8 2007
1967
7.4
0.02
0.04
1
M6.8
2007
2
M8.1
1995
0.2
1998
7.1
0.3
5
4
3
2
1
1987
7.5
1995 post-seismic
1995 co-seismic
2007 post-seismic
2007 co-seismic
depth [km]
10 20 30 40 50 60
Michilla cluster

Figure 11:

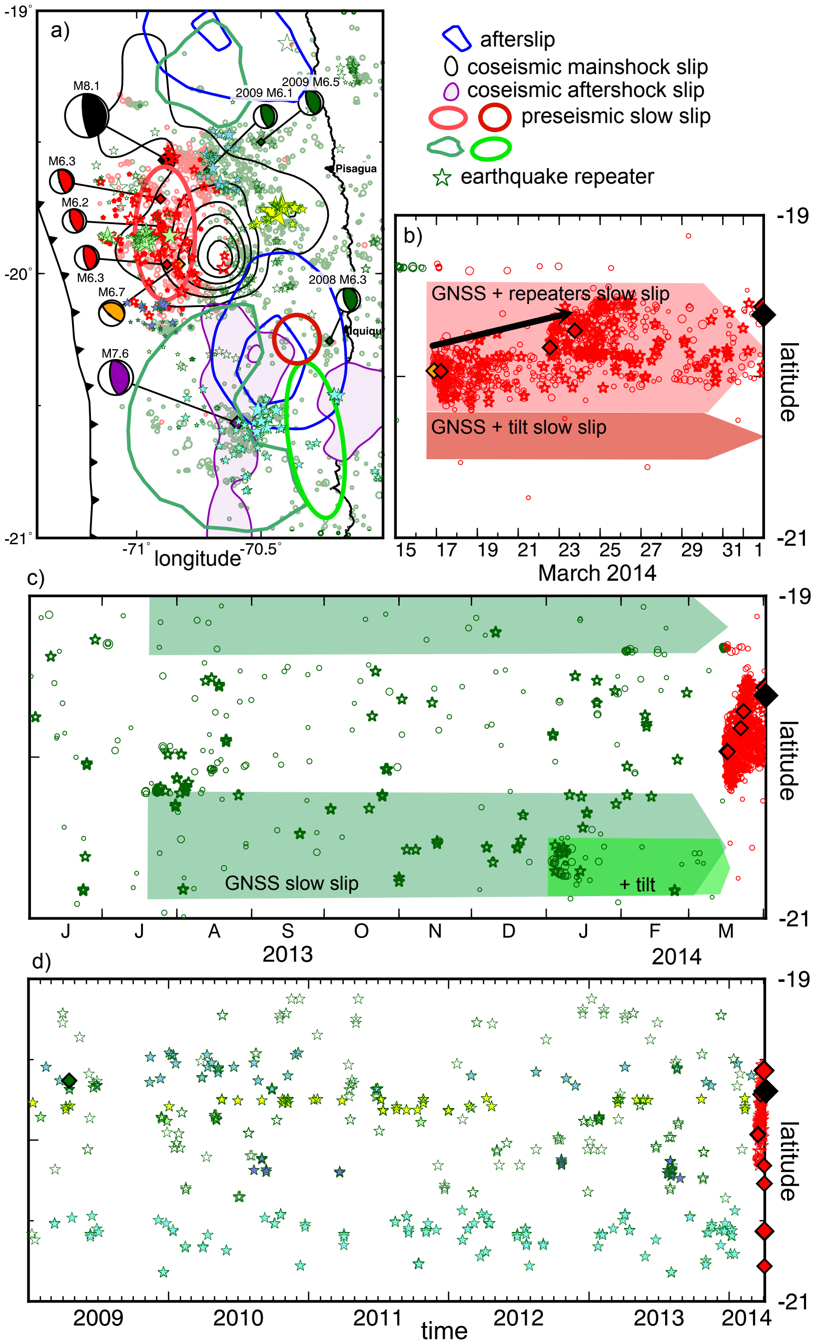

a)
afterslip
coseismic mainshock slip
coseismic aftershock slip
preseismic slow slip
earthquake repeater
M8.1
M6.3
M6.2
M6.3
M6.7
M7.6
2009 M6.1
2009 M6.5
2008 M6.3
Pisagua
-19°
-20°
-21°
-71°
-70.5°
longitude
b)
GNSS + repeaters slow slip
GNSS + tilt slow slip
15 17 19 21 23 25 27 29 31 1
March 2014
latitude
c)
GNSS slow slip
+ tilt
J J A S O N D J F M
2013
2014
d)
2009 2010 2011 2012 2013 2014
time

Figure 12:

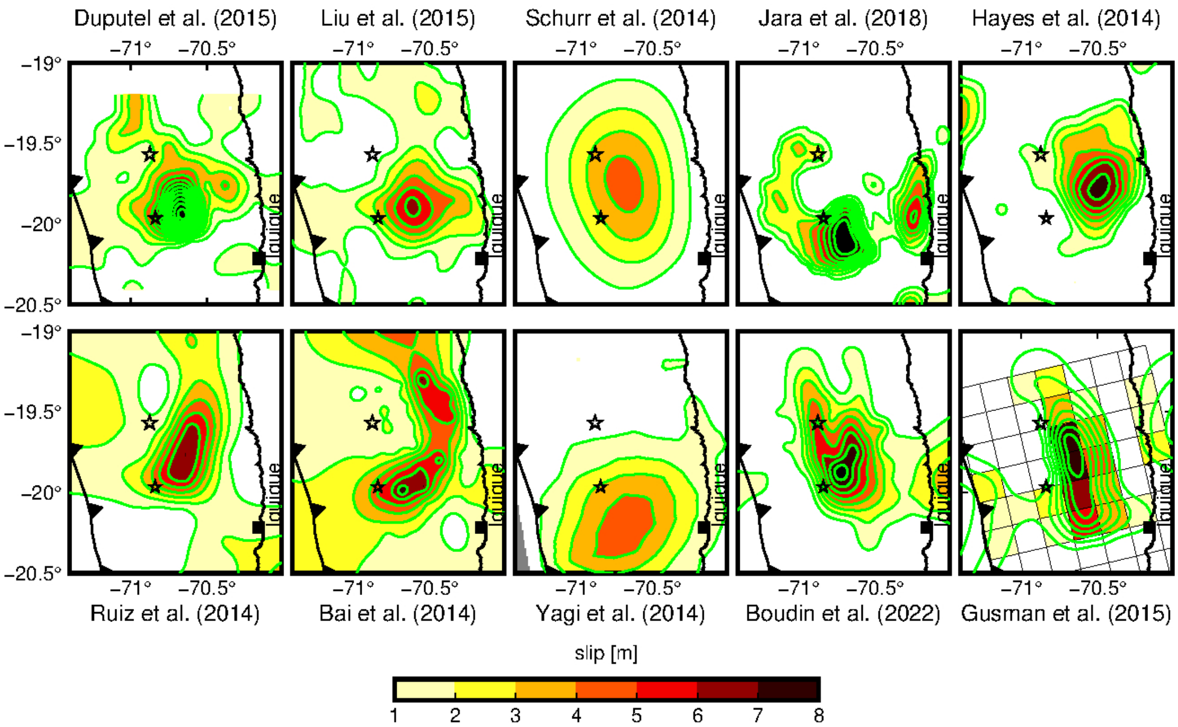
Duputel et al. (2015)
Liu et al. (2015)
Schurr et al. (2014)
Jara et al. (2018)
Hayes et al. (2014)
−71°
−70.5°
−19°
−19.5°
−20°
−20.5°
Iquique
Ruiz et al. (2014)
Bai et al. (2014)
Yagi et al. (2014)
Boudin et al. (2022)
Gusman et al. (2015)
slip [m]
1
2
3
4
5
6
7
8

Figure 13:

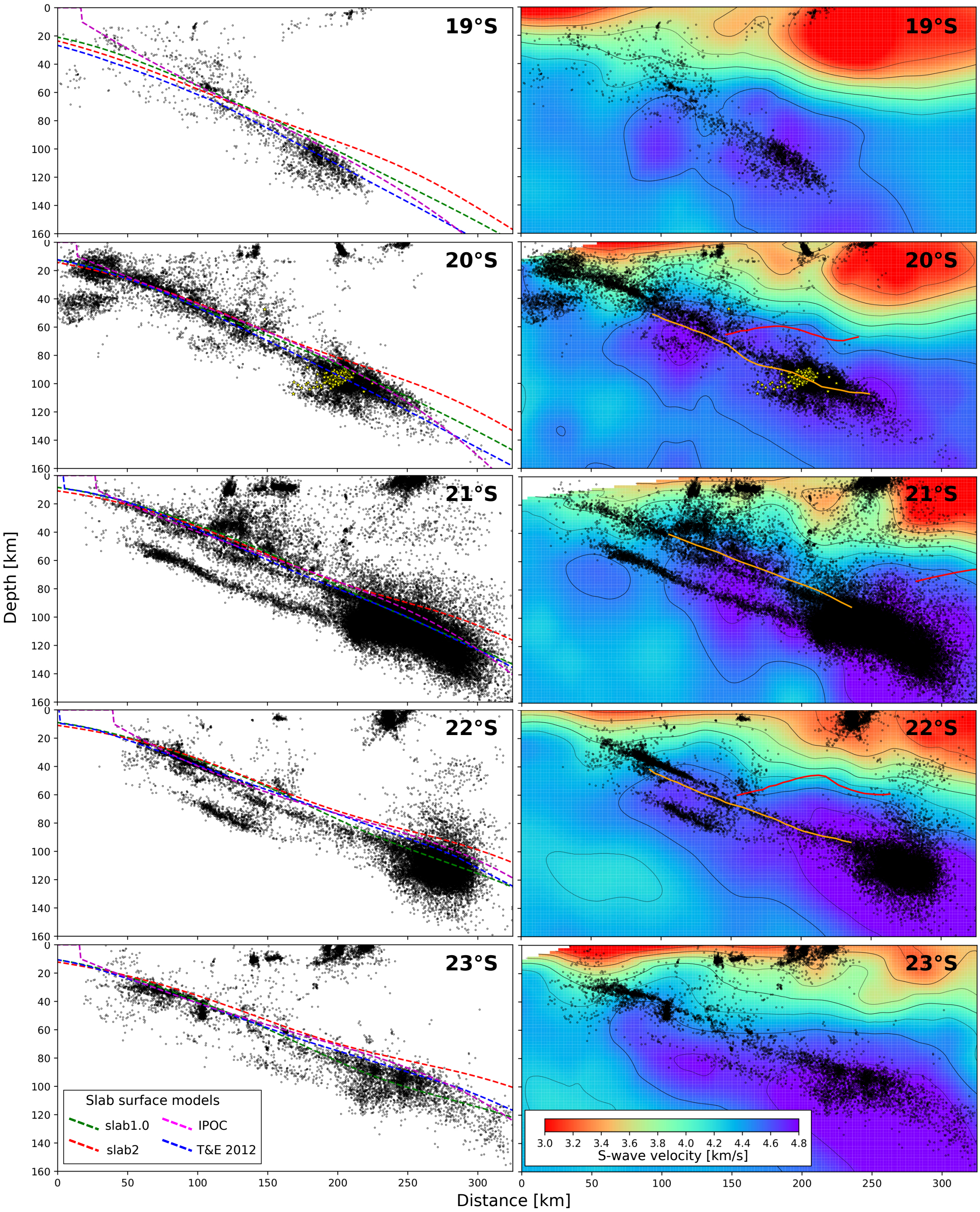

19°S
20°S
21°S
22°S
23°S
Depth [km]
Distance [km]
Slab surface models
slab1.0
IPOC
slab2
T&E 2012
S-wave velocity [km/s]

Figure 14:

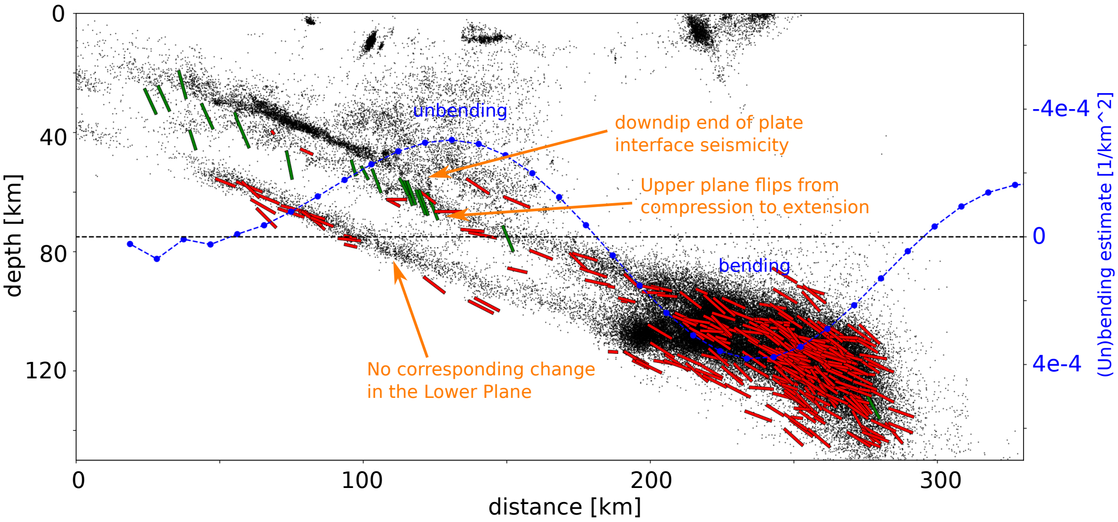

Figure 15:

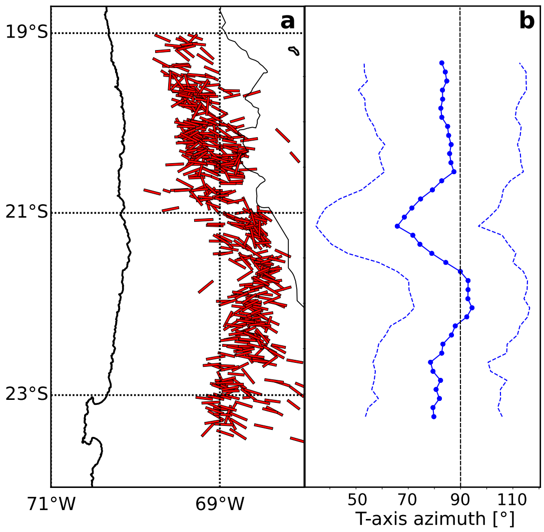

Figure 16:

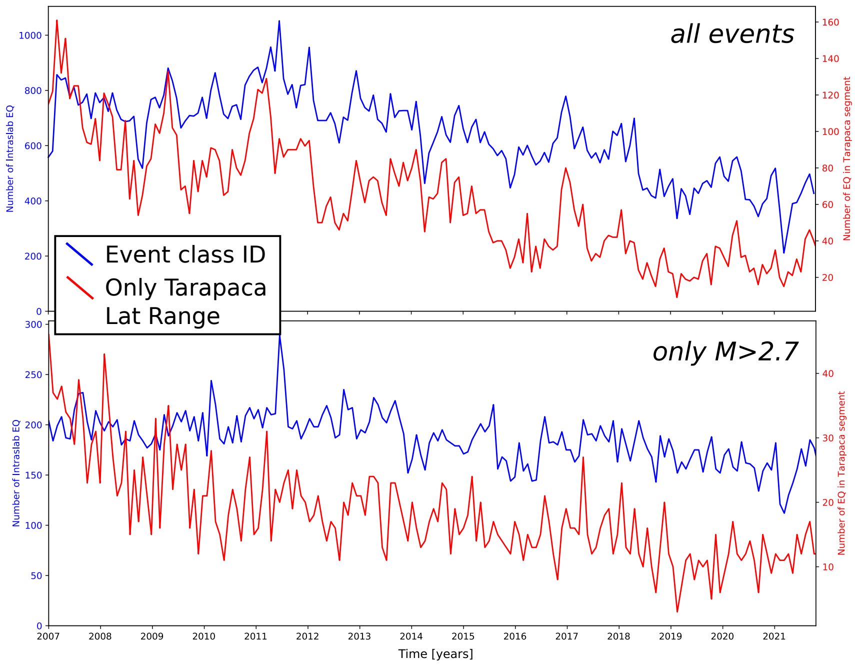

Figure 17:

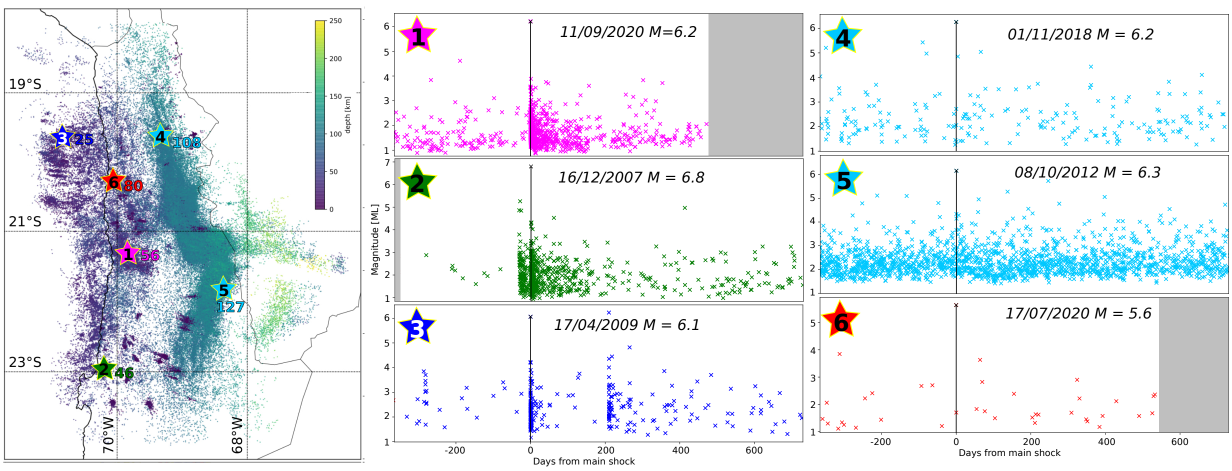

Figure 18:

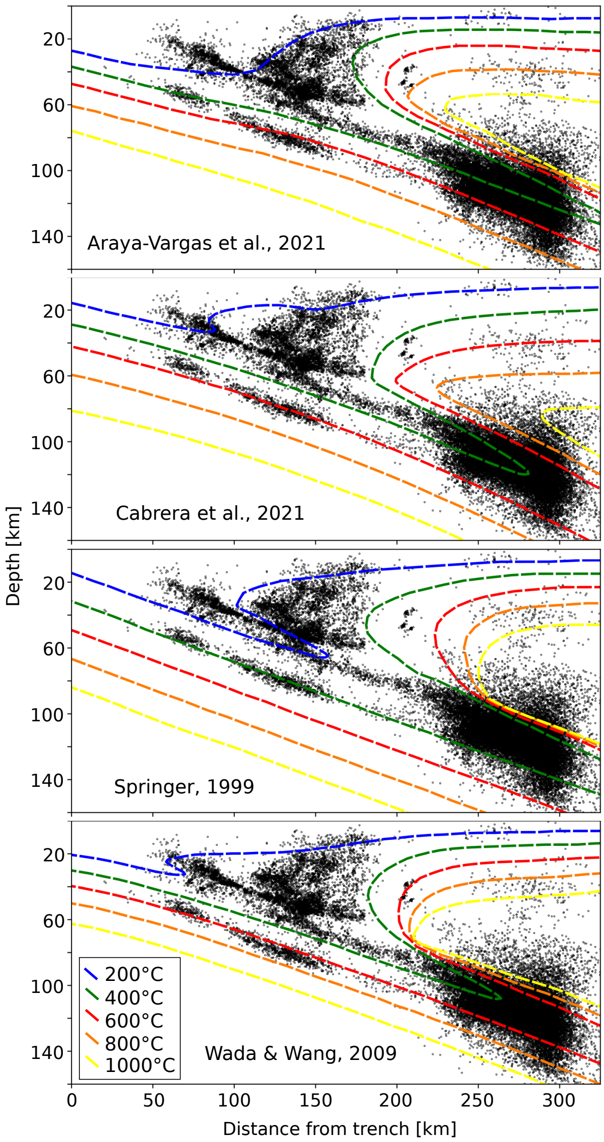

Araya-Vargas et al., 2021
Cabrera et al., 2021
Springer, 1999
Wada & Wang, 2009
200°C
400°C
600°C
800°C
1000°C
Depth [km]
Distance from trench [km]

Figure 19:

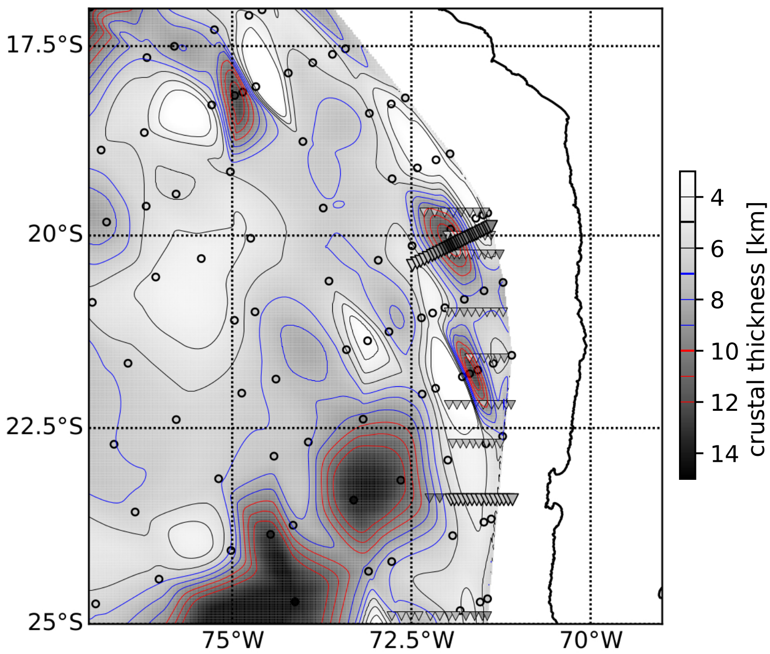
17.5°S
20°S
22.5°S
25°S
75°W
72.5°W
70°W
4
6
8
10
12
14
crustal thickness [km]

Figure 20:

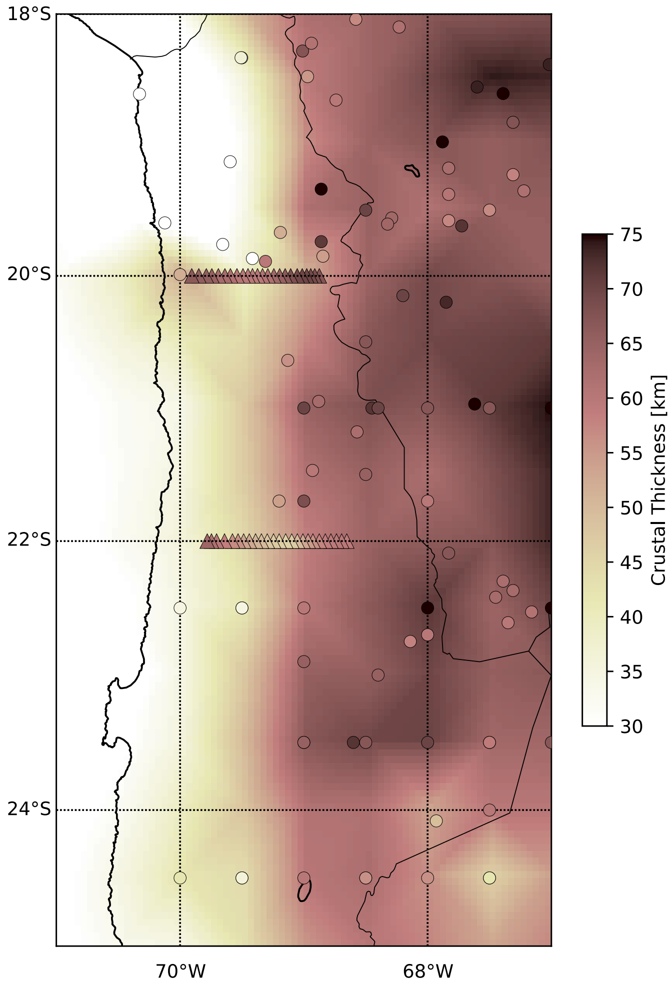

18°S
20°S
22°S
24°S
70°W
68°W
75
70
65
60
55
50
45
40
35
30
Crustal Thickness [km]

Figure 21:

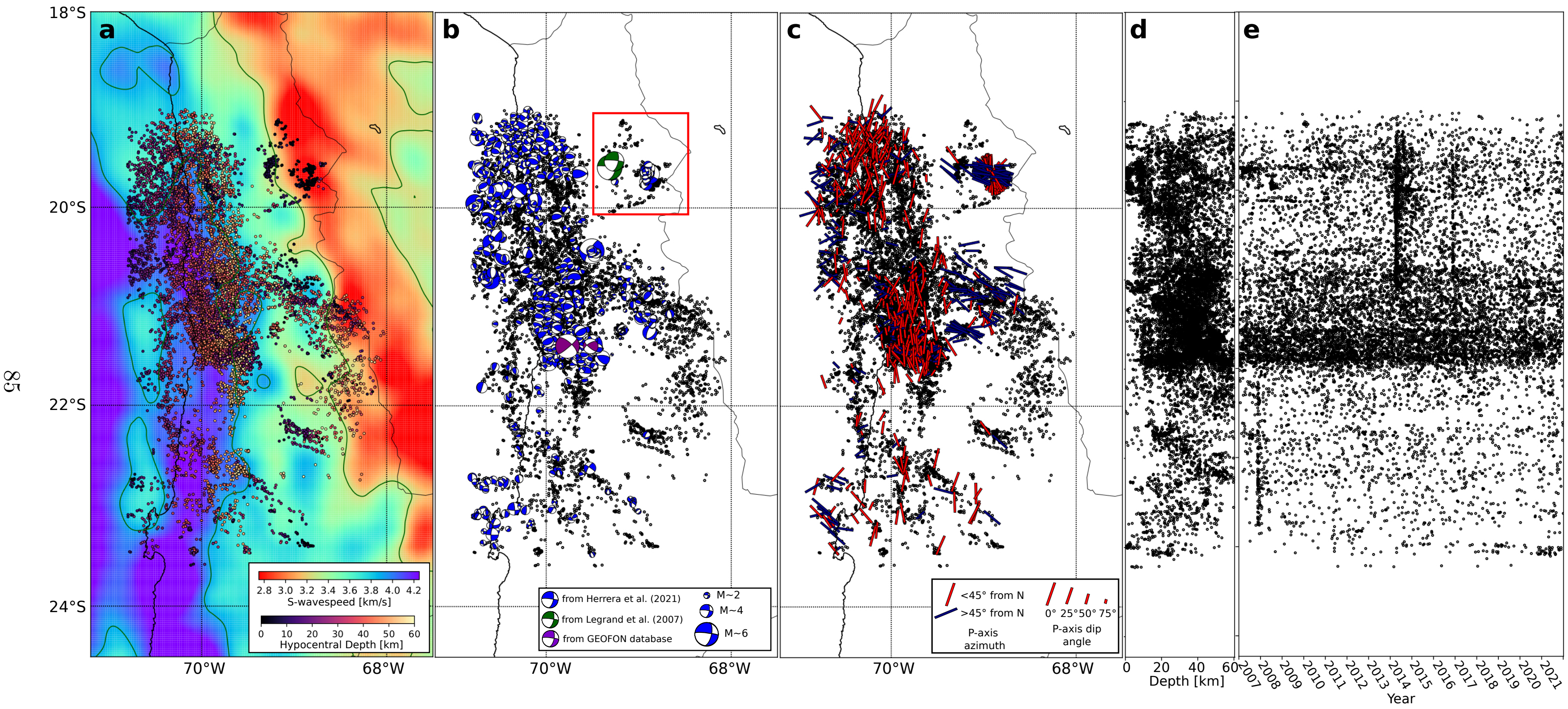

18°S
20°S
22°S
24°S
70°W
68°W
a
2.8 3.0 3.2 3.4 3.6 3.8 4.0 4.2
S-wavespeed [km/s]
0 10 20 30 40 50 60
Hypocentral Depth [km]
b
from Herrera et al. (2021)
from Legrand et al. (2007)
from GEOFON database
M~2
M~4
M~6
c
<45° from N
>45° from N
P-axis azimuth
0° 25° 50° 75°
P-axis dip angle
d
0 20 40 60
Depth [km]
e
2007 2008 2009 2010 2011 2012 2013 2014 2015 2016 2017 2018 2019 2020 2021
Year

Figure 22:

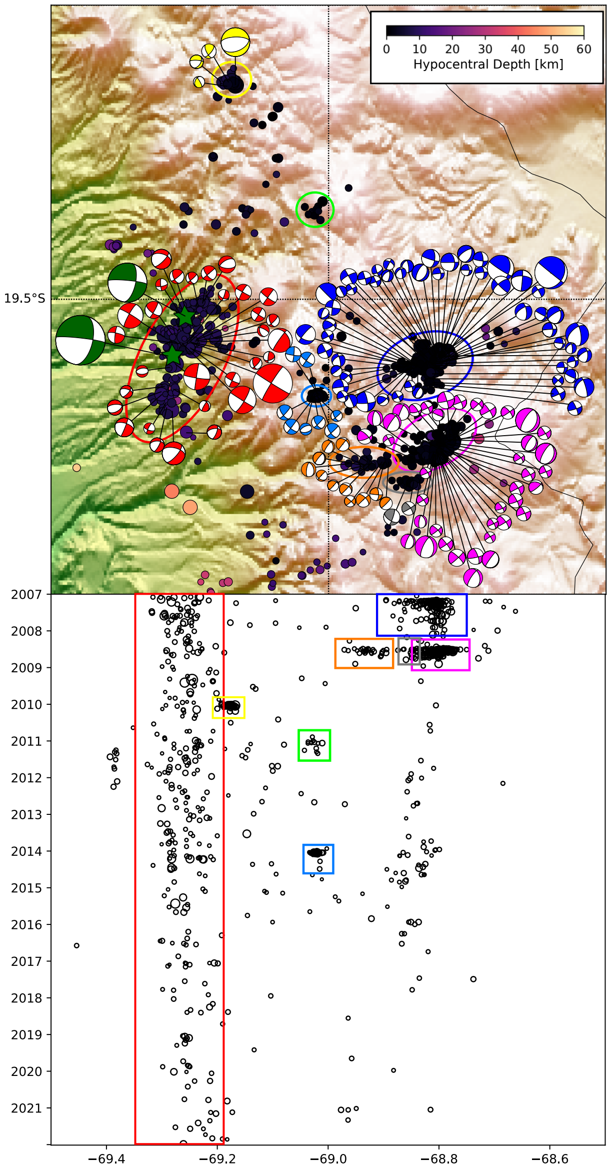
0 10 20 30 40 50 60
Hypocentral Depth [km]
19.5°S
2007
2008
2009
2010
2011
2012
2013
2014
2015
2016
2017
2018
2019
2020
2021
−69.4
−69.2
−69.0
−68.8
−68.6

Figure 23:

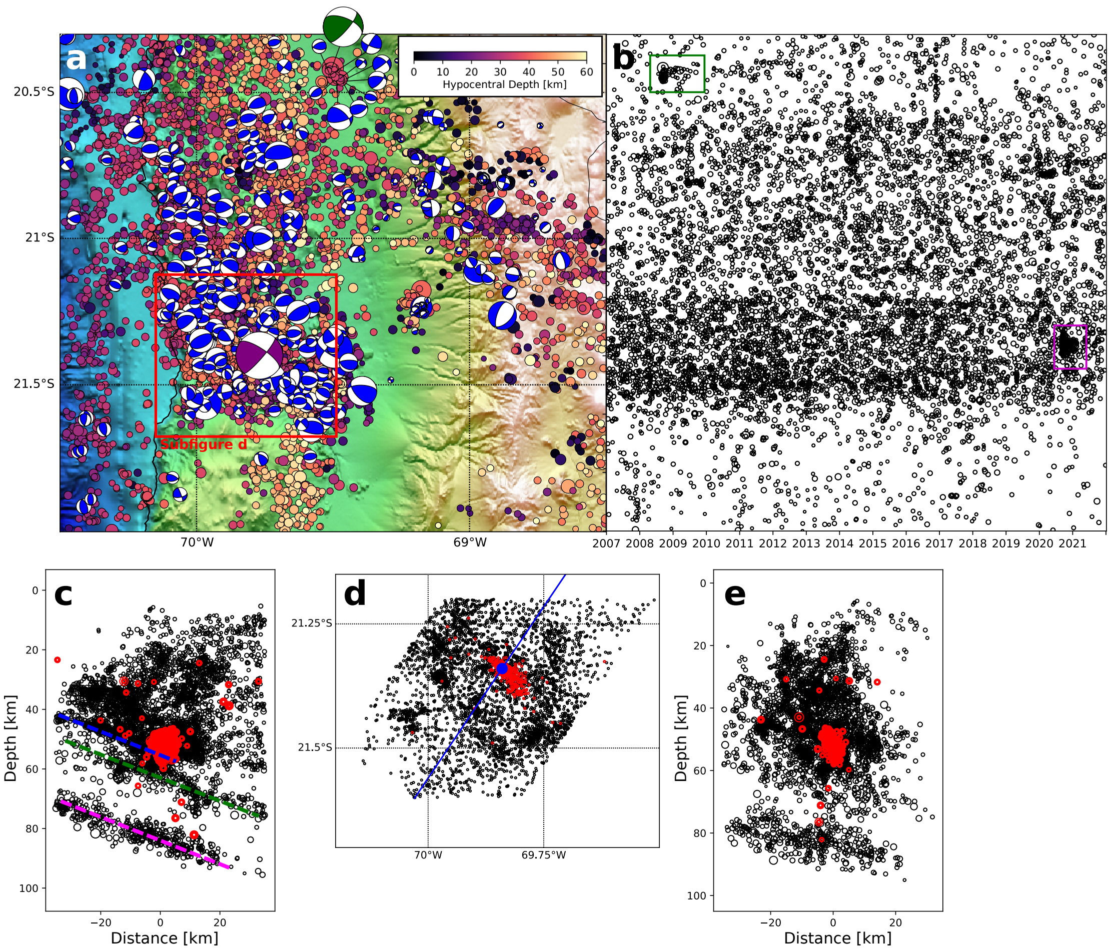

a
b
c
d
e
Hypocentral Depth [km]
Subfigure d
Depth [km]
Distance [km]

Figure 24:

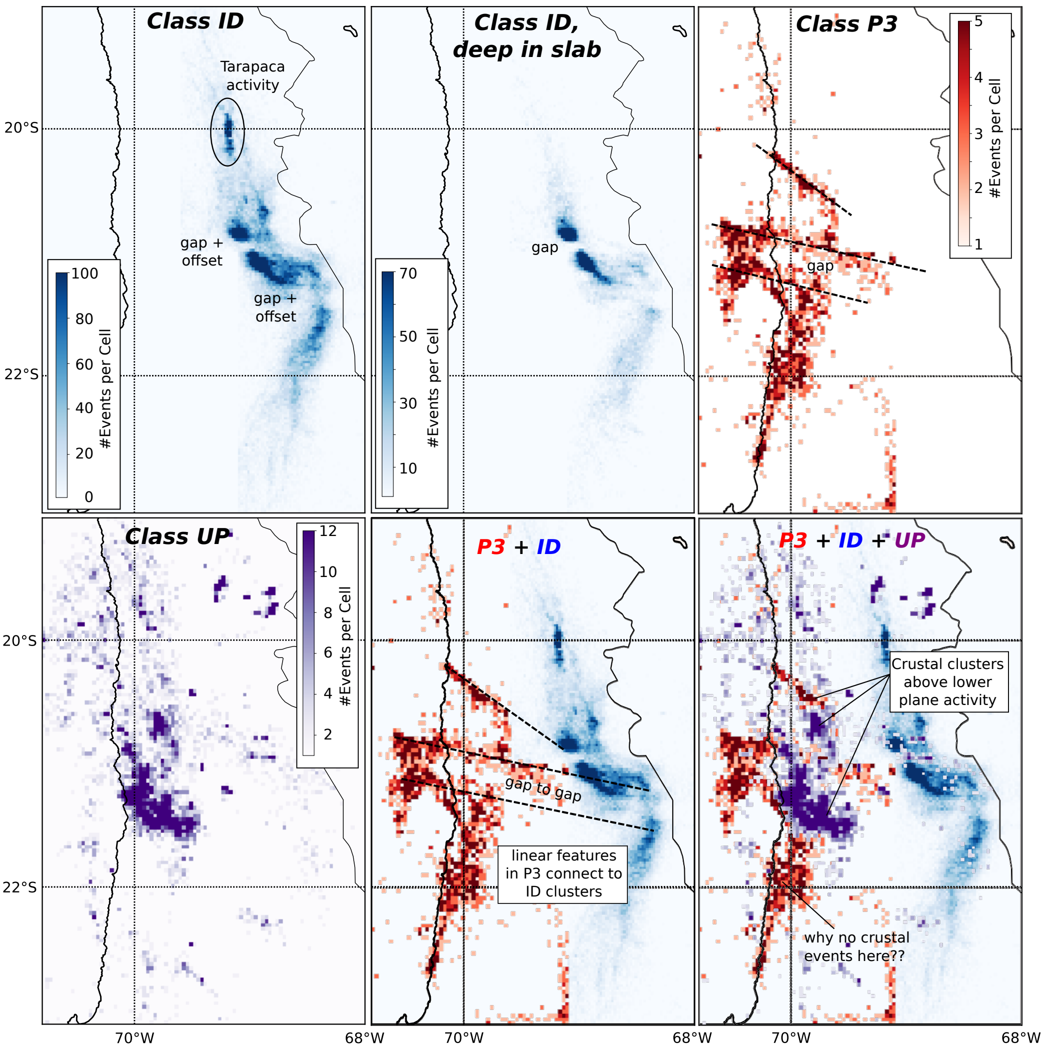

Class ID
Tarapaca
activity
gap +
offset
gap +
offset
#Events per Cell
Class ID,
deep in slab
gap
Class P3
gap
Class UP
P3 + ID
gap to gap
linear features
in P3 connect to
ID clusters
P3 + ID + UP
Crustal clusters
above lower
plane activity
why no crustal
events here??
20°S
22°S
70°W
68°W

Figure 25:

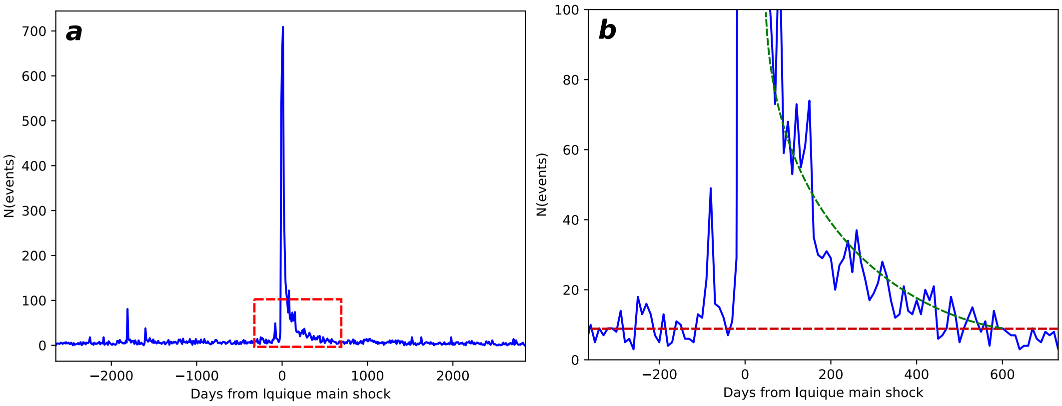
a
N(events)
700
600
500
400
300
200
100
0
−2000
−1000
0
1000
2000
Days from Iquique main shock
b
100
80
60
40
20
0
−200
0
200
400
600
Days from Iquique main shock

Figure 26:

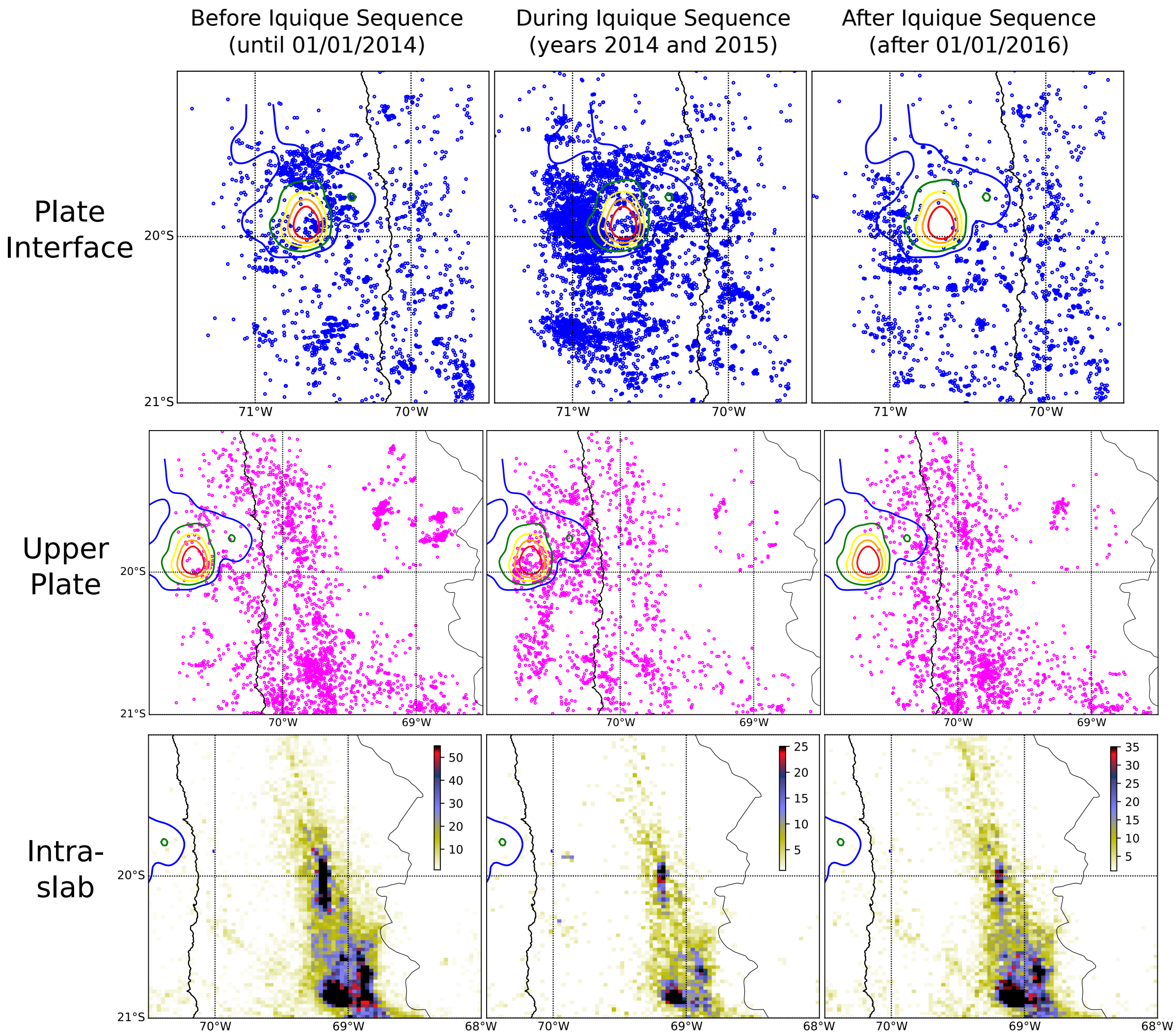
Before Iquique Sequence
(until 01/01/2014)
During Iquique Sequence
(years 2014 and 2015)
After Iquique Sequence
(after 01/01/2016)
Plate
Interface
Upper
Plate
Intra-
slab
20°S
21°S
71°W
70°W
69°W
68°W
50
40
30
20
10
25
15
5
35

Figure 27:

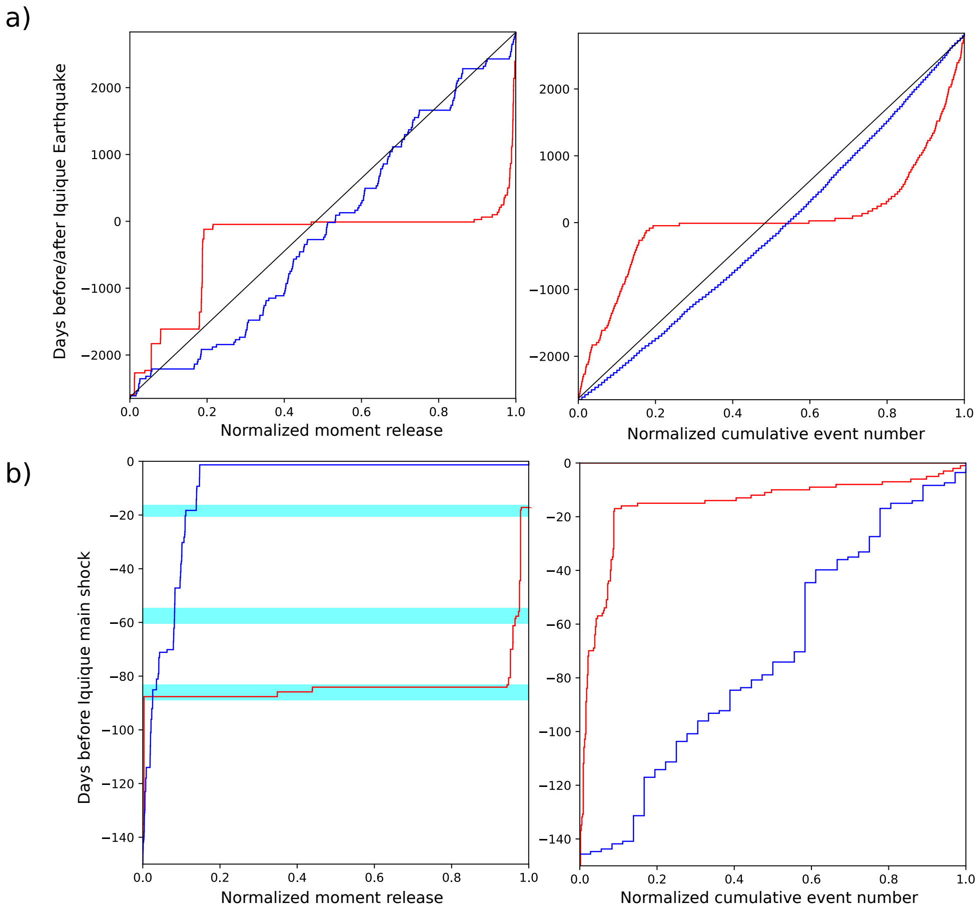
a)
b)
Days before/after Iquique Earthquake
Normalized moment release
Normalized cumulative event number
Days before Iquique main shock
Normalized moment release
Normalized cumulative event number

Figure 28: